



The role of network directionality in the brain

Amelia Padmore

N0506339

*A dissertation submitted in partial fulfilment of the requirements of
Nottingham Trent University for the degree of Master of Philosophy.*

November 2021

Copyright Statement

This work is the intellectual property of the author. You may copy up to 5% of this work for private study, or personal, non-commercial research. Any re-use of the information contained within this document should be fully referenced, quoting the author, title, university, degree level and pagination. Queries or requests for any other use, or if a more substantial copy is required, should be directed in the owner(s) of the Intellectual Property Rights.

Abstract

Network science is a vast interdisciplinary area which connects disparate subjects such as mathematics, the natural sciences, sociology, information technology and more. Network neuroscience, in particular, is a thriving and rapidly expanding field in which graph theory techniques have been deployed to better understand structure-function relations in the brain across multiple temporal and spatial scales. In this thesis, we use large-scale brain network models for a range of different species (cat, Macaque monkey and *C.elegans*) to simulate important aspects of brain function, such as associative memory and synchrony related activities. Network directionality is a fundamental feature of such models, yet it is typically ignored due to limitations of non-invasive imaging techniques. Here, we explore the role that directionality plays in determining neural activity in the brain. We start by considering a system of Hopfield neural elements with heterogeneous structural connectivity given by range of species and parcellations for which network directionality information is present. We investigate the effect of removing directionality of connections on brain capacity, which we quantify via its ability to store attractor states. In addition to determining large numbers of fixed-point attractor sets, we deploy the recently developed basin stability technique in order to assess the global stability of such brain states as well as their robustness to non-small perturbations. By comparison with standard network models with the same coarse statistics, we find that directionality effects not only the number of fixed-point attractors but also the likelihood that neural systems remain in their most ‘desirable’ states. These findings suggest that directionality plays an important role in shaping transition routes between different brain networks states. We then go onto consider the impact that network directionality has on the synchrony properties of the brain. We simu-

late neural dynamics on the aforementioned connectome-based networks deploying a phase delayed Kuramoto Model, which is perhaps the simplest example of a delay-coupled oscillatory network and is well-suited to assessing how directed connectomes govern synchronisation properties of the brain. In particular, we find that network directionality profoundly impacts both the time-scale at which coordinated rhythmic activity occurs across large-scale brain networks as well as the stability properties of these synchronised states. We also find that recently observed relations between network structure and directed functional connectivity, as quantified using the directed phase lag index, appear far less conclusive when network directionality is accounted for. This study thereby emphasizes the substantial role network directionality plays in shaping the brain's ability to both store and process information.

Acknowledgements

First and foremost I would like to thank my supervisor, Dr. Jonathan Crofts for his continuous support, patience, and guidance but mostly for not giving up on me when it would have been easy to do so. I can honestly say without his help I would not be where I am today and I am so grateful to you for giving me this opportunity. Secondly to my second supervisor, Dr. Martin Nelson for his vital input into this thesis and the crucial feedback and guidance he has given me through this time. Furthermore, thank you to my third supervisor Professor Nadia Chuzhanova for the important contributions she has made to my studies over the years.

I would like to thank the NTU mathematics department as a whole and all those with whom I have shared an office throughout my time at NTU, thanks for the laughs on difficult days and for keeping me sane(ish).

I would also like to thank the Vice Chancellor's bursary for providing me with the funding to undertake this postgraduate study at NTU.

Next, a big thank you to my family especially my parents, thank you for being there for me (both emotionally and financially), I hope I have made you proud and continue to do so.

Finally, thank you to my partner, Ben, thank you for putting up with me and for always bringing a smile to my face, I would be lost without you.

Declarations

I declare that the thesis has been composed by myself and that the work has not be submitted for any other degree or professional qualification. I confirm that the work submitted is my own, except where work which has formed part of jointly-authored publications has been included.

Parts of this thesis have been prepared for publication:

1. Padmore, A., Nelson, M.R., Chuzhanova, N. and Crofts, J.J., 2020. Modelling the impact of structural directionality on connectome-based models of neural activity. *Journal of Complex Networks*, 8(4)

Contents

1	Introduction	1
1.1	A brief history of networks	1
1.2	Network neuroscience	6
1.2.1	Constructing complex brain networks	6
1.2.2	Directionality in neural networks	10
1.2.3	Network models of large-scale neural activity	11
1.2.4	Brain networks and disease	13
1.3	Thesis overview	15
2	Network preliminaries	17
2.1	Networks	17
2.1.1	Weighted networks	17
2.1.2	Directed networks	18
2.1.3	Adjacency matrices	19
2.2	Network measures	20
2.2.1	Measuring network centrality	23
2.3	Network models	25
2.3.1	Erdős-Rényi random graphs	25
2.3.2	Watts-Strogatz small-world model	27

2.3.3	Barabási-Albert model	28
2.4	Network modularity	29
2.5	Summary	32
3	The impact of structural directionality on the computational properties of a neural network	33
3.1	Brain network models	34
3.1.1	The Hopfield model	34
3.1.2	Structural connectivity	39
3.2	Basin stability	42
3.3	Results	42
3.3.1	Network analysis	42
3.3.2	Numerical simulations	44
3.3.3	Discussion	51
3.4	Summary	53
4	The impact of structural directionality on effective connectivity networks	55
4.1	The Kuramoto model	56
4.1.1	Extensions of the model to a neuroscience setting	59
4.2	Directed functional connectivity	61
4.2.1	Phase lag index	62
4.3	Numerical Experiments	64
4.3.1	Speed of Synchronisation	66
4.3.2	Stability of phase locked solutions	69
4.3.3	Phase lead/lag relations	71
4.4	Summary	75

5 Conclusions	76
5.1 Summary of thesis	76
5.2 Discussion of further work	78
A Cortical network modularity	80
B Neural network activity patterns	86
C Clustering of activity patterns for <i>C. elegans</i> neural network	93
D Other network measures correlation with dPLI	97
References	99

Introduction

Networks can be found everywhere, in both natural and manufactured structures from physical structures such as train lines, to more hypothetical connections such as friendships within social networks. Due to the prevalence of real life networks, network science is a major interdisciplinary field which combines ideas from subjects such as biology, social science, statistics, economics, mathematics, computer science and neuroscience. The study of these networks has expanded across these topics and some examples of widely studied networks are power grids [1, 2], brain networks [3], metabolic networks [4, 5] and protein-protein interactions [6], the world wide web [7], neural networks and social media [8]. In this introductory chapter we start by giving a brief historical overview of the network studies in general, before focusing in greater detail on key concepts from network neuroscience. We in particular look at the role (or rather lack of!) that directionality has played in this area to date as due to limitations in noninvasive imaging methods, information on directionality is missing in studies of the human connectome. This means that directionality is an often neglected aspect of network neuroscience research and it is not known how this vital information may impact neural networks.

1.1 A brief history of networks

The history of networks originates from the study of graph theory which began in 1736 with the Königsberg bridge problem. The city of Königsberg lay on the banks of the

river Pregel with an island in the middle and citizens would try and come up with ways to cross all seven bridges in and out of the island without traversing the same one twice. Leonhard Euler confirmed most peoples' beliefs, *i.e.* that no such solution existed, by framing the problem as a graph and using graph theoretical techniques to solve the problem [9]. Graph theory evolved and studies began on small structured graphs such as lattices, *i.e.* regular, grid-like graphs. Useful ideas that became part of fundamental discrete mathematics emerged, for example, map colouring [10] and matching theorems [11, 12]. (For a more in depth introduction of graph theory see, for example, [13, 14].)

In 1959 Erdős and Rényi produced a seminal paper which explored larger graphs named random graphs [15]. Within the paper they introduced $G(n, p)$ as a collection of networks that have n nodes with all pairs of nodes connected with probability p . This became known as the Erdős Rényi (ER) random graph that is widely used in research to this very day as a null graph with which to test hypotheses within network science.

Graph theory continued to grow and in 1967 social psychologist Stanley Milgram confirmed a network phenomenon known as the small-world effect [16]. To determine how interconnected society was he set about trying to understand how many people know one another and how wide spread the impact of someone's connections is. To discover how connected people are within the USA, Milgram conducted an experiment:

- He sent letters to people from Omaha, Nebraska instructing them to forward the letter to randomly selected people in Boston, Massachusetts.
- When a person received a letter they were instructed to do one of two things:
 1. If they knew the intended person, they were to forward it straight to them.
 2. If they didn't know the intended person they were to forward it to someone more likely to know the intended.

From this, Milgram found that the average path length between the person that started with the letter and the intended person was 5.5; this was a lot smaller than first predicted given the size of the United States. This discovery has also led to the idea of

‘six degrees of separation’ and the theory that everyone in the world is connected via approximately six people. This also leads to the saying of ‘it’s a small world’.

Empirically, a network is termed small-world if it has a ‘small’ average (or characteristic) path-length together with a ‘high’ level of clustering. The clustering coefficient is a measure to indicate how clustered a network is. First thought of in 1949, it uses triplets, three nodes connected by either two or three edges, as they can mean that connections are close to one another [17]. This measure is calculated by computing the number of triangles divided by the sum of triplets, *i.e.* it equals the proportion of triangles present within a network.

Another important development made largely by social scientists was the idea of network centrality. A centrality measure provides a way of ordering the nodes within a network in terms of ‘importance’, the definition of this importance depends on the problem at hand and so a plethora of centrality measures have been put forward (see [18] and references therein for a discussion on centrality measures in a bioinformatics setting). Popular examples of centrality measures include: degree centrality (highest degree is the most important node); eigenvector centrality; Katz centrality (takes into account the influence of linked nodes)[19] and betweenness centrality (when a node is central to linking two areas of a network together) [20]. Measures such as characteristic path length and clustering are key in quantifying non-trivial structures present within large complex networks. We discuss these measures (and others) in more detail in Chapter 2 with a particular focus on those measures of historical importance to neuroscience and thus of relevance to the work in this thesis.

The modern discipline of Network Science exploded into life in the late nineties with two seminal papers. In 1998 Watts and Strogatz released a paper [21], which was perhaps the birth of network science as a field in its own right. They studied real-world networks and compared the average path length and clustering levels. Until this point scientists had largely studied two extremes: structured lattices (or regular networks), which exhibit high levels of clustering but have a large average path-length; and random networks, which have a small average path-length and low levels of clustering. Therefore neither of the networks exhibited the small-world property that appeared

prevalent in real-world networks. The Watts-Strogatz model constructs a random network that admits both of these two important properties. Beginning with a regular lattice network, Watts and Strogatz rewired each edge, or added a new edge (depending on the algorithm used), with a predetermined probability (p) so that a node is randomly connected to another randomly chosen node. This method adds shortcuts and, with each shortcut, the average path length decreases but (for small values of p) this has little effect on the high levels of clustering. Thus, this procedure generates networks with the desired small-world property, which can be used as toy models to compare properties of small-world networks and real life networks.

Another massively influential paper in Network Science was released in 1999 by Barabási and Albert, which examined another way to create networks with a desired effect; in this case a scale-free degree distribution, which is a property that many real-world networks possess [22]. A scale-free network has a degree distribution that follows a power law, which means that in these networks it is common to have a large number of nodes with small degree and a small number of nodes with a large degree. Barabási and Albert posited that this was a natural consequence of so-called *preferential attachment*, meaning that nodes have a preference to attach themselves to nodes with higher degree. The algorithm for constructing a network with scale-free degree distribution starts with some small initial network, before proceeding iteratively by adding a new node at each step, which is connected to already existing nodes with a probability that is proportional to their current degree. This way the higher the degree the more likely the new node is to create a new edge with that node. This model is often termed the preferential attachment model.

Another important concept, particularly in network neuroscience and biology more widely, is that of *community structure* of networks [23]. The most popular method for determining community structure, or *modularity*, was introduced in 2002 by Girvan and Newman. The method provides a single measure, or modularity score, which quantifies the extent to which a network's nodes can be partitioned into subsets such that nodes within the same sets are highly connected and those nodes in different sets are sparsely connected. This is just one example of a modularity algorithm; there are many

other ways to calculate the community structure of networks [24, 25]. Like most biological networks, it is well known that cortical networks display high levels of modularity and this is believed to be related to functional segregation and integration in the brain [26]. Once again, we examine how to compute modularity measures in more detail in Chapter 2.

Before moving on to focus on neuroscience applications in network science, it is worth noting the recent development in the field whereby more complex objects known as multilayer networks are used to represent systems in which multiple interaction types are present. Neuroscience, in particular, is awash with multimodal datasets that could benefit from such a holistic approach. More, commonly (especially in neuroscience) such systems can be modelled using a fixed set of network nodes (general multilayer networks allow for variation in nodes as well as both inter and intra connectivity [27]) across different layers – each describing a different type of interaction – and is termed a *multiplex network*. An example of a multiplex network is a two layer structure-function network in which one layer represents anatomical connectivity and the second functional connectivity – here the nodes generally denote brain regions as given by some parcellation of the brain. Examples of more general multilayer networks include a recent network model of the *C. Elegans* nervous system, which consisted of layers describing synaptic, gap junction and neuromodulator interactions [28], as well as a multilayer functional network consisting of different layers (including both inter and intra layer connections) for the different frequency bands in MEG data [29]. Such an approach adds layers of complexity and with it comes new solutions *and* problems. New complex network measures have been forwarded [30], including, for example, new multilayered centrality measures [31], as well as the extension of network studies of diffusion processes to the multilayer setting [32], and these methods have recently been applied to human disease [33, 34, 35].

1.2 Network neuroscience

The brain is one of the most complex systems in the world; it is a system of interrelated parts which exhibit properties and behaviors that cannot be explained by analysing these parts in isolation [36, 37]. Due to this complexity, the brain is often modelled as a network, where the nodes denote brain regions and edges denotes relationships between the aforementioned brain regions – at least at the scales that we consider. In what follows, we provide a brief overview into the methodologies behind the construction of network models of the brain, starting with a discussion of the different scales at which one can study, before considering the different types of brain network models (*i.e.*, structural, functional, *etc.*). We then touch upon the important topic of network directionality, a concept that is typically overlooked in modern network neuroscience investigations, and one that will play a key role in the work presented within this thesis. Finally, we examine the relevant and recent research into the connection of brain network architecture and neural disease, and discuss how the ideas of network neuroscience may one day provide solutions to some of the biggest diseases, such as Alzheimer’s, epilepsy and schizophrenia.

1.2.1 Constructing complex brain networks

There have been many questions on how to best represent the brain as a network. A lot of network neuroscience research have been done at different scales and there has been some attempts to bridge the gap between these different levels of research [38]. The most common scales used are the micro-scale, where problems are researched at the cellular level; meso-scale, where populations of neurons are grouped together and macro-scale, where the brain can be parcellated or investigated as a whole.

A brief view into the cellular level shows that the brain is made up of around 100 billion cells called neurons and most connections between them are made up of synapses. Neurons communicate by passing electrochemical signals to one another by ‘spiking’ and ‘firing’ these impulses along axons and across synapses, see Figure 1.1. To understand whole brain dynamics at the micro-scale would require us to construct a network

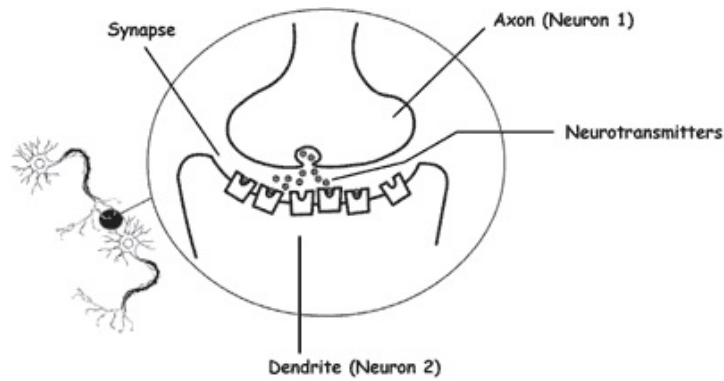


Figure 1.1: An illustration of a synapse [39]

model of local organisation consisting of billions of nodes all connected via trillions of synaptic links, which is unfortunately beyond current technologies.

As is usual in network neuroscience, we focus here on macro-scale connectivity, which considers brain connectivity between large-scale brain regions as opposed to neurons. In these large-scale networks brain regions are represented as nodes of a graph and the edges denote either structural or functional connectivity between these regions. More recently, multiplex (or, more generally, multilayered) networks have been used to construct large-scale structure-function models of the brain [40]. Such an approach has the potential to understand multi-scale neural behaviour by forming multilayered models across different scales.

Structural (or anatomical) brain networks describe the physical connections within the brain. The most common technique for computing brain networks for humans is to use diffusion magnetic resonance imaging (dMRI) [41]. This technique works by detecting differences in the diffusion of water molecules in drawn out structures such as the white matter fibres that make up the long-range wiring within the brain; water molecules diffuse faster along these bundles rather than perpendicular to them, and MRI techniques are capable of picking up these differences and hence determine the location of white matter connections. There are other techniques for finding the anatomical network of a brain such as tract tracing and electron microscopy, importantly, unlike the non-invasive techniques described previously, such methods are capable of inferring directionality [42, 43]. Electron microscopy is one of the oldest and best established way of providing the structural information of the brain. In this method the brain is cut

into thin slices, which are then examined by electron microscopy and pieced back together to give a 3D image of the structure. This, however, is a lengthy process and can still take an extended amount of time, even with the aid of computer programs. Another common technique is to use staining, this is where brain slices are stained with coloured dyes making the brain cells visible and neurons stand out from the surrounding tissue which is then examined with optical microscopy [44]. Nowadays the use of genetically modified mice is becoming common practice, where mice have a fluorescent protein used as a marker within the brain that emits visible light when illuminated under a UV light, which can then be observed and analysed to recreate the network [45]. Another common approach to find the underlying structural brain network is to use tracing, it works by injecting a tracer molecule into the brain where it then gets absorbed. Once absorbed it can be transported one of two ways; either forwards along the axons and through to neighbouring cells via synapses or backwards from synapses to the cell. The tracer is tagged with a fluorescent protein which leaves a path meaning the final path can be seen and the connections can be put together to create the structural network. Importantly, these invasive methods allow for the detection of directionality in the observed connections of the brain for a range of mammalian species. A useful resource for connectomics data is the brain connectivity toolbox (BCT), which consists of a number of MATLAB routines for performing network analysis as well as connectomes for a range of species.

Any network representation of the brain requires a so-called brain parcellation to be constructed such that the brain is divided into defined sections. These sections are close, interacting parts of the brain that are considered as fundamental units. The brain can be parcellated; however, there is no set way of describing the connectome and so different parcellations are used in practice. A brain parcellation typically consists of a subdivision of the brain into logical parts that all act in a similar way, are similar structurally and tend to be used for the same function *i.e* vision or motor skills. Different connectome maps still have the expected properties such as the networks are still small-world and scale-free; however, network analyses have also shown to differ significantly based on the type of parcellation used [46].

Functional networks are obtained by measuring similarities in neural activities across brain regions, *e.g.* correlations in time series of measured neural signals. One of the most common ways to create a functional network is by using data from a variety of measures such as functional magnetic resonance imaging (fMRI) [47]. fMRI is a time resolved imaging technique that picks out related brain activity of living brains in real time, it does this by measuring the blood oxygen level which increases during activity in functioning areas of the brain causing them to ‘light up’ on the MRI image. Other common measures include Electroencephalography (EEG) [48, 49] which measures electrical signals around the recording sites and Magnetoencephalography (MEG) [50] which measures the magnetic field around recording sites in the brain [51, 52]. The benefit of fMRI over the others is that EEG and MEG only measure cortical activity, which is the activity occurring in the top layer of the brain known as the cortex; fMRI can look deeper into the brain, past the cortex. Another problem with EEG is that it can quite often be affected by the noise of unavoidable tasks such as blinking and swallowing [53]. However unlike diffusion MRI these techniques do not directly measure the network connections, instead this is decided by observing correlations. A time series is obtained from these methods and from that we measure the strength of the statistical relationship between different areas of the brain. There are many different methods to measure correlation or coherence for example Pearson’s correlation coefficient or phase coherence [54, 55]. These techniques result in a matrix of pairwise similarities, from which we can infer a weighted network, in which the weights of the edges are related to the strength of the correlation between the activities of the relevant brain regions (nodes). We can then choose (if we wish) to threshold the network in a number of ways such as choosing a significant edge weight and removing any edges whose weights fall below this value. Other ways of thresholding a network include choosing the number of edges wanted within a chosen network, or listing the values from strongest connection to weakest and selecting a percentage (typically 20-30%) of strongest links to form a list to become edges within the network.

Another type of brain network is that of effective connectivity [56]. It measures the influences that nodes have over other nodes within a network model. To determine

this connectivity the system would be analysed using a measure capable of inferring causality amongst a collection of time series; however, despite the importance of these methods to our work we put off a thorough discussion of such techniques until Chapter 2.

1.2.2 Directionality in neural networks

Directionality is an important and often overlooked aspect of brain networks. Naturally, brains are directed. This is because within the brain there are chemical synapses which have predetermined transmitters and receivers, hence the chemicals flow one way, from the transmitter of one synapse to the receiver of another. Direction is rarely investigated as the methods to obtain the data are intrusive. Methods such as electron microscopy and tract tracing involve slicing the brain and examining it underneath a microscope. This means that there is little information on the direction of the connections within the human brain, as these are mapped with non-invasive techniques, and although they have improved in the level of detail that can be found they are still unable to determine direction at present. Therefore papers which analyse the human connectome are potentially flawed as they neglect a fundamental aspect of biology. Despite having the information available for analysis on animal connectomes they too are still often analysed with undirected networks as to discover underlying information about brain networks and so these too are also potentially flawed. Many of the network measures and characteristics that have been found within the connectome [57] are dependent on the directionality of the connections in the networks. Therefore it is important to address this gap in knowledge and understand the extent of its impact. The main aim of this work is to explore the effect that directionality has on brain network dynamics.

Kale *et al* questioned the reliability of undirected connectomes by evaluating a range of species and parcellations using network analysis and comparing the directed (or empirical) and undirected cortical network results [58]. Their findings demonstrate that adding in extra edges (reciprocal edges) thus making a directed network undirected leads to larger errors than if you remove edges to make a network undirected. This

suggests that errors can be made when classifying and identifying nodes such as hub and peripheral nodes, meaning large consequences as these can have important roles within brain function. This work focuses on characterising the effect of network directionality on structural brain networks; however, the extent to which perturbations to the directionality of connections influence neural activity on large-scale connectomes has yet to be addressed. The majority of work in this direction has centred on the dynamics of small circuits, such as network motifs [59].

1.2.3 Network models of large-scale neural activity

Computational models have been closely linked to neuroscience for a number of years, beginning with the spiking model of Hodgkin and Huxley in the 1950s [60]. Their model consisted of a set of non-linear ODES describing the temporal evolution of the membrane potential, and was derived from so-called clamping experiments on the giant squid axon. This work was the foundation of the family of models known as spiking neuron models [61, 62]. In 1982, Hopfield introduced an artificial neural network which replicated how the human brain stores and retrieves memories. In this model, a neuron is either on or off (firing or not firing) which is a huge simplification of how the brain works; however, the model is capable of being trained to learn patterns and then recognise slightly corrupted patterns. Since then computational models have continued to grow in numbers and complexity so that the brain may be represented to suit the requirements desired, including large scale functional patterns within the brain. By using computational models that examine large-scale activity, we can view the overriding dynamics that occur. To model this larger-scale behaviour, many authors tend to use neural mass models, such as Wilson-Cowan [63], Jansen-Rit [64] and Stuart-Landau [65], since they better replicate neural rhythms such as those observed in EEG recordings. Unlike the spiking neuron models discussed above, these models describe the collective neuronal behaviour of large groups of neurons together thus providing an average activity level for larger brain regions. By using these models we can visualise and understand what is happening within the brain at a larger scale to that of single spiking neurons and they are more realistic at the scales we examine.

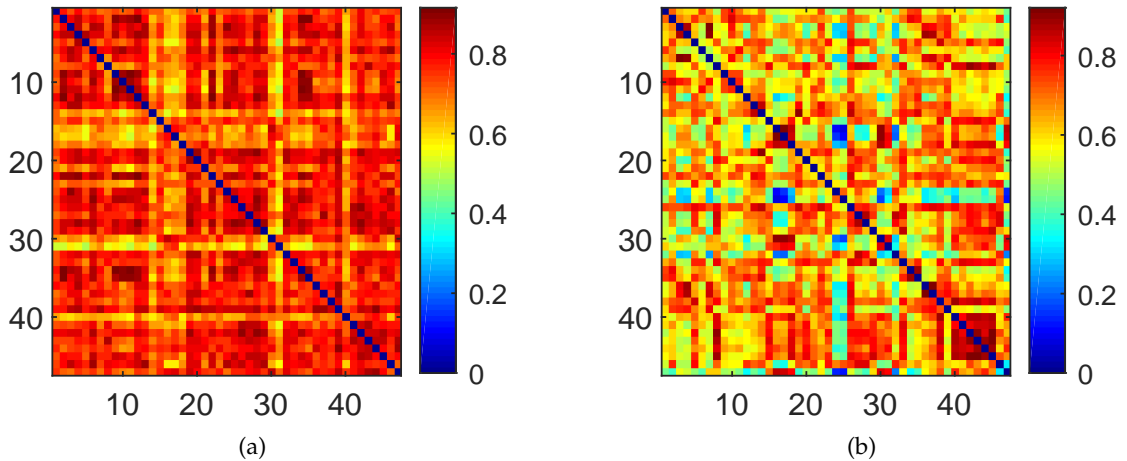


Figure 1.2: Comparison of functional connectivity networks for simulated dynamics using the Wilson-Cowan model (two different parameter sets) and coupled via the anatomical connectivity of the Macaque monkey.

Neural mass models usually describe local populations of interacting neurons; most commonly they describe the excitatory and inhibitory behaviour of the collective neurons [66]. Within these models each node has complex dynamics from the population behaviours as well as influence from other nodes within the network. They can be coupled to a large scale brain by using an anatomically informed connectome. These can be found in a variety of places, one of which is CoCoMac [67], which is a collation of invasive tract tracing studies that enable us to better understand the primates' brains. Creating a functional network this way means that we gain valuable insight into the functional patterns of correlated areas of the brain, meaning that by using the connectome alongside the generated functional network we can analyse structure-function relationships using these brain network models [68]. Figure 1.2 shows two simulated functional networks with dynamics simulated using the neural mass model of Wilson and Cowan (two different parameter sets) and connectivity provided by the anatomical network for the Macaque monkey.

These models are dynamical systems and are capable of generating diverse dynamical behaviours that closely match observed neural activity in the brain, such as oscillations and multistability. Multistability is an interesting area of dynamics and it is believed to play an important role within the brain that can help us understand large-scale patterns that occur [69]. To begin to understand multistability we first need to understand stability. An attractor, which could be of varying nature for example a fixed point or

a limit cycle, has unique basin of attraction. This is said to be stable if after a small perturbation it returns to the same attractor; if a system has multiple of these stable states its said to be multistable. However, large perturbations can knock the system from one basin of attraction to another meaning it changes the attractor it is drawn to. Within the brain this has been hypothesised to equate to the brain being ‘knocked’ from a healthy state to an unhealthy one, or indeed to another healthy state (*e.g.* different resting states). Resting state data studies have shown that healthy brains constantly switch between various resting states showing that the brain is multistable as well as dynamic even when the brain is at rest (meaning there is no task and the brain has no stimulation) [70].

The virtual brain (TVB) is a neuroinformatics software that simulates brain activity by using realistic biological data for the connectivity matrices within the framework [71]. It has a variety of information included such as time delays and connection strength in order to make networks biologically realistic. The package also holds many different neural mass models which can be used alongside the tractography data they supply. Together this defines the virtual brain. It can be used to generate time series which simulate brain activity similar to that of data from imaging techniques such as EEG, MEG or fMRI. It then can also be used to analyse this data and can seamlessly interact with other well known toolboxes via MATLAB such as the Brain Connectivity Toolbox (BCT) [72]. More information can be found in papers such as [73, 74] that go into depth on how to use and understand this platform and simulator.

1.2.4 Brain networks and disease

Brain networks (both healthy and diseased) have been shown to display many common features such as small-worldness [75], the existence of hubs [76] and a hierarchically modular structure [77]. Importantly recent studies have found that a number of brain diseases result from a breakdown in the above features, which are believed to be crucial for the efficient transfer of information in the brain [78, 79]. Schizophrenia, for example, has been reported to involve significant changes to network architecture, as compared to healthy controls. For example, in the study by Liu *et al.* [80] it was found

that the small-world architecture of the brain was disrupted in people with schizophrenia, largely due to an increase in the distance between nodes, or brain regions, in the networks. Indeed, it has been postulated recently that schizophrenia is a disorder of brain network disorganisation [81].

Another neurological disorder that has received considerable attention is Alzheimer's disease (AD). Research has shown that the structural brain networks of those patients with AD display abnormal small-world features with increased local clustering, meaning AD patients' brain networks have a less than optimal organisation [82]. It has been argued that the spread of disease can be linked to the attack of important hub networks during the early stages of the disease [83]. Not only does AD attack hub nodes but also the functional connections within modules, this degeneration of both hub nodes and the modular structure correlates with patients' cognitive ability [84]. By using network neuroscience within diseases such as AD we can highlight the differences between diseased and healthy brains, meaning physical bio-markers can be made known to further researchers.

Epilepsy is a dynamic brain disorder that affects approximately 1% of the world's population. Its main symptom is seizures, which are the spread of uncontrolled neural activity. It has been known for a while that changes in the brain's structure can lead to abnormal brain function such as epileptic seizures, as well as other neurological disorders [85]. Neuroimaging techniques are improving, meaning we have greater insight into the structural networks and the differences between healthy and diseased brains have become better quantified using network measures; for example, the clustering coefficient has been shown to increase in certain areas of epileptic patients' brains [86]. Computational models have been used to simulate corresponding functional networks, and examining structural and functional networks together has yielded greater understanding into epilepsy and other diseases [87, 88]. There are several different types of epilepsy and, although it normally cannot be cured, it can be controlled with anti-epileptic drugs and these are effective in 60–70% of individuals [89]. However, this is not always successful and in some cases surgery is the only option left. In surgery it is common to remove the part of the brain that is 'linked' to the origin of seizures

in most epileptic patients, and the success rate of patients can vary significantly [90]. An active area in network neuroscience, computer modelling of epilepsy using brain network models, attempts to predict surgical outcomes for patients with focal epilepsy with success which can aid clinicians in presurgery consultations [91]. Another important research area is in the prediction and control of seizures using implantable devices. Network methods have recently been shown capable of detecting seizure onset deploying so-called time-dependent network approaches. In one study by Kramer *et al.* [92], it was shown that functional networks evolve through distinct topological phases during seizure progression: a large, densely connected set of nodes dominate at seizure onset, and just prior to termination, but during seizures this densely connected component is fractured into a number of smaller modules.

Note that whilst we have provided some examples above on how networks can be applied to study brain disorders we have only touched on what is a huge subject area. An excellent recent overview of the state-of-the-art in network neuroscience and its application to psychiatry is given in the review by Alexander *et al.* [93]. Another important note is that the aforementioned studies almost exclusively ignore directionality and so it is very important to determine the impact of structural direction on network dynamics in order to understand how directionality might impact and influence the results and studies mentioned.

1.3 Thesis overview

In this thesis we apply techniques of network science in order to better understand structure-function relationships in the brain, and the impact that these can have on one another. More specifically, we aim to discover the impact that directionality of a structural brain network can have on the dynamic properties sub-serving brain function. Below we outline the structure of the remainder of the thesis.

In Chapter 2, we delve deeper into the preliminaries of network science, providing definitions of specific relevance to this project within network science. Within this we look at different network measures that can be used to analyse a system as well as

the different network models that can be used. In Chapter 3 we analyse systematically the effect that network directionality has on the brain's ability to store network patterns. More specifically, activity of neural subunits is described by a deterministic, graded response Hopfield model with connectivity defined via physiologically-relevant structural connectomes across a range of species and parcellations. The capacity of connectome-based networks to store patterns is interrogated by determining large numbers of fixed-point attractor sets for both directed and undirected connectomes (obtained via the addition of reciprocal connections) under systematic variation of model parameters. Moreover, we quantify the robustness of said patterns using the basin stability approach, which uses the basin of attraction to assess a steady state's stability in a probabilistic sense (*i.e.* it provides the likelihood of returning to a steady state under a random, non-small perturbation). Importantly, our approach enables us to determine the extent to which directed network topology influences multistability within connectome-based networks, as well as allowing us to quantify the affect that directionality has on the robustness of neuronal activity patterns in the brain. In Chapter 4 we question whether a significant change such as the addition of direction to the structural network will have a significant impact on the resulting directed functional network [94]. We hypothesise that neglecting direction from the structural connectome will have a major impact on the resulting functional brain networks as measured by Granger causality (GC), single transfer entropy (STE) or directed phase lag index (dPLI). Here, we focus on dPLI as it is a simple measure which has been proven to have similar outcomes to that of GC and STE without the complexity that those measures bring [95, 96]. We also follow on from several papers which have also used dPLI as a comparison measure in studying directionality [94, 96]. Finally, in Chapter 5 we conclude with a summary of the work presented and provide a discussion of possible ongoing research in this area.

Network preliminaries

In this Chapter we provide a mathematical overview of some of the most important areas in network science, with especial focus on those areas of most use in our work. We start by exploring the definitions of a graph or network and we then study the different network measures which will be used throughout this thesis. Subsequently we look at some classic network models that are commonly used within network science before discussing some further topics of interest such as modularity that we use later in this thesis.

2.1 Networks

A network, or graph, is a pair $N = (V, E)$ consisting of a set of vertices (or "nodes") V and a set of edges $E \subset V \times V$, in which $v_i, v_j \in V$ are connected in N if there exists an edge $e = (v_i, v_j) \in E$. The cardinality of the sets V and E , denoted $n = |V|$ and $m = |E|$, respectively, count the number of nodes and edges of the network. There are many different types of network; we discuss a few including the key example of directed networks below.

2.1.1 Weighted networks

In real world networks connections can have varying strengths or weights. To include this in the network structure we define a weighted network by considering a graph

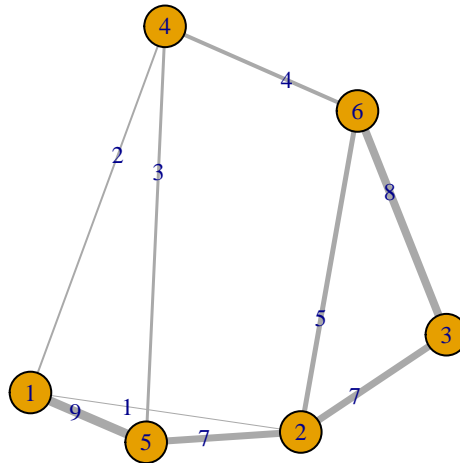


Figure 2.1: An example of a weighted network. Here, edge thickness varies in regard to the edge weight.

$G = (V, E)$ along with a weight function $w : E \rightarrow \mathbb{R}$, mapping each edge to the real number line. In neuroscience, for example, weighted networks are often used to define a structural brain network derived from diffusion tensor imaging (DTI) experiments thus resulting in a complete, weighted network, where the weights can be considered as probabilities describing the likelihood that two nodes, or brain regions, are connected. It is common practice for studies in network neuroscience to consider binary brain networks, using some thresholding scheme to convert real numbers to zeroes and ones. Figure 2.1 shows an example of a weighted network in which the edge thickness represents the weight of the edge.

2.1.2 Directed networks

As already discussed in Chapter 1, directed networks are prevalent within neuroscience but often overlooked. The majority of experimental techniques are incapable of inferring whether or not a connection is directed, either structural or functional, and so, again, the default is to consider undirected representations only – although in the case of functional connectivity studies, statistical techniques such as dynamic causal modelling and Granger causality can be used to infer directionality [56, 97, 98]. A directed network is one in which connections are not mutual, meaning that a connection can occur one way and not the other. For example chemical synapses within the brain only fire one way, meaning there is natural direction in the brain. Mathematically, we say

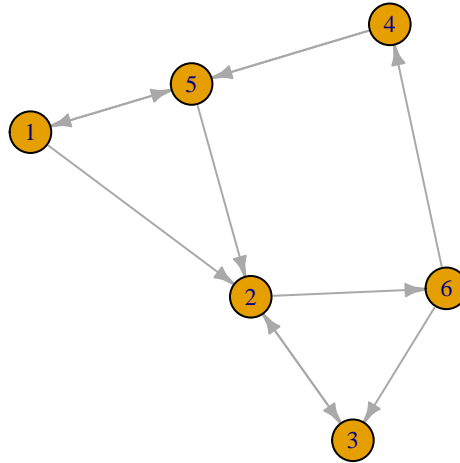


Figure 2.2: An example of a directed network. Here, the arrows show the direction of the connection between nodes.

that a network is *undirected* if $(v_i, v_j) \in E$ then necessarily $(v_j, v_i) \in E$; otherwise it is *directed*. Figure 2.2 shows an example of a directed network in which the arrows show the direction of the edges.

2.1.3 Adjacency matrices

The most common way to represent a network is by its *adjacency matrix*, which is an $n \times n$ matrix given by, A , with entries

$$a_{ij} = \begin{cases} 1, & i \sim j, \\ 0, & \text{otherwise.} \end{cases} \quad (2.1)$$

Here, \sim denotes that nodes i and j are adjacent, *i.e.* they are connected by an edge, in an undirected network. In a directed network, \sim would denote a connection from node i to node j , rather than a connection going both ways. The above formulation assumes that the connections between nodes are binary, or unweighted, which for most real-world systems is not the case as discussed above. Clearly, the adjacency matrix of an undirected network is symmetric, *i.e.* $A = A^T$.

An abundance of network models in neuroscience, and biology more widely, are modelled as so-called *simple networks*, that is they are unweighted, undirected networks that contain no self-loops or multiple edges. However, clearly many biological systems are

more naturally described using more complicated mathematical objects, *e.g.* hypernetworks, multiplex networks, or more generally, multilayered networks. The brain in particular, has recently been modelled as a multilayered network, in which different layers represent either structure and function [33, 99], or the different frequency bands at which the brain operates [34, 100].

2.2 Network measures

In this section we introduce the network measures considered in our experiments for both undirected and directed forms. See the books by Estrada [101] and Newman [102] for a more general introduction to network measures and for additional details on the measures introduced here.

Degree

The degree of a node is the number of connections the node has or in terms of the adjacency matrix

$$k_i = \sum_j a_{ij}. \quad (2.2)$$

In directed networks there are a number of different degrees. The *in-degree* is the number of connections into the node, the *out-degree* is the number of connections out of the node and the total degree is the sum of the in- and out-degrees:

$$k_i^{\text{in}} = \sum_j a_{ji} \quad k_i^{\text{out}} = \sum_j a_{ij}, \quad (2.3)$$

and

$$k_i^{\text{tot}} = k_i^{\text{in}} + k_i^{\text{out}}. \quad (2.4)$$

Often the mean, or characteristic, degree is used as a global measure of connectivity and is given by

$$\langle k \rangle = \frac{1}{n} \sum_{i=1}^n k_i = \frac{1}{n} \sum_{ij} a_{ij} = \frac{2m}{n}, \quad (2.5)$$

where m is the number of edges. Note that a similar result holds for directed networks.

Shortest and average path-length

The *distance* $d(i, j)$ between two nodes i and j is the length of the shortest path connecting the nodes i and j . The matrix $D = (d_{ij})$ is called the *distance matrix*. For simple networks (a graph that is unweighted and contains no self loops, undirected), D is a symmetric matrix, *i.e.* the distance between i and j is the same as the distance between j and i . The *characteristic path-length* is the average geodesic distance over all pairs of nodes in the network and is given by

$$\langle l \rangle = \frac{1}{n(n-1)} \sum_{i,j} d(i, j). \quad (2.6)$$

This particular measure is historically important in neuroscience since a short characteristic path-length is indicative of efficient transfer of information in such systems.

Triadic structures

Triangle counting is an important problem in network mining and is used in determining a number of different network measures. A triangle in a network is defined as a path of length 3 starting and ending at the same node (*i.e.* a 3-cycle). To compute the number of triangles we can use the following observation concerning the number of walks (*i.e.* network traversals [101]) in a network:

$$\left(A^k \right)_{ij} = \sum_{r_1=1}^n \sum_{r_2=1}^n \cdots \sum_{r_{k-1}=1}^n a_{i,r_1} a_{r_1,r_2} \cdots a_{r_{k-2},r_{k-1}} a_{r_{k-1},j}, \quad (2.7)$$

counts the number of walks of length k that start at node i and end at node j – this result is easily proved by induction.

Using this result we can count the number of triangles centred on node i in a network as

$$\Delta(i) = \frac{1}{2} (A^3)_{ii}. \quad (2.8)$$

The total number of triangles in an undirected network is given by

$$\Delta = \frac{\text{Trace}(A^3)}{6}, \quad (2.9)$$

and directed network is given by

$$\Delta = \frac{\text{Trace}(A^3)}{3}. \quad (2.10)$$

Note that when dealing with a directed network the above equations generalise immediately to count directed 3-cycles – although sometimes we might wish to count more general triadic structures in which case the formulae need to be refined [103].

Clustering coefficient

Clustering describes the interconnectedness of a node's nearest neighbours. For example, consider a friendship network. Such a network typically forms lots of small cliques due to fact that friendship occurs much more frequently amongst a friends' friends than it does between random people in the network. Thus, friendship networks exhibit large levels of 'clustering'.

In their seminal work on 'small-world' networks [21], Watts and Strogatz forwarded a new measure, which they termed the *local clustering coefficient*, that quantifies the extent to which a network node is clustered. For a given node, they considered the ratio

$$C(i) = \frac{2\Delta(i)}{k_i(k_i - 1)}. \quad (2.11)$$

Here, k_i is the degree of node i and the quantity $k_i(k_i - 1)/2$ counts the number of connected triples (a pair of edges with a shared node) centred on node i . Informally, $C(i)$ measures the 'cliquishness' of the network; it tells you the likelihood that a nodes neighbours are connected.

As mentioned above, there are a number of different ways of counting triangles in a directed network and so this results in multiple versions of the clustering coefficient

for a directed network [103]. For example, if we include all triangles, of all directions, then the resulting coefficient is given by

$$C_i = \frac{(A + A^T)_{ii}^3}{(k_i^{\text{tot}})(k_i^{\text{tot}} - 1) - 2A_{ii}^2}. \quad (2.12)$$

This is the equation we use throughout this thesis to calculate directed clustering coefficient. See reference [103] for definitions of the other possibilities.

As is common in network science, a global measure of clustering is provided by taking an average over all nodes, *i.e.* the *global clustering coefficient* is given by

$$\langle C \rangle = \frac{1}{n} \sum_{i=1}^n C(i). \quad (2.13)$$

Global efficiency

The efficiency of a network measures how effectively the network can exchange information, which is, for obvious reasons, an important measure in network neuroscience. It is a useful measure as, unlike distance, efficiency does not explode for disconnected nodes:

$$e = \frac{1}{n(n-1)} \sum_{i,j,i \neq j} \frac{1}{d(i,j)}. \quad (2.14)$$

It can be used to measure the small-world phenomenon within a network as it can give an idea into how the shortcuts in the network can help reduce inefficiency when passing information through the network. Such a measure is particularly relevant to neuroscience since it quantifies the efficiency of information transfer in cortical networks from a parallel processing perspective.

2.2.1 Measuring network centrality

Centrality measures are a very useful way to find important nodes within a network. The different measures can identify contrasting important nodes depending on the chosen definition of important. Below we outline some historically important centrality measures (see the book by Estrada[101] for further examples).

Degree centrality

Degree centrality is a simple measure which orders the importance of nodes via the number of connections. This is a simple measure to calculate as we use Equation (2.2) to find each node degree, then rank nodes from highest degree as most important to lowest degree being least important.

Betweenness centrality

Betweenness centrality measures nodes that connect important regions within the network. The algorithm for computing the betweenness centrality of node i , is to calculate the shortest path between between all other pair of nodes and calculate the fraction of them that pass through node i .

$$b(i) = \sum_{j,k} \frac{\alpha_{kj}(i)}{\alpha_{kj}} \quad (2.15)$$

where α_{kj} is the number of shortest paths from k to j and $\alpha_{kj}(i)$ is the amount of those shortest paths that pass through node i . This can also be normalised so that the calculation lies between 0 and 1, to do this we divide by the number of pairs of nodes not including node i . So for directed networks $(n - 1)(n - 2)$ and undirected networks $(n - 1)(n - 2)/2$. Figure 2.3 shows an example of betweenness centrality where nodes 2 and 6 would have very high betweenness centrality values as they are both important bridging nodes to other parts of the network, where as node 7 would have a low value with it being a peripheral node [57].

Eigenvector centrality

Eigenvector centrality measures the influence a node has on the network by assessing the connected nodes, if the connected nodes also have high influence it increases the score whereas a node connected to a low influencing node the score will decrease. So it places importance onto the connections of a node rather than the credit of that individual node. The measure is calculated via the eigenvectors of the adjacency matrix as

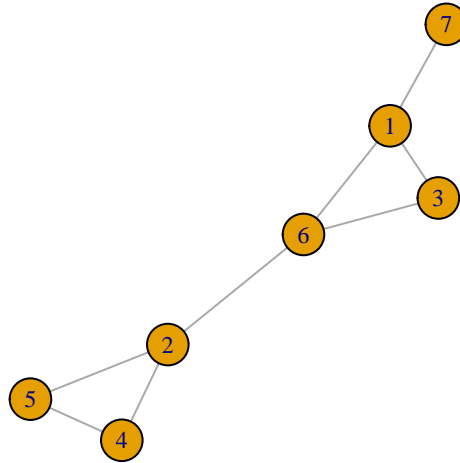


Figure 2.3: An example of two nodes with high betweenness values. Nodes 2 and 6 have a connection between them which connects two important regions of the network.

follows:

$$\lambda_1 e(i) = \sum_j A_{ij} e(j), \quad (2.16)$$

where λ_1 is the largest eigenvalue of A , which is guaranteed by Perron–Frobenius theorem, the proof that a square matrix with real values will always have a unique largest eigenvalue [104]. The centrality score of the vertex i is then given by the i^{th} component of the related eigenvector.

2.3 Network models

For completeness we consider here briefly three different network models that have had a significant impact in network science and network neuroscience in particular.

2.3.1 Erdős-Rényi random graphs

As discussed in Chapter 1, Erdős and Rényi explored a new type of graph, named *Erdős-Rényi random graphs* (ER) [15]. They introduced $G(n, p)$ as a collection of networks having n nodes such that all pairs of nodes were connected with probability p . So, for example as seen in Figure 2.4, when $p = 0$ a null network containing no edges would be created. For increasing values of p the networks become increasingly dense until at a certain point a *giant connected component* forms [105, 106]; further increasing

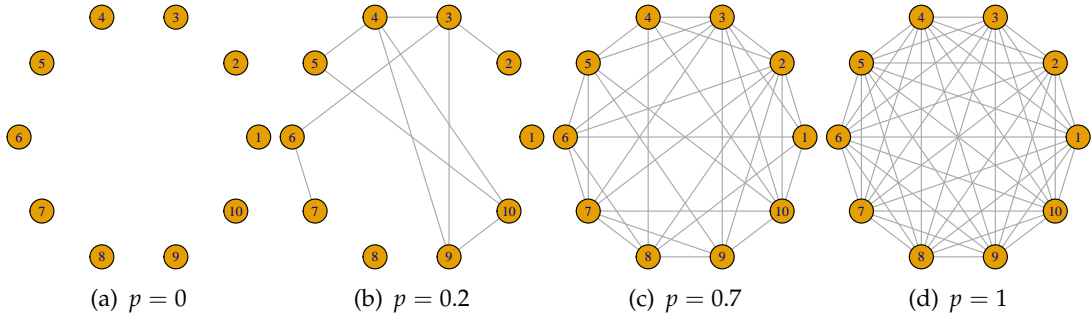


Figure 2.4: Increasing value of p to increase connections in an ER random graph.

p the networks tend towards a complete network. A considerable amount of research has gone into understanding the ER random graph model and so, for example, it is well known that their degree distribution is binomial, given by

$$P(k) = \binom{n}{k} p^k (1-p)^{n-1-k} \quad (2.17)$$

and that in the large n limit this distribution is well approximated by a Poisson distribution of the form

$$P(k) = e^{-\langle k \rangle} \frac{\langle k \rangle^k}{k!}. \quad (2.18)$$

Note that we require $\langle k \rangle$ to remain bounded in the above limit.

Importantly, both the clustering coefficient and average path-length are known for ER random graphs [107]:

$$l \sim \frac{\log n}{\log \langle k \rangle} \quad \text{and} \quad C = p \approx \frac{\langle k \rangle}{n}. \quad (2.19)$$

Note contrasting the above against real-world networks shows that ER random graphs are not ideal to be used for modelling real-world networks.

Perhaps the most common use of ER networks is as null models by which to compare results for real-world networks against. It is particularly common in neuroscience to use the following ratio to determine whether or not a network possesses the small-world property:

$$S = \frac{\gamma}{\lambda'}, \quad (2.20)$$

where

$$\gamma = \frac{C}{C_{\text{rand}}} \quad \text{and} \quad \lambda = \frac{l}{l_{\text{rand}}}. \quad (2.21)$$

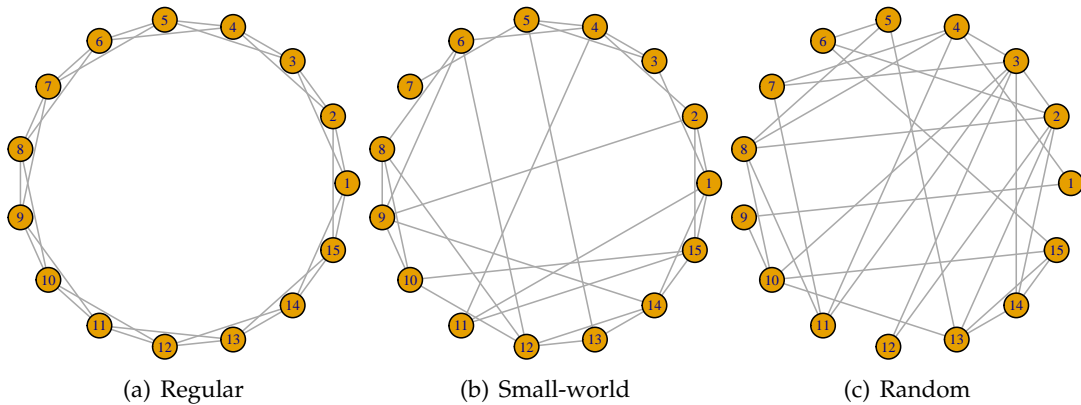


Figure 2.5: Increasing randomness changes a network from regular to random and through transition shows small-world properties.

In the above, C_{rand} and l_{rand} are the mean clustering and characteristic path-length for an ensemble of ER networks of the same order as the network of interest and we say that the network is small-world if $S \gg 1$.

2.3.2 Watts-Strogatz small-world model

Stanley Milgram’s experiment showed the first evidence of the small-world phenomenon, as explained in Chapter 1. From this, it was hypothesised that for a network to be considered ‘small-world’ the path length would need to be proportional to the log of the network size, specifically $l \propto \log(n)$. Real-world networks, however, tend to also display high levels of clustering, and so from a practical point of view we say a network is small-world if it has both small average path length whilst simultaneously having a large amount of clustering when compared to a ‘random’ network.

Watts and Strogatz thought up an idea to create a random network model that incorporates elements of both random and regular structures. Ideally taking the small average path length in classic random graphs whilst also having the clustering levels seen in regular networks. They created this by beginning with a k -regular lattice on n nodes and rewiring each edge or adding a new edge (depending on the algorithm used), with a set probability p so that each node is reconnected randomly to a different node. When $p = 0$ the network will still have a regular structure, as is the case with low values of p . However, as p increases so does the small-worldness of the network; we know that reg-

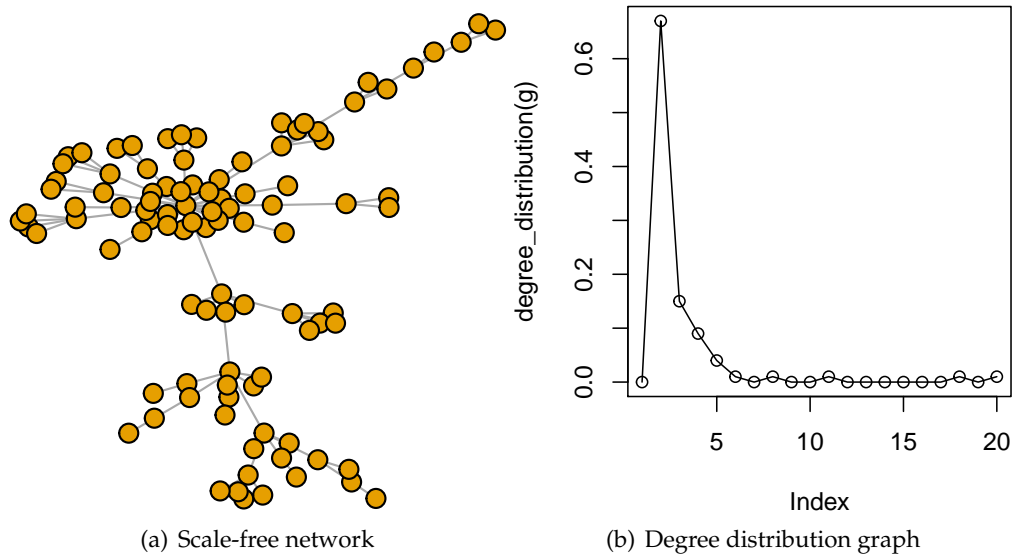


Figure 2.6: Scale-free network and the corresponding degree distribution graph.

ular networks have high levels of clustering already but adding short-cuts, we shorten the average path length and so traversing the network becomes easier and the small-worldness increases as can be seen in Figure 2.5. The result of this method is a random graph that has small-world properties, high clustering and small path length.

2.3.3 Barabási-Albert model

When studying the Erdős-Rényi and Watts-Strogatz models there is no thought to the degree distribution of the resulting networks. Within those network models the nodes are often homogeneous due to each node being treated the same; the issue here is that most real world degree distributions are not homogeneous but instead are heterogeneous. We often have few nodes with many connections, called *hub nodes*, and many nodes with few connections, called *periphery nodes*, this feature is typical of *scale-free* networks an example of which can be found in Figure 2.6. Barabási and Albert posited that this was a natural consequence of so-called *preferential attachment*, meaning that nodes have a preference to attach themselves to nodes with higher degree.

They set about creating a network model which could construct a network that was scale-free. This algorithm starts with a small initial network, adding nodes in each

iteration using this probability,

$$p(i) = \frac{k_i}{\sum_j k_j}. \quad (2.22)$$

The nodes follow the preferential attachment idea and so with that are more likely to attach to a node with higher degree already, creating a scale-free network. This model is often termed the preferential attachment model or the BA model.

2.4 Network modularity

It is common in real-world networks that some nodes will cluster together in groups called modules. Often this is due to them having similar characteristics, either structurally or functionally. These modules or communities are identifiable as having a high concentration of connections between nodes within a module and sparse connectivity with the rest of the network. Modularity plays an important role in network neuroscience due to the observed hierarchically modular organisation of both structural and functional networks. For example, it has been shown to impact the function of working memory capacity and declining brain modularity is related to aging in both healthy and diseased brains [108]. There is also a belief that the way the brain is organised in modules can mediate the relationship between task complexity and performance, the authors in [109], for example, showed that when a brain is more organised it has a negative correlation with scores from complex tasks but a positive correlation with scores from simple tasks, showing a link between brain organisation and cognitive processes.

Girvan and Newman first proposed modularity as a network measure [24]. They determine a partitioning of the node set V , *i.e.* a collection of sets $V_i \subset V$ with $V_i \cap V_j = \emptyset \forall i \neq j$ and $\cup_i V_i = V$, such that nodes in the same set are densely connected with each other, but sparsely connected with all other nodes. To measure the ‘quality’ of such a partition Girvan and Newman forwarded the following modularity score

$$Q = \frac{1}{4m} \sum_{r=1}^{n_p} \sum_{i,j=1}^n \left(a_{ij} - \frac{k_i k_j}{2m} \right) s_{ir} s_{jr}, \quad (2.23)$$

where m is the number of edges within the network, n_p is the number of sets within

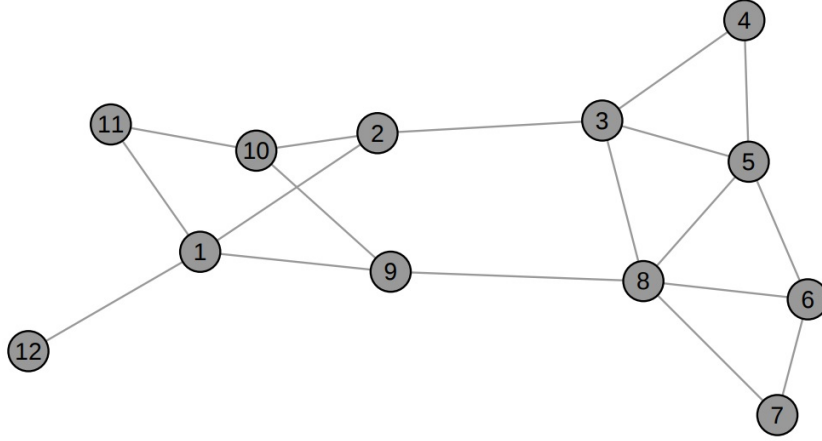


Figure 2.7: A network with two distinct modules.

our partition, a_{ij} equals 1 or 0 depending upon whether a connection exists between nodes i and j , k_i is the degree of node i and $s_{ir} = 1$ if node i is in the cluster r and $s_{ir} = 0$ if it is not. Incorporating directionality alters Equation (2.23) as follows:

$$Q = \frac{1}{2m} \sum_{ij} \left(A_{ij} - \frac{k_i^{in} k_j^{out}}{m} \right) (s_i s_j + 1) \quad (2.24)$$

Modularity can then be optimised over all partitions to understand the optimised community structure. Note that this measure is in general a computationally intractable problem.

A comprehensive overview of community detection algorithms for general complex networks is given in [110]; for a more recent neuroscience-specific review see [111]. Our focus here, is on the spectral community detection algorithm [112] due to Newman since we deploy it in Chapter 3 to determine modularity structure for connectomes across a range of species.

Spectral modularity maximisation is a method of obtaining modularity values and makes use of the eigenvectors of the matrices to approximate the divisions within a network [102, 112]. The method begins by splitting a network in two and introducing s_i which holds the value of either +1 or -1 dependent on if node i is in group 1 or 2 respectively. We can then use a vector form of (2.23) given by,

$$Q = \frac{1}{4m} \mathbf{s}^T B \mathbf{s}, \quad (2.25)$$

where s is a vector of the elements of s_i and B is the modularity matrix that is made up of the elements of B_{ij} where,

$$B_{ij} = A_{ij} - \frac{k_i k_j}{2m}. \quad (2.26)$$

In order to maximise the value of Q we must find the value of the vector s that maximises Equation (2.25) for given matrix B . Given that s_i is a discrete variable maximisation is trickier than usual, normally the usual tools of calculus would suffice, but as the problem is discrete we instead we use an approximation method. An approximation to this difficult discrete maximisation problem can be obtained via the method of relaxation, in which we replace the intractable discrete problem by a related continuous one, which is amenable to the tools of calculus. To this end we allow the vector s to take real entries so that we can find an approximation to maximise Q , not exact as the values may not be ± 1 , but will allow us to see the best way to split the network.

By considering the fact that the values of the vector s are binary and so they align with the corners of a hypercube, we can relax this by allowing the vector to point anywhere on the surface of a hypersphere with radius of \sqrt{n} . The length of the vector must stay the same and so

$$\sum_i s_i^2 = n. \quad (2.27)$$

The relaxed form means that the maximisation problem is elementary and is simply just a case of differentiating Equation (2.23) whilst using the new constraints given in Equation (2.27) with Lagrange multiplier λ :

$$\frac{\partial}{\partial s_i} \left[\sum_{jk} B_{jk} s_j s_k + \lambda \left(n - \sum_j s_j^2 \right) \right] = 0. \quad (2.28)$$

Thus, we obtain

$$\sum_j B_{ij} s_j = \lambda s_i, \quad (2.29)$$

or in vector form

$$B\mathbf{s} = \lambda\mathbf{s}. \quad (2.30)$$

Which means that the optimal s is one of the eigenvectors of the modularity matrix with

corresponding eigenvalue λ . Substituting Equation (2.30) into Equation (2.25) gives

$$Q = \frac{1}{4m} \lambda \mathbf{s}^T \mathbf{s} = \frac{n}{4m} \lambda, \quad (2.31)$$

which can be used to find the eigenvector which maximises our Q , by choosing the largest eigenvalue and using the corresponding eigenvector.

The elements of \mathbf{s} however we know are forced to only take the values of ± 1 and so we try and chose values of \mathbf{s} as close to our ideal as possible within these constraints. By minimising the angle between \mathbf{s} and the leading eigenvector which we will denote as \mathbf{u} . Alternatively we can just maximise the product $\mathbf{s}^T \mathbf{u} = \sum_i s_i u_i$ which is when for all i , $s_i u_i$ is positive which occurs when both s_i and u_i both have the same sign, if $u_i = 0$ we can chose either $s_i = \pm 1$. This creates an algorithm to then follow, firstly we calculate the eigenvector that corresponds to the largest eigenvalue, then use this vector to assign signs to each node which splits them into two modules or communities, positive signs in one community and negative in the other.

2.5 Summary

In this chapter we have given an overview of some of the most essential features of network science currently with a focus on the topics with most relevance to the work within this thesis. This review is not extensive as there are many areas we have not considered within this chapter. We have covered the basic mathematical concepts of graph theory and networks. We have also considered some of the different types of network models that exist and that can be created to make networks with various results and behaviours. We also examined how we can analyse networks by using measures such as centrality measures and extended our review to include information about modularity. For further details we recommend the following books and references therein [101, 102]. The concepts covered in this chapter will be examined for various relevant (directed and undirected) cortical networks in the subsequent chapters.

The impact of structural directionality on the computational properties of a neural network

The goal of this chapter is to extend work by Golos *et al.* [113] to analyse systematically the effect that network directionality has on the brain's ability to store network patterns. More specifically, activity of neural subunits is described by a deterministic, graded response Hopfield model [114] with connectivity defined via physiologically relevant structural connectomes across a range of species and parcellations. The capacity of connectome-based networks to store patterns is interrogated by determining large numbers of fixed-point attractor sets for both directed and undirected connectomes (obtained via the addition of reciprocal connections) under systematic variation of model parameters. Moreover, we quantify the robustness of said patterns using the basin stability approach forwarded by Menck *et al.* [115], which uses the basin of attraction to assess a steady state's stability in a probabilistic sense (*i.e.* it provides the likelihood of returning to a steady state under a random (non-small) perturbation). Importantly, our approach enables us to determine the extent to which directed network topology influences multistability within connectome-based networks, as well as allowing us to quantify the affect that directionality has on the robustness of neuronal activity patterns in the brain.

3.1 Brain network models

3.1.1 The Hopfield model

The Hopfield model was originally forwarded by J. J. Hopfield as a relatively simple description of the collective behaviour of a large ensemble of ‘neurons’ [114, 116]. In this section we give a brief description of the original Hopfield model [116] as well as the so-called ‘graded response’ model [114], which extends the original discrete model to the case of continuous variables and response. We then discuss an adaptation of the graded response model forwarded in [113] that we use throughout this chapter.

The original model

The original Hopfield model consists of n neurons, each of which can be in one of two states: an ‘on’ state or an ‘off’ state. Denoting the state of the i^{th} neuron as V_i (typically V_i will be taken as being either 1 or 0), the total input of the i^{th} neuron is given by

$$H_i = \sum_{j \neq i} A_{ij} V_j + I_i, \quad (3.1)$$

where the matrix A defines the neural architecture and any external inputs are given by I_i . Thus, each neuron receives two types of input: an external input and input from neighbouring neurons.

Each neuron updates its state according to the following probabilistic rule:

$$\begin{aligned} V_i &\longrightarrow 0 \text{ if } \sum_{j \neq i} A_{ij} V_j + I_i < \theta_i \\ &\longrightarrow 1 \text{ if } \sum_{j \neq i} A_{ij} V_j + I_i > \theta_i. \end{aligned} \quad (3.2)$$

The threshold θ_i determines the state of the i^{th} neuron. The state of the system updates at random and in an asynchronous manner. This asynchronicity is believed to better model important features of neural systems such as noise, delays and jitter [114, 116].

Importantly, it can be shown that the dynamics of an n -neuron Hopfield model (evolv-

ing according to (3.2)) always converges onto a stable steady state, regardless of the initial configuration. To see this, consider the following energy function:

$$E = -\frac{1}{2} \sum_i \sum_{j \neq i} A_{ij} V_i V_j - \sum_i I_i V_i + \sum_i \theta_i V_i.$$

Any change, ΔE , of the energy, E , due to a change in state ($V_i \rightarrow V_i'$) of the i^{th} node is given by

$$\Delta E = - \left[\sum_{i \neq j} A_{ij} V_j + I_i - U_i \right] \Delta V_i.$$

Now, according to the update rules in (3.2), ΔV_i is positive/negative only when the bracketed term in the above is positive/negative, thus any change in E under the algorithm in (3.2) is negative, and since E is bounded, iteration of the algorithm must converge to a stable steady state [114, 116]. The boundedness of E follows since the input is bounded and all other elements in each of the sums lie in the range $[0, 1]$.

The original Hopfield model as described above, serves as a model of associative memory in that it converges onto a set of stable steady states, each of which can be considered as content-addressable memory. Configurations that lie close to a steady state, or memory, can be thought of as partial information about that memory. Convergence of such an initial configuration to the aforementioned steady state implies that memory retrieval can be achieved even when only partial information of the memory is available; in this instance, we say that the memory is defined by its content as opposed to its location.

Graded response Hopfield model

Next, we consider the *graded response* Hopfield model, which is a time-continuous version of the model described previously. The graded response model originally considered by Hopfield is given by

$$C_i \frac{du_i}{dt} = \sum_j A_{ij} g_j(u_j) - u_i/R_i + I_i, \quad (3.3)$$

which is a resistance-capcitanace model of cell potential [114]. In (3.3), u_i describes the mean potential of the i^{th} neuron, C_i and R_i are the membrane capacitance and resistance, respectively of the i^{th} neuron, and as before I_i denotes any external inputs to neuron i . The function $g_i(x)$ describes the firing rate and is typically given by a sigmoidal function of the form

$$g(x) = \frac{1}{2} (1 + \tanh(x)), \quad (3.4)$$

but any monotonically increasing function in x that asymptotes at V_i^0 and V_i^1 is sufficient. (Note that for the above choice of g we have $V_i^0 = 0$ and $V_i^1 = 1$.)

Importantly, Hopfield showed that Equation (3.3) has energy E given by

$$E = \sum_i \left(-\frac{1}{2} \sum_j A_{ij} V_i V_j + \frac{1}{R_i} \int_0^{V_i} g_i^{-1}(V) dV + I_i V_i \right), \quad (3.5)$$

where $V_i = g(u_i)$. The minima of the energy function E determine the set of potential states (*i.e.* steady state solutions) supported by the model in (3.3). To see this, note that differentiating Equation (3.5) with respect to t gives:

$$\begin{aligned} \frac{dE}{dt} &= - \sum_i \frac{dV_i}{dt} \left(\sum_j A_{ij} V_j - \frac{u_i}{R_i} + I_i \right), \\ &= - \sum_i C_i \frac{dV_i}{dt} \frac{du_i}{dt}, \\ &= - \sum_i C_i g_i^{-1}(V_i) \left(\frac{dV_i}{dt} \right)^2, \end{aligned}$$

and since $g_i^{-1}(V_i)$ is a monotonically increasing function and C_i is positive, we have that either $dE/dt < 0$ or $dE/dt = 0$ in which case $dV_i/dt = 0$ for all i . Thus, the time evolution of (3.3) results in trajectories that seek out minima of the energy function in (3.5), in other words, the minima of E are in a one-to-one correspondence with the stable steady state solutions of (3.3). To further illustrate these points, in Figure 3.2 we have plotted the phase portrait and energy function for the adapted Hopfield model (see equations (3.6)–(3.7)) on an undirected, complete network on two nodes. The correspondence between fixed points of (3.3) and minima of (3.5) can be seen in

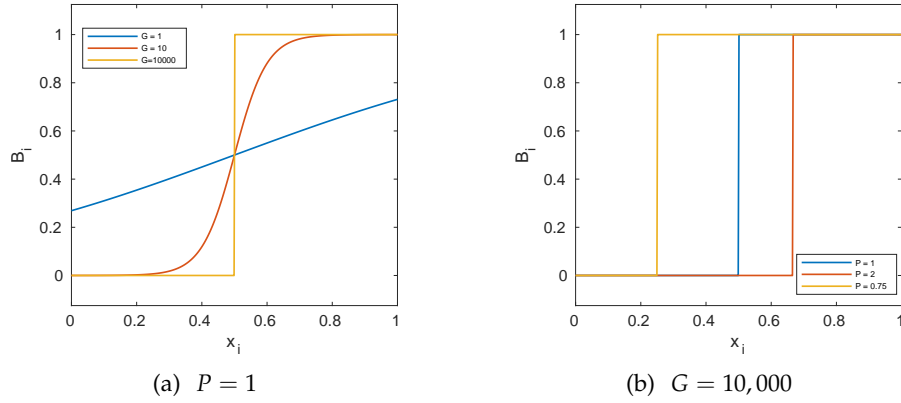


Figure 3.1: The firing rate function $g(x, \theta) = \frac{1}{2}(1 + \tanh(G(Px - \theta)))$ deployed in this chapter for various values of G and P and fixed $\theta = 0.5$.

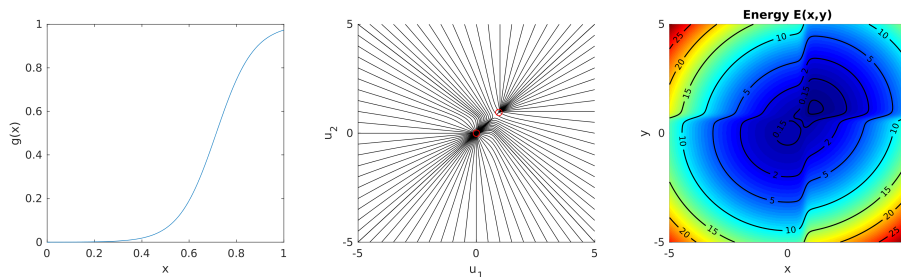


Figure 3.2: Phase portrait and energy landscape of the Hopfield model in (3.6)–(3.7) with $N = 2, G = 10, P = 1, \theta = 1/2$ and $C = 1$.

the plot by examining where the fixed points are in the middle figure, shown with red circles, also corresponds to where energy is at its lowest (dark blue) in the right side figure. Note that the stable equilibria (or fixed points) of the Hopfield model in (3.3) are in a one-to-one correspondence with the minimum energy configurations of (3.5) as is evident from figures.

Adaptation of the Hopfield model

In our experiments neural activity is described using a variation of the Hopfield graded response network model forwarded in [113]. This results in a dynamic network model consisting of n state variables x_1, x_2, \dots, x_n each describing the average neural activity

within a brain region (or neuron):

$$\tau \frac{dx_i}{dt} = -x_i + \sum_{j=1}^n w_{ji} g(x_j, \theta), \quad (3.6)$$

with

$$g(x, \theta) = \frac{1}{2} (1 + \tanh(G(Px - \theta))). \quad (3.7)$$

Here, τ is a relaxation time constant and the matrix W represents the normalised adjacency matrix, which is defined as

$$W = \frac{1}{\|A\|_1} A \in \mathbb{R}^{n \times n}. \quad (3.8)$$

In the above, we make use of the one-norm to ensure that each $x_i \in [0, 1]$ by:

$$g(x_j, \theta) \in [0, 1] \implies \sum_j w_{ji} g(x_j, \theta) \leq k_j^{\text{in}} = 1 \quad (3.9)$$

for the normalised adjacency matrix. Which for a matrix $A \in \mathbb{R}^{n \times n}$ is defined by

$$\|A\|_1 = \max_j \sum_{i=1}^n |a_{ij}| = \max_j k_j^{\text{in}},$$

where k_j^{in} denotes the in-degree of the j th node. This ensures that $x_i \in [0, 1]$ as the numbers within the matrix are divided by the maximum in degree from the network and so this means the maximum number will be 1 and as there are no negatives lowest value possible will be 0.

The function $g(x, \theta)$ in (3.7) is a sigmoidal function that represents the input-output relationship of each node – see Figure 3.1. The parameters G and P , which represent node excitability and the ratio of excitation over inhibition respectively, determine, alongside the activation threshold θ , the degree of multistability present within the system (3.6). Here, we follow [113] and define a global activation threshold given by

$$\theta = \frac{1}{2n} \sum_{i,j} w_{ji}. \quad (3.10)$$

The global activation threshold is a simplification of the original Hopfield model since each node uses the same activation threshold. In this simplified setting, nodes with larger in-degree have a larger probability of being active.

Importantly, the parameters G and P control the dynamical regime. More specifically, G is the system gain which controls the multistability of the system (see, for example, [113]). In our experiments we fixed $G = 10,000$ as such large values enhance multistability thus increasing the network's ability to support information. We then investigated the capacity of both directed and undirected connectomes to store patterns under systematic variation of the scaling factor P , since this parameter has previously been hypothesised to play an important role in determining attractor densities.

3.1.2 Structural connectivity

Network directionality is a fundamental feature of brain networks, yet due to experimental limitations it is typically omitted from network studies of the brain. Motivated by the study of Kale *et al.* [58], here, we investigate the influence that network directionality has on the information storing capacity of connectome-based networks for a variety of different organisms across a range of scales, including two different parcellations of the Macaque monkey cortex [117], a parcellation of the cat cortex [118] and a representation of the nervous system of *C. elegans*, which is a tiny round worm and the only organism to date for which the entire nervous system is mapped out [119, 120]. The Macaque and cat datasets are accessible via the Brain Connectivity Toolbox [57]. The *C. elegans* data is the same as that used in [121, 122] and is available from http://www.biological-networks.org/?page_id=25.

For the mammalian connectomes, nodes represent some predefined collection of brain tissue and edges encode the presence of long-range connections between pairs of brain regions; whilst for the *C. elegans* connectome, nodes represent individual neurons and edges between nodes represent synapses. For consistency in our experiments, edge weights were discarded (when present) resulting in a binary representation of each of the aforementioned connectomes, yielding a binary connectivity matrix $A \in \mathbb{R}^{n \times n}$ such that $a_{ij} = 1$ if brain region (neuron) i projects onto brain region (neuron) j , and is

otherwise zero. To obtain undirected versions of the connectomes all connections were made bidirectional resulting in a symmetric adjacency matrix given by

$$B = \text{sgn} \left(A + A^T \right),$$

where $\text{sgn}(x)$ denotes the sign function, which equals 1 for positive inputs, -1 for negative inputs and is otherwise 0. Below we provide further details of the connectomes studied in this work.

Macaque networks

The first Macaque connectivity network we consider is a representation consisting of $n = 71$ brain regions and $m = 876$ directed edges. The network combines the parcellation of the Macaque visual system due to Felleman and Van Essen [123] with that of Yeterian and Pandya [124], which also includes brain regions within the sensorimotor, motor and superior temporal cortices. The second Macaque connectome is the same as that studied in [122], which is based on three extensive neuroanatomical compilations [123, 125, 126] that collectively cover large parts of the cerebral cortex. It consists of $n = 95$ cortical areas and $m = 2390$ directed edges. The connectivity data for these networks were originally collated from the CoCoMac database [117] but we obtained them from the Brain Connectivity Toolbox [57].

Cat network

The matrix representing the cat connectome is that given by Scannell *et al.* [118], which is a collation of numerous studies and deploys the parcellation from [127, 128]. This results in a connectome with $n = 52$ brain regions and $m = 818$ directed edges.

C. elegans

The *C. elegans* nervous system considered here has $n = 277$ nodes and $m = 2105$ directed edges [121, 122]. This network is derived using electron microscopy and is the

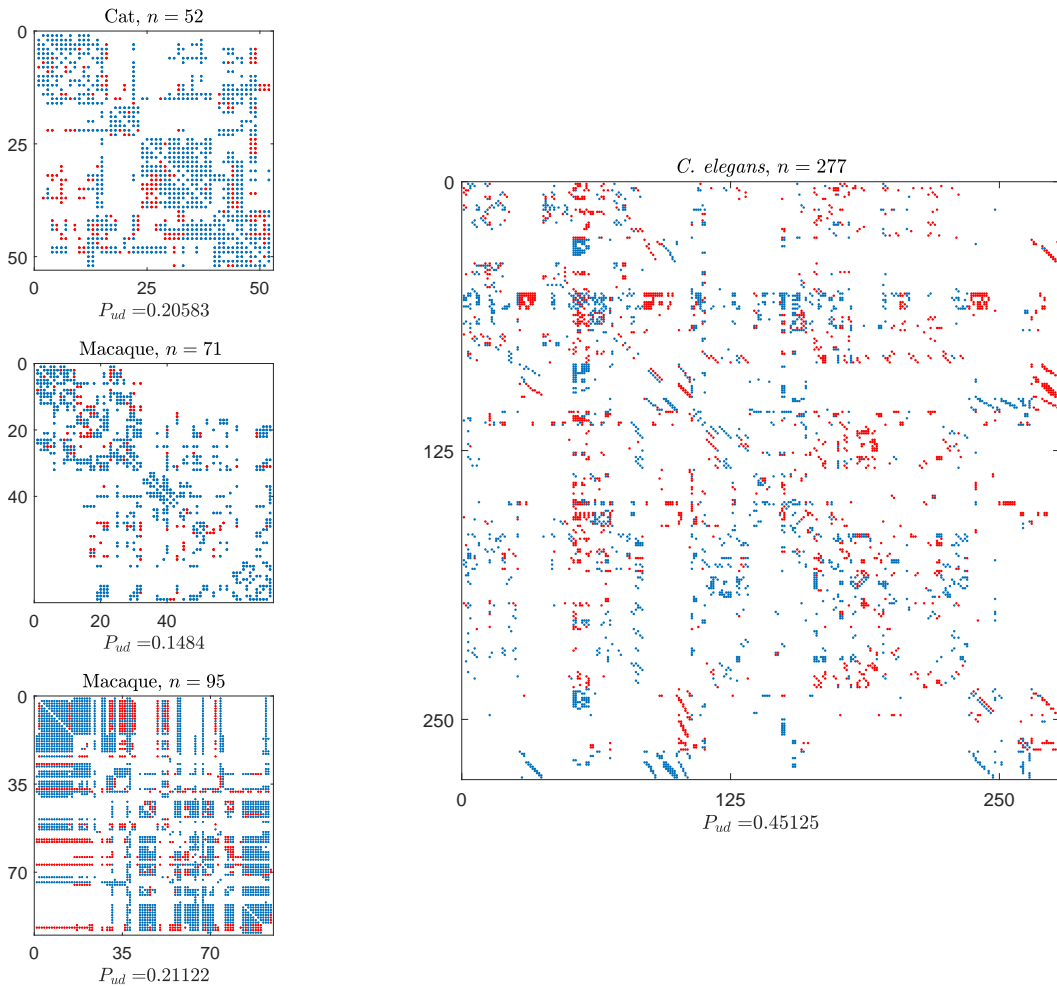


Figure 3.3: Spy plots of the adjacency matrices corresponding to the four connectomes studied in this work: two different parcellations of the macaque cortex, the cat cortex and the neuronal network for *C. elegans*. Directed connections are shown in blue. Reciprocal edges added to form the corresponding undirected networks are shown in red. The proportion of reciprocal edges, P_{ud} , is given below each network diagram.

only fully mapped nervous system to date. It has two types of connections: *chemical synapses*, which are directed, and *gap junctions*, which we treat as bidirectional since experimental techniques are unable to infer directionality in this case.

Figure 3.3 displays the four connectomes analysed in this study with reciprocal edges added to form the undirected representation of each connectome highlighted in red and the respective proportion of reciprocal edges stated below each connectome. Basic network statistics for both the empirical connectomes as well as their undirected representations are given in Table 3.1.

Connectome	Cat		M71		M95		CE	
	D	U	D	U	D	U	D	U
# of edges	818	515	746	438	2390	1515	2105	1918
mean degree	15.73	19.81	10.51	12.34	25.43	32.23	7.60	13.85
# of modules	4	3	4	4	3	3	6	5

Table 3.1: Network statistics for the original directed connectomes (D) and their undirected representations (U). Here, M71 and M95 denote the Macaque connectomes on 71 and 95 nodes, respectively, whilst CE denotes the *C. elegans* connectome.

3.2 Basin stability

For each network the dynamics are governed by the Hopfield model in (3.6). To determine the global stability of attractor states, we compute the *basin stability* [115] for each of the steady states of (3.6) as a function of the parameter P . This amounts to estimating the size of the basin of attraction $\mathcal{B}(\mathbf{x}^*)$ of each steady state, \mathbf{x}^* , of (3.6). Due to the computational challenges inherent in computing volumes of high-dimensional spaces the basin stability is computed in a relative sense, that is

$$S_{\mathcal{B}(\mathbf{x}^*)} = \mu(\mathcal{B}(\mathbf{x}^*)), \quad (3.11)$$

where μ is an appropriately defined measure over an appropriately chosen domain, Q say, containing all basins of attraction of all attractors. Typically, μ will be proportional to a volume and so $\mu(\mathcal{B}(\mathbf{x}^*)) \in [0, 1]$ is a proportion of state space. From a practical point-of-view, suppose that \mathbf{x}^* is an asymptotically stable equilibrium point of (3.6) with basin of attraction $\mathcal{B}(\mathbf{x}^*)$. Then we integrate (3.6) for N initial conditions drawn uniformly at random from Q and count the number, M , of initial conditions that converge to the fixed point \mathbf{x}^* , which provides the estimate M/N for the basin stability, $S_{\mathcal{B}(\mathbf{x}^*)}$, of the steady state \mathbf{x}^* .

3.3 Results

3.3.1 Network analysis

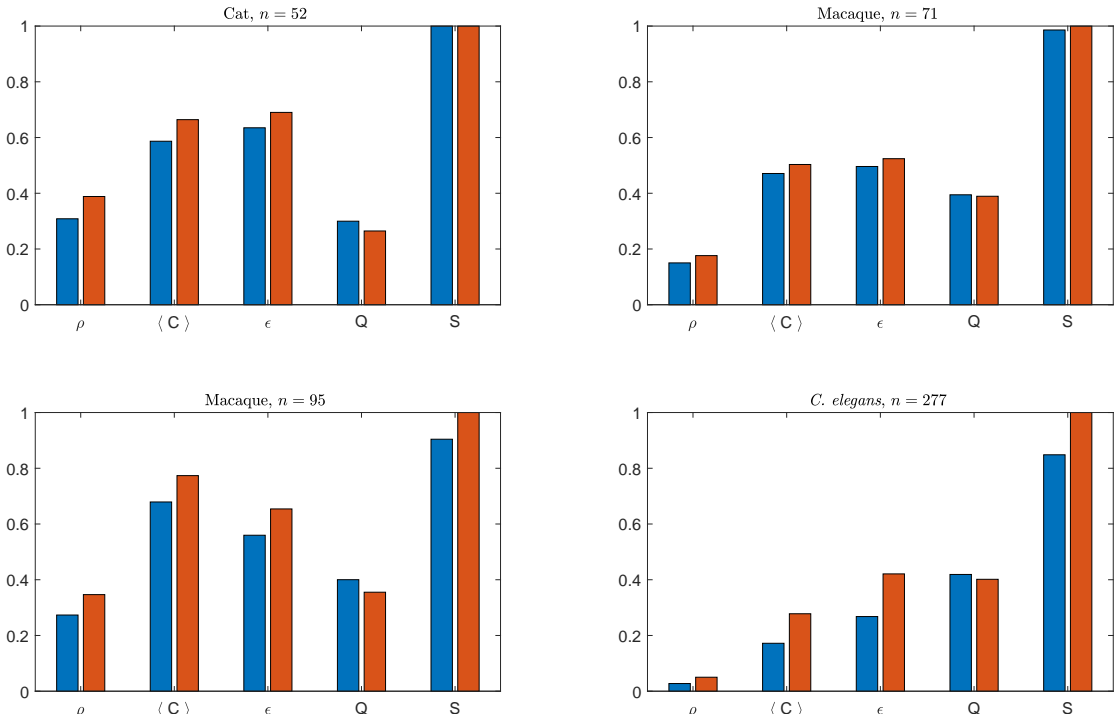


Figure 3.4: Network measures for both directed (blue) and undirected (red) connectomes: ρ = density; $\langle C \rangle$ = mean clustering coefficient; ϵ = efficiency; Q = Newman-Girvan modularity score; and S = size of the giant (strongly) connected component.

Our focus here is on the impact that directionality has on network dynamics; however, for completeness we present a brief overview of the fundamental statistical features of the connectomes introduced in the previous section for both directed and undirected cases. Note that unlike the study by Kale *et al.* [58], that considers a spectrum of perturbed networks comprised of the empirical (directed) connectome at one end and the fully undirected representation of the connectome at the other, we consider only the aforementioned limiting cases here.

Figure 3.4 shows results of a network analysis for the different connectomes using a range of standard network measures, including the network density ρ ; the global Watts-Strogatz clustering coefficient $\langle C \rangle$; and the Newman-Girvan modularity score Q (see Chapter 2 for definitions of these standard network metrics). In addition, since the empirical connectomes are in general not strongly connected, we also compute the relative size, S, of the giant strongly connected component (GSCC) for each connectome,

as well as the global efficiency, which recall is defined as

$$\epsilon = \frac{1}{n(n-1)} \sum_{i,j,i \neq j} \frac{1}{d(i,j)}.$$

Here $d(i,j)$ is the length of the shortest path between nodes i and j . All network measures were computed using the Brain Connectivity Toolbox [57].

The loss of directionality has the general effect of inflating network measures. For the local metrics considered (*i.e.* the degree and clustering coefficient) this is a direct consequence of the increased density of these networks. Note that whilst the clustering coefficient depends both on degree and interneighbour network connectivity, the addition of reciprocal edges results in a monotonic increase of $\langle C \rangle$. The inclusion of reciprocal edges has a similar inflationary effect on network efficiency since it facilitates shorter (potentially biologically implausible) routes between nodes. Interestingly, network modularity is higher in the empirical connectomes in all cases, which indicates the existence of asymmetric, intermodule connections potentially controlling the flow of neural information between functional modules. Table 3.1 shows the number of modules observed for each of the empirical and undirected connectomes corresponding to the modularity scores given in Figure 3.4. It is noteworthy that in the case of the Cat connectome and the *C. elegans* connectome, the removal of network directionality reduces the number of observed modules – see Appendix A for details. We remark that a similar break-down of modular topology due to the existence of false positive connections in undirected brain networks was recently observed in a study by Sporns and Betzel [111]. Finally, we note that, with the exception of the cat connectome, all empirical connectomes have GSCCs consisting of less than N nodes; the fraction of nodes in the GSCCs are 0.99, 0.90 and 0.85 for the Macaque connectome on 71 and 95 nodes and *C. elegans* connectome, respectively.

3.3.2 Numerical simulations

In all of our experiments the time constant and network gain were fixed at $\tau = 10$ and $G = 10000$ respectively. (Such a large value of the gain results in network saturation,

at least for the connectomes we analysed.) We then proceeded to investigate the behaviour of the system in (3.6) for different connectomes under variation of the control parameter P . Note that for such large values of G the function in (3.7) approaches a Heaviside function with switching threshold at $x_s = \theta/P$. As the switch approaches zero (*i.e.* in the large P limit) we have that all nodes are active for any non-zero initial condition (as long as the network is strongly connected), and so the system is monostable with almost all initial states converging to the maximal solution, also known as the ‘up’ state, $x_U^* = W^T \mathbf{1}$. Here $\mathbf{1} = \left(1, \dots, 1\right)^T$ is the vector of all ones. When the switch is at one (*i.e.* $P = \theta$), the network is in a quiescent ‘down’ state irrespective of the initial condition. That is, the system is monostable and all initial states converge to the trivial steady state $x_D^* = \mathbf{0}$. For intermediate values of P the system displays multistable behaviour.

In what follows, we choose $P \in [\theta, 10]$ since we have found (experimentally) that the dynamics of (3.6) are unchanged outside this region regardless of the connectome considered. More specifically, for each connectome, we selected 101 equally spaced values of $P \in [\theta, 10]$ and integrated a fixed set of 10^4 initial states drawn at random from the state space $Q = [0, 1]^n$. For each distinct fixed point x^* found, we then approximated its basin stability, $S_{\mathcal{B}(x^*)}(P)$, as the proportion of all initial states that converged to x^* . Fixed points were identified by integrating (3.6) for $T = 1000$ using the built-in MATLAB routine `ode45`, with absolute and relative tolerances both set to 10^{-6} . Note that convergence to a fixed point is generally much faster than $T = 1000$ and so the integration was terminated early in this case. To better sample the extremely high-dimensional state space, initial conditions were drawn from a binomial distribution with $x_i(0) \sim \text{Bi}(1, r)$, where r is a random number selected from a uniform distribution over $[0, 1]$. In this way, we consider a range of different initial activity patterns. For example, for small r the initial activity pattern has very few ‘active’ nodes. Conversely, large values of r result in initial activity patterns with large numbers of ‘active’ nodes.

Figure 3.5 shows an estimation of the number of final attractors for the four different connectomes as a function of the parameter P . For the three large-scale connectomes (figures 3.5(a–c)) we find that the number of attractors is relatively small, with a maxi-

Connectome	Cat		M71		M95		CE	
	D	U	D	U	D	U	D	U
Total # of attractors	205	198	204	203	286	223	605	1066

Table 3.2: Total number of attractors found for the original directed connectomes (D) and their undirected representations (U). Here, M71 and M95 denote the Macaque connectomes on 71 and 95 nodes, respectively, whilst CE denotes the *C. elegans* connectome.

mum of 4 to 11 different final attractors being observed for any particular P value. Peak pattern variability occurs for $P \approx 1$ for the three large-scale connectomes regardless of whether network directionality is incorporated. In terms of numbers, the empirical cat connectome displays nearly twice as many attractor states at peak variability than its undirected representation, whilst directionality appears to have less of an effect in the case of the two Macaque networks, although the empirical network on 95 nodes displays increased multistability over a broader range of P values. Results for the micro-scale connectome of *C. elegans* are shown in Figure 3.5(d). Unlike the macro-scale connectomes, we observe large numbers of attractor states for both directed and undirected connectomes, although significantly more in the undirected case, with approximately 10 times as many attractor states being observed at peak variability. Interestingly, peak variability for the empirical *C. elegans* connectome happens away from $P = 1$, in contrast to the other networks studied. As can be observed from Figure 3.5(d), the empirical network displays increased multistability over a broader range of P values than its undirected counterpart, peaking for values of P approximately in the plateau range (2, 4), although it is worth noting that a local maximum at $P \approx 1$ is also evident. (See the magnified section of Figure 3.5(d).) These findings are further supported by Table 3.2, which displays the cumulative number of attractor states (up to $P = 10$) for each of the four connectomes.

Figures 3.6 and 3.7 display the basin stability of the steady states of (3.6) as a function of the parameter P for the different connectomes considered in this work. For each value of P , the basin stabilities of each observed steady state are represented as a stacked bar

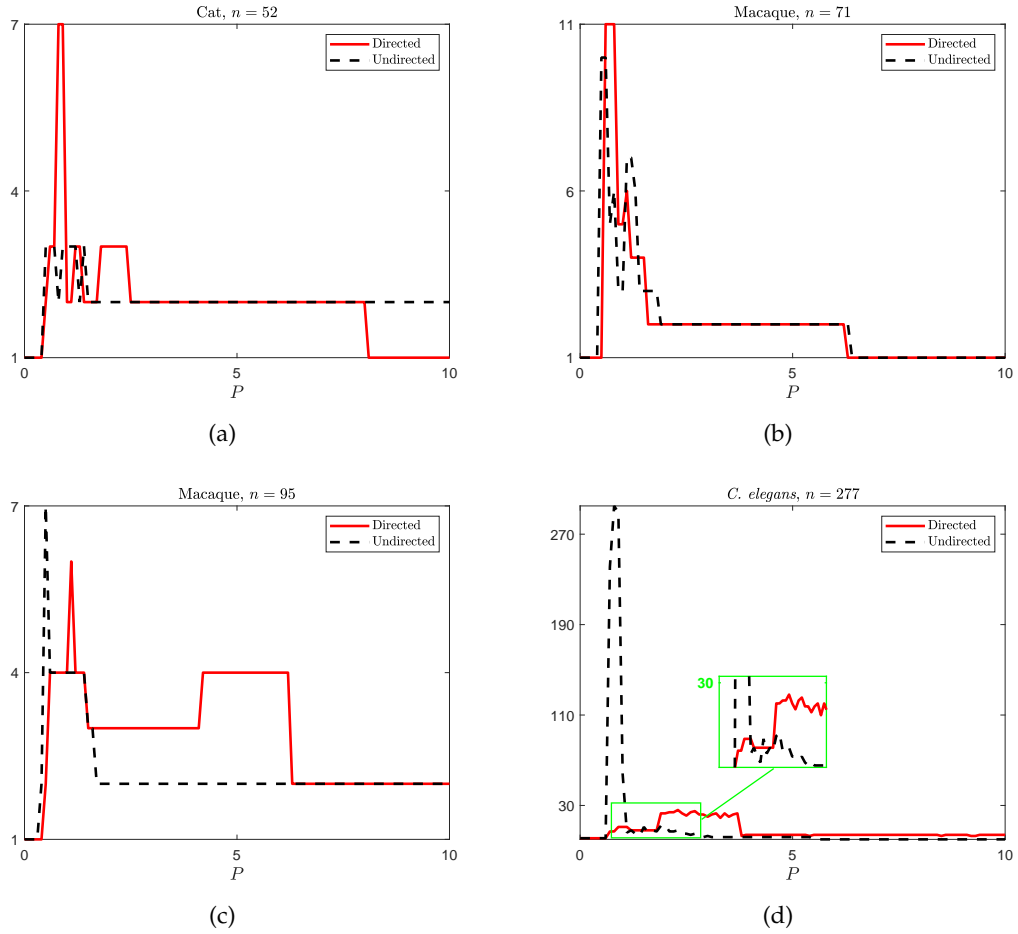


Figure 3.5: Estimated attractor numbers as a function of the scaling factor P for each of the connectomes described in Section (3.1.2).

chart with total height 1. Sub-bar heights are proportional to the basin stability, $S_{\mathcal{B}(x^*)}$, and are coloured according to the magnitude of x^* as measured by the one-norm. As expected, for low values of P the system is monostable with all initial states converging to the trivial steady state $x_D^* = \mathbf{0}$ regardless of the connectome. This is evident from the figures since the basin volume consists of a single blue bar. Increasing P sees the emergence of a multistable regime for all connectomes. For the undirected connectomes, regions of parameter space displaying high levels of multistability (*i.e.* more than two attractor states) were roughly contained within the interval $(0.5, 1.5)$, whilst for the empirical connectomes the multistable regime is significantly more widespread. As P is further increased the multistability systematically decreases until only two solutions remain: the trivial steady state, x_D^* , and the maximal solution, x_U^* , although the basin of attraction for the trivial steady state diminishes rapidly, as expected. We remark that

for networks that are only weakly connected, initial states exist that do not converge to the state x_{U}^* regardless of the size of P ; however, these solutions are rarely met in practice and so have negligible basins of attraction.

As expected the basin stability plots for the cat connectome differ significantly between the undirected and empirical connectomes. At peak variability the empirical connectome has seven different attractor states each with appreciable basins of attraction, whereas the undirected connectome is essentially bistable with almost all initial conditions converging either to the quiescent state, x_{D}^* , or to a highly active state (*i.e.* one such that $x^* \approx x_{\text{U}}^*$) regardless of the choice of P . A similar feature is observed for both the Macaque networks, in that solutions with intermediate activity tend to have relatively small basins of attraction in the undirected representations. Solutions for the empirical Macaque connectomes, however, exhibit various levels of neural activity as well as an increase in their respective domains of attraction.

The basin stability plots for *C. elegans* (Figure 3.7) are more complex than those of the mammalian connectomes due largely to the sheer number of solutions determined; however, we still observe broadly similar characteristics to the large-scale networks. Solutions for the undirected connectome are more ‘active’ on average, whilst multistability is prevalent across significantly larger regions of parameter space for the empirical network. Also, whilst the attractor set for the undirected *C. elegans* connectome consists of up to 295 activity patterns (for any particular P value), a considerable amount of redundancy exists, with many solutions being either very similar (in norm) or possessing negligible domains of attraction. Note that we have performed a clustering analysis (further details are provided in Appendix C) and determined a small number (3–10 in the multistable regime) of principal modes, or clusters in the attractor landscape, whose significance can be quantified using the combined basin stabilities of the clustered states. Importantly, such dimensionality reduction techniques enable us to characterise large, complex attractor sets, such as that obtained for the *C. elegans* connectome, using just a small number of prototypical activity patterns. Deploying the same technique for the empirical connectome results in 3–5 different prototypical network patterns for values of P in the multistable regime. Importantly, this result

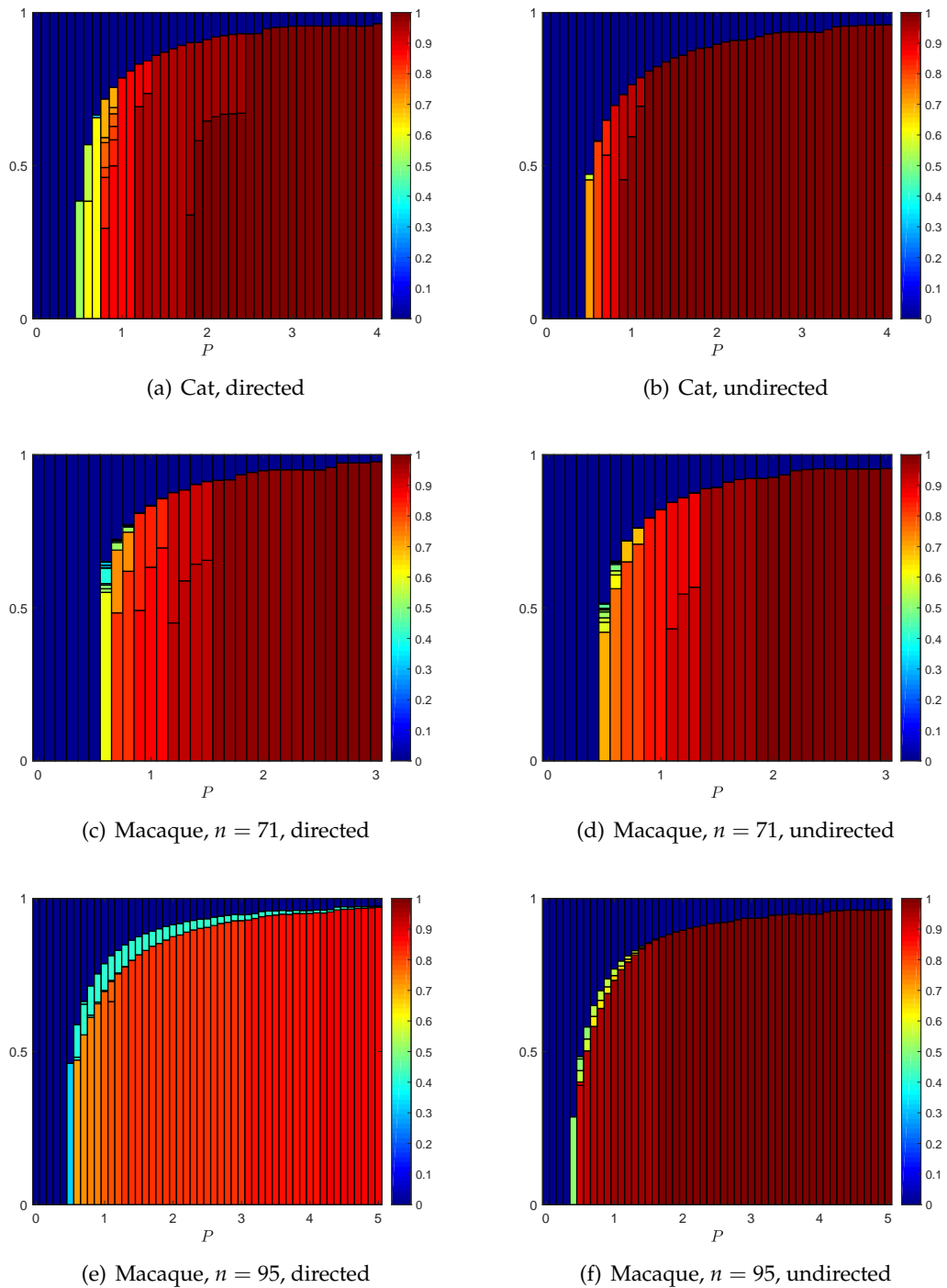


Figure 3.6: Basin stability of the Hopfield neuronal model as a function of the scaling factor, P , for the three large-scale mammalian connectomes considered in this work. (a, b), (c, d) and (e, f) display results for the directed and undirected connectomes of the respective parcellations of the cat and Macaque (on 71 and 95 nodes, respectively) cortex. Each solution is coloured according to its magnitude as measured by the one-norm.

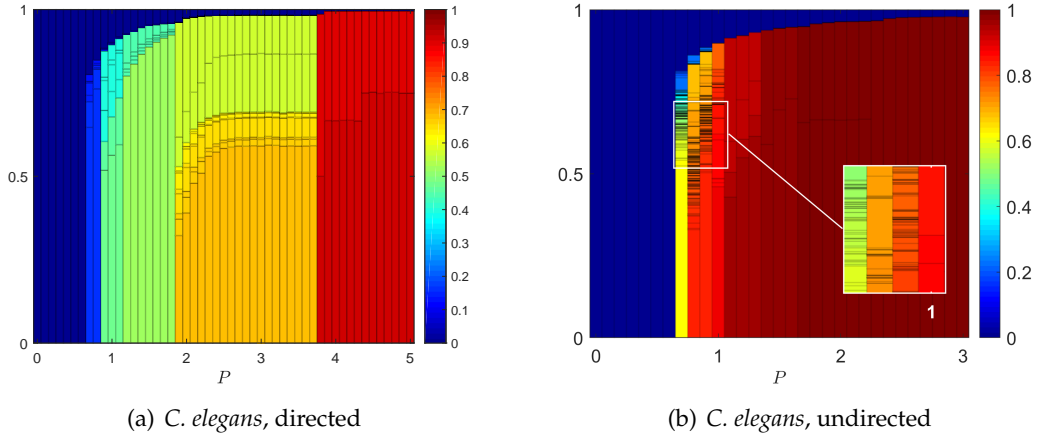


Figure 3.7: Basin stability of the Hopfield neuronal model as a function of the scaling factor, P , for the *C. elegans* neuronal network. (a) and (b) give results for the directed and undirected neuronal networks, respectively. Each solution is coloured according to its magnitude as measured by the one-norm.

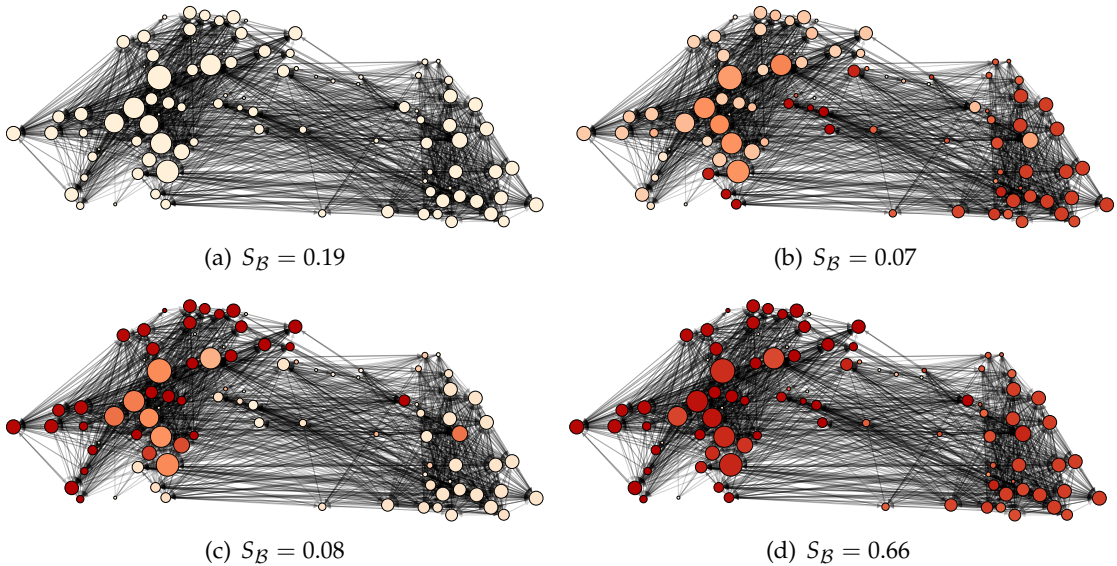


Figure 3.8: Example final activation patterns (*i.e.* network states) for the Macaque network on 95 nodes along with their respective basin stabilities. Here $P = 0.7$ and solutions shown are those with basin stability scores of at least 5%. As well as the ‘down’ state (a) and the ‘up’ state (d), we have two non-trivial intermediate states (b, c) whose activity is driven by the modular structure of the network.

suggests that despite the dramatic quantitative differences observed between the undirected and empirical connectomes (see Figure 3.5(d)), the number of sustainable patterns, whilst larger in the undirected connectome (approximately 5–10), remains small in both cases.

In Figure 3.8 we show an example of a typical set of final activation patterns for the empirical connectome of the Macaque monkey on 95 nodes along with their respec-

tive basin stabilities. We display only those solutions with a basin stability score of at least 5% since such network patterns are more likely to be sustainable as they are less sensitive to perturbations arising due to neuronal noise. Figures 3.8(a, d) display the quiescent state and a high activity state (which are permissible in both empirical and undirected connectomes (see Appendix B)), whilst figures 3.8(b, c) show two different intermediate states in which neuronal activity strongly reflects the modular organisation of the Macaque cortical network – a structure that is particularly evident in the spy plot in Figure 3.3. The two active modules observed in figures 3.8(b, c) are the same as those in [129] with the one in 3.8(b) consisting of brain regions belonging to visual pathways (*e.g.* primary visual cortices (V1, V2, V3 and V4), Frontal eye field (FEF), *etc*) serving perception and action [130], whilst the second module is formed of brain regions of importance to the control of movement (*e.g.* supplementary motor area (SMA) and premotor and visuomotor cortices (Brodmann areas 6 and 7)) as well as prefrontal areas responsible for decision making (*e.g.* orbitofrontal cortex (Brodmann areas 11 and 12)). We remark that whilst similar intermediate states (as those shown in figures 3.8(b, c)) exist for the undirected Macaque connectome, the frequency with which they are observed is greatly diminished due to the reduction in their respective basins of attraction. As a final note, we emphasise that the modular patterns displayed in Figure 3.8 are representative of configurations observed across all four connectomes studied here (see Appendix B for additional details), thus implicating directed network modularity as a key ingredient in the formation of neural patterns.

3.3.3 Discussion

In this Chapter, we have investigated the influence of directed network topology on the activation dynamics of connectome-based networks for a range of species, including the cat, Macaque monkey and *C. elegans* round worm. Whilst network directionality is typically ignored in network investigations of the brain (due largely to limitations in experimental neuroscience), our analysis indicates that it can have a profound effect on network dynamics, both in terms of the number of attractor states observed and the sustainability (or network robustness) of said states. We find that network patterns are

based on their studies (as well as recent results in [132]), significantly richer dynamics are expected in the case of directed networks, such as the emergence of travelling Turing waves, which importantly, are not observed in the undirected case. We note here, that the effect of directionality on the pattern formation capabilities of modular, connectome-based networks is an open area of research.

We remark that our results are in contrast to the study by Golos *et al.* [113] in which observed numbers of attractor states were orders of magnitude higher than found here, even for the case of the micro-scale *C. elegans* connectome; however, it is important to note that the connectomes studied in [113] are of the order $n = 1000$ and that the number of attractor states of (3.6) scale with network complexity (as seen in the case of *C. elegans*). Also, whilst the number of attractor states was much larger in the study by Golos *et al.*, a closer analysis determined a small set of ‘significant’ (and importantly comparably sized) activity patterns resembling observed resting state networks in the human brain. Other recent studies [133, 70] have reported attractor landscapes populated by a small number of patterns, as in this study, whilst results from empirical investigations typically posit the existence of up to eight different sustainable network patterns. (See, for example, the paper by Damoiseaux *et al.* [134].) The critical brain hypothesis [135] states that neuronal dynamics are governed by a dynamical system close to criticality. The resting state networks (*i.e.* attractor states) of this dynamical system are then multistable ghost attractors that shape the global dynamics of the system. Importantly, results in this study indicate that directed network topology can have a strong influence on both the number *and* configuration of admissible network patterns.

3.4 Summary

In this chapter we have shown that the directionality of networks can impact on the information capacity of connectomes and can also impact significantly the domains of attraction of the aforementioned brain states. Using a system of Hopfield neural elements with heterogeneous structural connectivity given by different species and parcellations (cat, *C. elegans* and two macaque networks), we investigated the effect of removing

directionality of connections on brain capacity, which we quantified via its ability to store attractor states. In addition to determining large numbers of fixed-point attractor sets, we deployed the recently developed basin stability technique in order to assess the global stability of such brain states, which can be considered a proxy for network state robustness. In particular, we found network modularity to be a key mechanism underlying the formation of neural activity patterns, and moreover, our results suggest that neglecting network directionality has the scope to eliminate states that correlate highly with the directed modular structure of the brain. A numerical analysis of the distribution of attractor states identified a small set of prototypical direction-dependent activity patterns that potentially constitute a ‘skeleton’ of the non-stationary dynamics typically observed in the brain. Therefore the ineffectiveness of modern neuroimaging techniques to try and correct directionality can potentially lead to errors in the classification of network patterns making it difficult to define a meaningful dynamical repertoire (*i.e.* collection of prototypical brain states) of the brain.

The impact of structural directionality on effective connectivity networks

In this chapter we investigate the implications of the directed topology of structural brain networks on the directed functional connectivity patterns observed in connectomes for several species (cat, two parcellations of the macaque monkey and *C. elegans*) [136, 137, 138]. To better understand these relations, we construct brain network models with neural dynamics of each brain region (network node) given by the Kuramoto model [139, 140] and structural connectivity defined via one of either the Macaque, Cat or *C. elegans* connectome. More specifically, we examine the impact of directionality on the speed of synchronisation, as well investigating the stability of these synchronous states as a function of the inherent time delay found within these neural systems. Moreover, we study the dependence of effective connectivity patterns on the directed topology underlying neural activity in the brain, by constructing and analysing functional connectivity networks using the so-called *directed phase lag index*, which is a measure of the flow of information within a network.

The Kuramoto model we study in this chapter is an example of a *phase oscillator model* [141], and so before proceeding we emphasise that in the following, we deploy the term synchronisation to describe the case when all signals coincide, *i.e.* all phases are identi-

cal. This is commonly known as *complete synchronisation* in the literature [142]. In addition, we are also interested in solutions in which the phase differences become constant and we term this behaviour as *phase locking*. Importantly, we are only interested in 1:1 locking (*i.e.* $|\theta_i - \theta_j| = \text{constant}$) here as opposed to the more general concept of $n : m$ locking, which requires the following relation between phases $|n\theta_i - m\theta_j| = \text{constant}$.

4.1 The Kuramoto model

The emergence of synchronisation in biology, and neuroscience in particular, is ubiquitous, as exemplified by chorusing crickets, flashing fireflies, or pulsing pacemaker neurons [143]. Winfree was the first to attempt to capture common features of the aforementioned oscillatory systems and beyond, with his pioneering work on weakly coupled systems of oscillators [144]. From a mathematical point-of-view, Winfree's formulation was essentially a mean field approach in which a large system of interacting units evolved according to the collective rhythm of the population.

Kuramoto [139], inspired by the work of Winfree, derived the following highly simplified model of n globally coupled oscillators:

$$\frac{d\theta_i}{dt} = \omega_i + \frac{S}{n} \sum_{j=1}^n \sin(\theta_i - \theta_j) \quad (i = 1, \dots, n). \quad (4.1)$$

Here, S is the coupling strength and θ_i and ω_i are respectively, the phase and natural frequency of the i^{th} oscillator. Note that despite its simplicities, the model in (4.1) displays many of the features of Winfree's earlier models, including the observed synchronisation threshold phenomenon.

The natural frequencies in (4.1) are typically drawn from a Lorentzian distribution centred at ω_0 and of width γ , that is the probability density function is given by

$$g(\omega) = \frac{\gamma}{\pi [\gamma^2 + (\omega - \omega_0)^2]}. \quad (4.2)$$

Figure 4.1 shows an example of the Lorentzian distribution for $\omega_0 = 10$ and $\gamma = 1$. Note, however, that other unimodal distributions such as the Gaussian distribution are

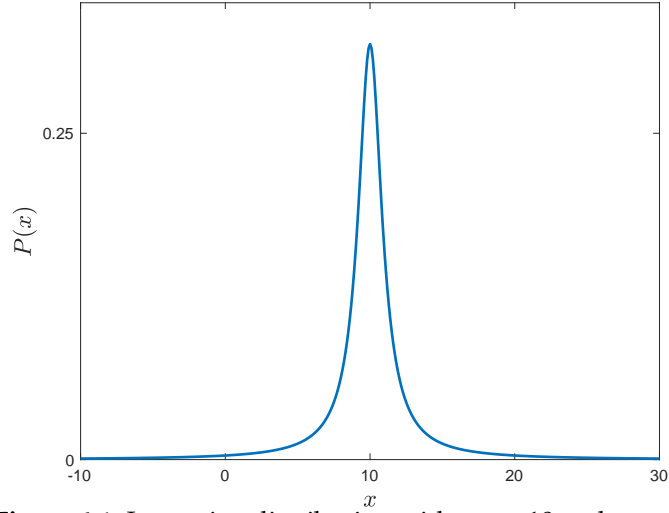


Figure 4.1: Lorentzian distribution with $\omega_0 = 10$ and $\gamma = 1$.

also used in practice.

To determine the levels of synchrony present within the system, Kuramoto forwarded the following *order parameter*:

$$r(t) = \left| \frac{1}{n} \sum_{i=1}^n e^{i\theta_i(t)} \right|. \quad (4.3)$$

If we denote by $r = \langle r(t) \rangle$ the time average of the order parameter, then it can be shown that when $r = 0$ the system is in an incoherent state with phases distributed evenly across the interval $[0, 2\pi)$, whilst for $r = 1$ all oscillators are perfectly phase-locked (*i.e.* display zero phase lagged synchrony). Importantly, Kuramoto showed that the system in (4.1) undergoes a phase transition, moving from a desynchronised state to a partially synchronised state as the coupling strength, S , is increased past some critical value $S = S_{\text{crit}}$ [139].

In Figure 4.2 we display the time-averaged order parameter, r , as a function of coupling strength S for a system of $n = 100$ Kuramoto oscillators. More precisely, we integrated (4.1) using the built-in Matlab solver ode45 with fixed step-size $\Delta t = 0.01$ for time $T = 100$. The mean frequency of the oscillators was 0 Hz, and the width of the Lorentzian distribution $\gamma = 1$. The system was initialised by drawing phases at random from a uniform distribution on $[0, 2\pi)$. To remove transients, the first 5,000 time-steps were discarded and the results were then averaged over 10 trials. For values of $S < 2$ we see

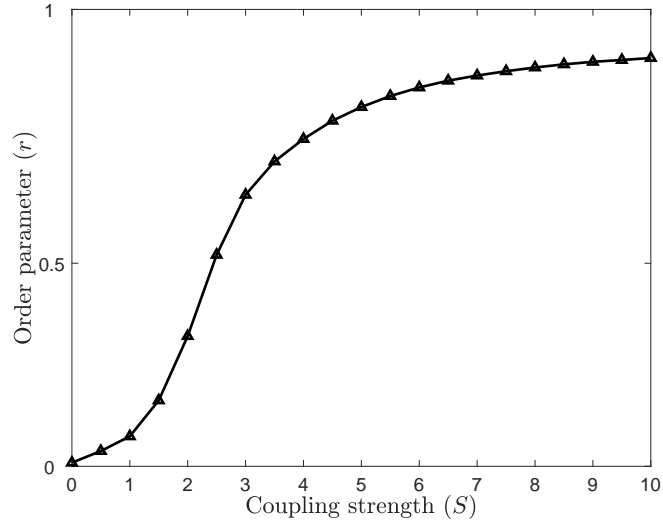


Figure 4.2: Time averaged order parameter r as a function of coupling strength S for a complete network on $n = 100$ nodes.

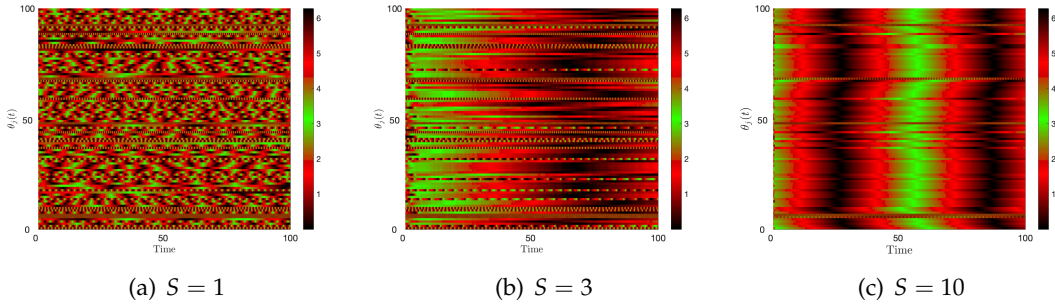


Figure 4.3: Evolution of oscillator phases for the globally coupled Kuramoto model ($n = 100$) for weak ($S = 1$), moderate ($S = 3$) and strong ($S = 10$) coupling.

that r remains at relatively low levels. From $S = 2$ onwards, however, there is a sudden increase in the averaged order parameter, which plateaus close to $r = 1$. Note that this result is in agreement with theoretical studies that have shown that if the natural frequencies are drawn from a Lorentzian distribution, then in the large n limit S_{crit} is given by

$$S_{\text{crit}} = 2\gamma. \tag{4.4}$$

Thus the phase transition in this case, is completely determined by the width, γ , of the Lorentzian distribution.

Figure 4.3 illustrates the impact of increasing the coupling strength, S , on the evolution of phase oscillators. As can clearly be seen, in the case of weak coupling the oscillators disperse, whereas for increasing values of S , clusters of synchronous oscillators begin to appear, which merge to form a fully synchronised solution for large S .

4.1.1 Extensions of the model to a neuroscience setting

The Kuramoto model described in the previous section can be generalised in a number of ways to make it more applicable to a neuroscience setting. For example, neural networks display a heterogeneous network connectivity and so the all-to-all connectivity of the original problem is more naturally replaced by one that resembles the topology of the brain. In addition, one typically wants to account for the inherent delays within neural systems that arise due to finite neural signalling speeds. Accounting for such physiological details results in the following Kuramoto model for complex networks [145]:

$$\frac{d\theta_i}{dt} = \omega_i + S \sum_{j=1}^n a_{ji} \sin(\theta_j - \theta_i - \beta), \quad i = 1, \dots, n. \quad (4.5)$$

Here, a_{ij} denotes the elements of the cortical connectivity matrix, β is a phase delay term that accounts for finite signal propagation speeds [146], and S is the coupling parameter as before. Note that in the above equation the factor of $1/n$ has been removed so that the coupling is independent of the system size n ; it has been argued that this allows for more meaningful comparisons between observables between networks of differing size.

Note that in [94], it was shown (in the case of an undirected network) that the networked system (4.5) can be simplified via the introduction of the following local order parameter

$$r_i e^{j\Theta_i} = \frac{1}{n_i} \sum_{k=1}^N a_{ik} e^{j\theta_k}. \quad (4.6)$$

where n_i is the sum of the couplings to oscillator i , $n_j = \sum_{k=1}^N a_{ik}$. The above equation differs from that in [145] as it accounts for the fact that the network is potentially directed. The local order parameter (LOP) measures to what extent oscillator i is in synchrony with its neighbours.

Multiplying (4.6) by the factor $e^{-i(\Theta_i + \beta)}$ and equating imaginary parts of the resultant expression gives

$$r_i \sin(\Theta_i - \theta_i - \beta) = \frac{1}{k_i^{\text{in}}} \sum_{j=1}^n a_{ji} \sin(\theta_j - \theta_i - \beta), \quad (4.7)$$

which results in the following form of Equation (4.5):

$$\frac{d\theta_i}{dt} = \omega_i + Sk_i^{\text{in}} r_i \sin(\Theta_i - \theta_i - \beta), \quad i = 1, \dots, n. \quad (4.8)$$

We can further simplify these equations by deploying a rotating coordinate frame, that is by performing the following change of variables $\phi_i = \theta_i - \Omega t$, where Ω is the population frequency once a stationary distribution has been reached. This leads to the following representation of a network of Kuramoto oscillators:

$$\frac{d\phi_i}{dt} = \omega_i - \Omega + Sk_i^{\text{in}} r_i \sin(\Phi_i - \phi_i - \beta) \quad i = 1, \dots, n. \quad (4.9)$$

Here, $\Phi_i = \Theta_i - \Omega t$.

It follows that phase locked solutions of (4.5) are fixed points of (4.9), asymptotically at least. The advantage of the above formulation is that it reveals the important relation between the in-degree of the network and the ability for oscillators to phase lock. To see this, note that since we require $d\phi_i/dt = 0$ for the oscillators to phase lock, we have the following fixed point condition

$$F_i(\phi_i) = \omega_i - \Omega + Sk_i^{\text{in}} r_i \sin(\Phi_i - \phi_i - \beta) = 0, \quad i = 1, \dots, n, \quad (4.10)$$

where $F(\phi)$ is the right-hand side of Equation (4.9). Note that the r_i and Φ_i are constant in the phased lock state. The Jacobian of (4.9) is given by

$$\frac{\partial F_i}{\partial \phi_j}(\phi^*) = \begin{cases} -Sk_i^{\text{in}} r_i \cos(\Phi_i - \phi_i^* - \beta), & i = j, \\ 0, & i \neq j. \end{cases} \quad (4.11)$$

For a fixed point to exist requires the condition $|\omega_i - \Omega| \leq Sk_i^{\text{in}} r_i$, to hold, and moreover, for that fixed point to be stable requires

$$\cos(\Phi_i - \phi_i - \beta) > 0, \quad i = 1, \dots, n. \quad (4.12)$$

When the aforementioned stability condition is satisfied, we can solve (4.10) to obtain

the following analytical expression for the phase:

$$\phi_i^* = \sin^{-1} \left(\frac{\omega_i - \Omega}{S k_i^{\text{in}} r_i} \right) + \Phi_i - \beta, \quad i = 1, \dots, n. \quad (4.13)$$

This result is a direct extension of that in [94] to directed networks, in that it provides a relation between the phase of an oscillator and the in-degree, k_i^{in} , and the local order parameter (via r_i and Φ_i). In [94], the authors argued that since the inverse sine function is monotonically increasing and the r_i and Φ_i display only a small amount of variation (an experimentally observed fact), the phase ϕ_i increases as the network degree decreases, that is they discovered an inverse relationship between node phase and node degree. We shall consider the question of whether or not such a relation persists when directionality is incorporated later on in this chapter.

4.2 Directed functional connectivity

Directed functional connectivity (*i.e.* effective connectivity (EC)) is a measure of the influence that a node exerts over other nodes in the network [147]. Unlike standard functional connectivity (such as that derived using Pearson's correlation coefficient or mean phase coherence) these interactions are not necessarily reciprocal resulting in asymmetric adjacency matrices describing function. A number of techniques are available for measuring EC, for example, Granger causality [97], structural equation modelling [148], and dynamic causal modelling [149], to name a few. Here, we deploy the concept of directed phase lag index (dPLI) [95] to determine EC. Our primary motivation for using dPLI, is to be able to perform a comparative analysis with the work in [94, 96, 150], which deployed it to determine important structure-function relations in the case of undirected connectomes. In particular, we wish to investigate the extent to which directed connectomes impact observed global directionality patterns in the brain.

4.2.1 Phase lag index

The phase lag index (PLI) is a measure of phase synchronisation that was originally introduced to counter biases that typically reduce the reliability of phase synchronisation estimates in EEG signals [151]. It measures the asymmetry of a phase distribution and can be obtained from the time series of phase differences as follows

$$PLI_{ij} = |\langle \text{sign} [\Delta\theta_{ij}(t_k)] \rangle|. \quad (4.14)$$

Here, $\Delta\theta_{ij}(t) = \theta_i - \theta_j$ denotes the instantaneous phase difference between node pairs; the sign function yields 1 if $\Delta\theta_{ij} > 0$, 0 if $\Delta\theta_{ij} = 0$ and -1 if $\Delta\theta_{ij} < 0$; and the angled brackets denote a time average. PLI lies in the range $[0, 1]$, with zero indicating no coupling, or rather, that signals are randomly alternating between a position of phase lead and lag. A PLI score of 1 indicates that the instantaneous phase of one signal is consistently leading that of the other (*i.e.* they are phase locked).

It is worth noting that the formula in (4.14) assumes that phases lie in the range $[-\pi, \pi)$, if, however, phases lie in the interval $[0, 2\pi)$ then the formula

$$PLI_{ij} = |\langle \text{sign} [\sin (\Delta\theta_{ij}(t_k))] \rangle|$$

should be deployed.

As mentioned above, the authors of [96] considered directed PLI in order to determine the impact that network topology has on effective connectivity. The measure is obtained from the PLI measure in (4.14) by simply removing the absolute value:

$$dPLI_{ij} = \langle \text{sign} [\Delta\theta_{ij}(t_k)] \rangle. \quad (4.15)$$

The range of dPLI is $[-1, 1]$. If a node leads on average then it obtains a dPLI score in $(0, 1]$; if it lags on average a score in $[-1, 0)$; and a score of zero in the absence of a phase-lead/lag relationship. Importantly, it was shown in [96] that network degree was an effective predictor of phase-lead/lag relationships in the case of undirected network topologies; and so in this chapter we wish to explore the extent to which this

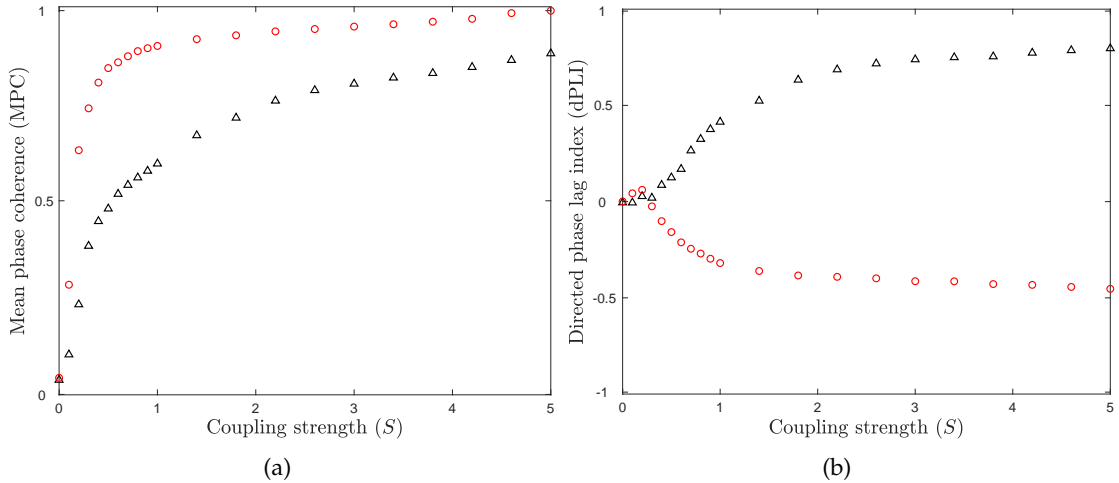


Figure 4.4: Distinct local dynamics of hub and peripheral nodes as coupling strength (S) increases. Hub nodes shown by the red circles and the peripheral nodes shown with black triangles. Results shown for the undirected cat connectome.

result holds for directed, or empirical, connectomes.

In Figure 4.4 we repeat experiments in [96] in which the authors demonstrate the impact of undirected network topology on local oscillator phase dynamics. To illustrate the result we use the undirected connectivity structure of the cat cortex, but the result applies to all undirected cortical networks studied in our work. We solved the system in (4.5) with A set equal to the undirected adjacency matrix of the cat cortex ($n = 52$) for $T = 100$ using the built-in Matlab solver `ode45` ($\Delta t = 0.01$) and phase delay $\beta = 0.1$. Note that this matches the set-up in [96]. Figure 4.4(a) shows the mean phase coherence (MPC) (see [55] for a precise definition) for two nodes in the network: the node of maximal degree (red circle); and the node with minimal degree (black triangle). Note that MPC is a measure of phase synchrony that is similar in spirit to the Kuramoto order parameter in that it is a temporal average over an angular distribution of the phase differences between node pairs and that we use it in this instance to more accurately replicate the results in [96]. We see that the high-degree node synchronises significantly quicker than the low-degree node and attains full synchrony (*i.e.* an r value close to one) for smaller values of coupling. In Figure 4.4(b) we display the mean dPLI values for the nodes with maximal (red circle) and minimal (black triangle) degree. This is

Connectome	Cat		M71		M95		CE	
	D	U	D	U	D	U	D	U
# of nodes	52	52	70	70	85	85	235	235
# of edges	818	515	745	437	2356	1481	1841	1656
mean degree	15.73	19.81	10.64	12.49	27.72	34.85	7.83	14.09

Table 4.1: Network statistics for the directed connectomes (D) and their undirected representations (U) restricted to its strongly connected component. Here, M71 and M95 denote the original Macaque connectomes of 71 and 95 nodes, respectively, whilst CE denotes the *C. elegans* connectome.

computed by averaging over all dPLI values, *i.e.*

$$dPIL_i = \frac{1}{n} \sum_{k=1}^n dPIL_{ik}. \quad (4.16)$$

For large values of S we observe a distinct behaviour between high- and low-degree nodes, with the low-degree node leading and the high-degree node lagging, for sufficiently large S .

4.3 Numerical Experiments

In all of our experiments Equation (4.5) was integrated from $t = 0$ to $t = 100$ using the built-in Matlab solver ode45 with $\Delta t = 0.01$ and absolute and relative tolerances set at 10^{-8} . In accordance with [96], natural frequencies of the oscillators were drawn from a Gaussian distribution with mean $f = 10\text{Hz}$ (or $\omega_j = f \cdot 2\pi \text{ rad/s}$) and variance one. This choice of frequencies simulates observed alpha oscillations in the human brain as well as the peak bandwidth of other species such as the macaque and mouse [96, 94]. To determine the dependence on initial data, each simulation was repeated ten times with different sets of initial conditions θ drawn uniformly at random from the interval $[0, 2\pi)$. Connectomes studied are the same as those in Chapter 3; however, to ensure the existence of the completely synchronised solution (in the case $\beta = 0$ at least) we restricted each connectome to its strongly connected component, thus resulting in the following networks: cat of size $n = 52$; parcellations of the Macaque on 71 and 95 nodes become of size $n = 70$ and $n = 85$, respectively; and *C. elegans* of size $n = 235$, basic network statistics are given in Table 4.1.

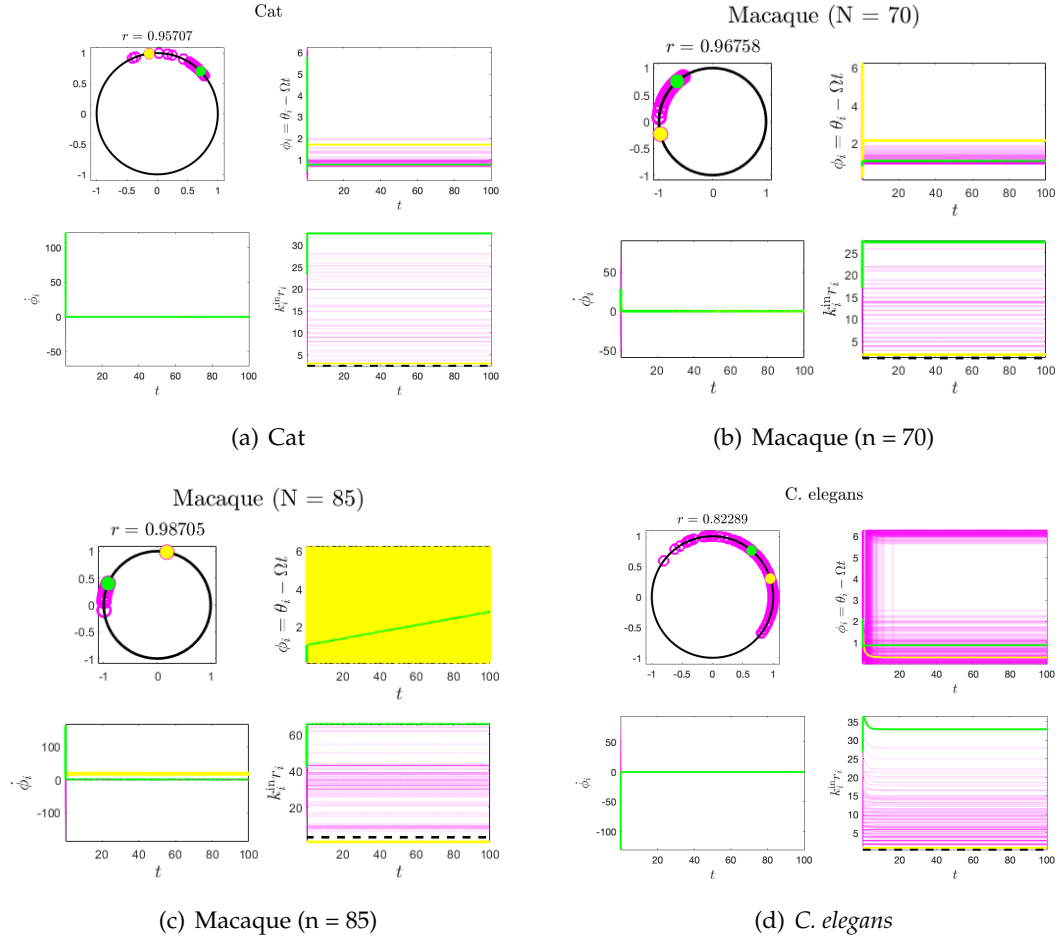


Figure 4.5: Simulation results: $S = 1, \beta = 0.1$

Figure 4.5 shows simulation results when solving Equation (4.5) for each of the four connectomes. In these experiments we deploy the directed, or empirical, connectomes with $S = 1$ and $\beta = 0.1$. For each connectome we plot four figures: a snapshot of the Kuramoto model in action with phases at time $T = 100$ plotted on the unit circle (Top Left); the relative phase ϕ versus time (Top Right); the rate of change in the relative phase (Bottom Left); and the quantity $k_i^{\text{in}} r_i$ (Bottom Right). In addition, in each plot we highlight in yellow the node of greatest degree and in green the node with minimal degree. With the exception of the Macaque parcellation with $n = 85$, we observe convergence towards a phase locked state for the selected parameter values. This is evident not only from the plots displaying constant values for both the quantity $k_i^{\text{in}} r_i$ (recall that r_i tends to a constant value when the system is phase locked) and the rel-

ative phase, but also from the fact that $\dot{\phi}_i$ tends to zero for all i . The latter statement follows from the fixed point condition in Equation (4.10). Additionally, as noted above, in the case of the Macaque connectome on $n = 85$ nodes we do not observe convergence to a phase locked state, rather the nodes are divided into two classes: those that phase lock and those that drift monotonically without locking.

4.3.1 Speed of Synchronisation

For $\beta = 0$ the system in (4.5) admits a fully synchronised solution of the form

$$\theta_i(t) \equiv \theta_j(t) =: \theta(t). \quad (4.17)$$

For non-zero values of β the solution in (4.17) is no longer guaranteed, rather in this case we observe either phase locked solutions such that $\theta_i - \theta_j$ is constant $\forall i, j$ or so-called cluster states in which two or more groups of synchronised oscillators coexist.

In this section we assume identical oscillators so that $\omega_i = \omega \forall i$, and set the phase lag $\beta = 0$ thus guaranteeing the existence of the completely synchronised solution in (4.17). To determine the time scales of synchronisation for the different connectomes we compute the distance

$$d(t) = \max_{i,j} \text{dist}(\theta_i, \theta_j), \quad (4.18)$$

where

$$\text{dist}(\theta, \theta') = \min \{|\theta - \theta'|, 2\pi - |\theta - \theta'|\} \quad (4.19)$$

is the circular distance between two phases θ and θ' on S^1 . Note that after some initial transient, convergence to the synchronous state decays as $d(t) \sim \exp(-t/\tau)$, where τ denotes the characteristic time scale of each cortical network. Theoretically, this characteristic time scale is given by

$$\tau = -\frac{1}{\text{Re}(\lambda_2)}, \quad (4.20)$$

where λ_2 is the second largest eigenvalue of the graph Laplacian [152], which in this case coincides with the stability matrix, or Jacobian, of (4.5) evaluated at the synchronous state. (See, for example, [153] for further details.)

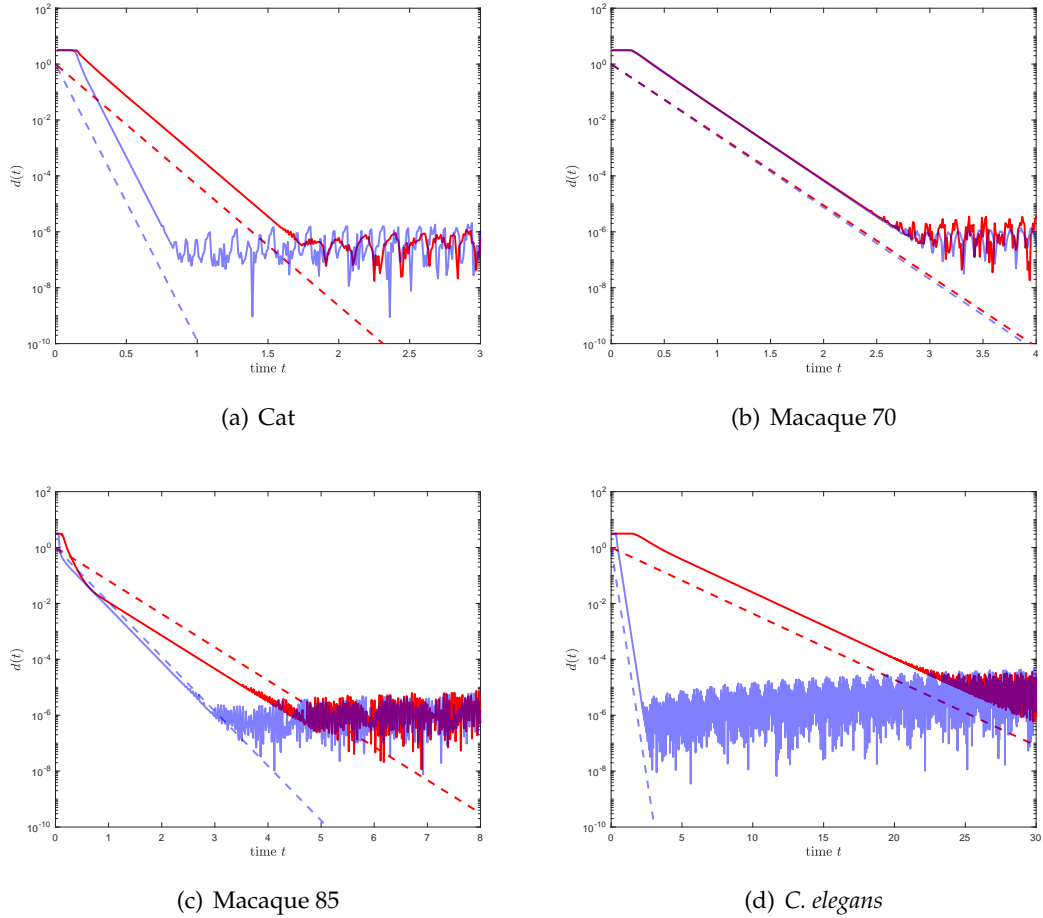


Figure 4.6: Speed of synchronisation shown by plotting $d(t)$ against time. Blue lines represent the undirected network and red lines show the directed network. For $\beta = 0$ and coupling strength, $S = 1$.

In Figure 4.6 we plot the logarithm of the decaying distances for directed (red line) and undirected (blue line) representations of each of the connectomes. In addition, we plot slopes of $-1/\tau$ for both directed (red dashed line) and undirected (blue dashed line) networks, where τ is the theoretical time-scale given in (4.20). Importantly, we find that in all cases synchronisation times are reduced for the undirected connectomes, and also, that, with the exception of the Macaque network on $n = 70$ nodes (which displays very similar time-scales regardless of directionality), these differences scale with the size of the network. Moreover, we note that the theoretical time-scales predicted by (4.20) are in excellent agreement with the simulation results.

Finally, we plot the normalised spread of the Laplacian eigenvalues for each network, in both directed and undirected cases, since this is known to correlate with network

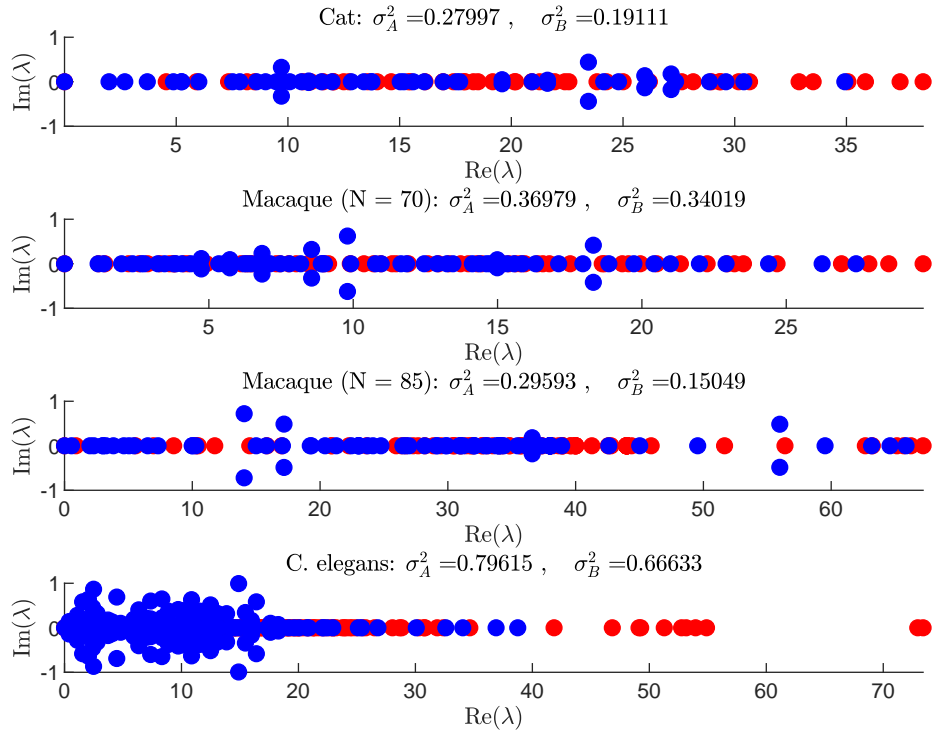


Figure 4.7: Scatter plots of the eigenvalues for empirical (blue) and undirected (red) representations of the connectomes studied in our work.

synchronisability [154]. To quantify the spread of the eigenvalues we use the following (see [155] for further details):

$$\sigma^2 = \frac{1}{d^2(n-1)} \sum_{i=2}^n |\lambda_i - \langle \lambda \rangle|^2, \quad \text{where} \quad \langle \lambda \rangle = \frac{1}{n-1} \sum_{i=2}^n \lambda_i. \quad (4.21)$$

Note that in the above equation, the quantity $d = \frac{1}{n} \sum_{i \neq j} a_{ij}$ measures the average coupling strength per node. Importantly, the smaller the variance (as measured by Equation (4.21)) the more synchronisable the network will generally be.

Figure 4.7 shows the spread of the eigenvalues of the graph Laplacian for each of the four networks considered, in both the directed (or empirical) and undirected cases, as well as σ_A^2 and σ_B^2 , which measure, respectively, the eigenvalue spread in the empirical and undirected networks. Note that in all cases, we find that the spread is reduced for the undirected connectomes, suggesting that these networks synchronise easier, a result that is in agreement with our earlier numerical experiments.

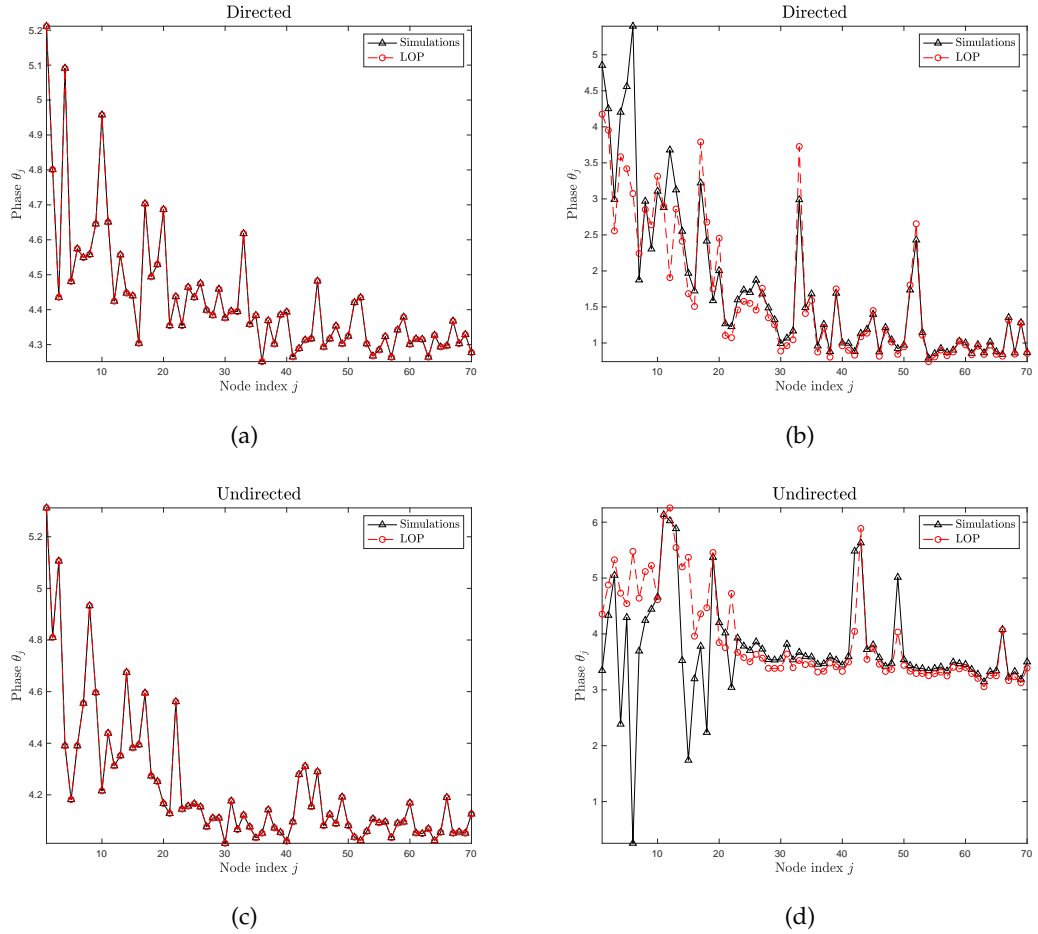


Figure 4.8: Comparison between the analytical and simulation results for macaque ($n = 70$). Top row are results for the directed networks and bottom for that of the undirected networks with $\beta = 0.1$ on the left and $\beta = 0.5$ on the right.

4.3.2 Stability of phase locked solutions

For non-zero β the solution in (4.17) is no longer guaranteed to exist; rather, as we increase β the system in (4.5) admits phase locked solutions such that $\theta_i - \theta_j$ equals a constant $\forall i, j$. See Figure 4.5 for examples of such solutions. Recall that these phase-locked solutions can be determined analytically, when they exist, by solving Equation (4.10) for ϕ to obtain the following

$$\phi_i^* = \sin^{-1} \left(\frac{\omega - \Omega}{S k_i^{\text{in}} r_i} \right) + \Phi_i^* - \beta, \quad i = 1, \dots, n. \quad (4.22)$$

Importantly, phase-locked solutions are fixed points in the rotating frame.

Figure 4.8 compares results of numerical simulations and the analytical phase given

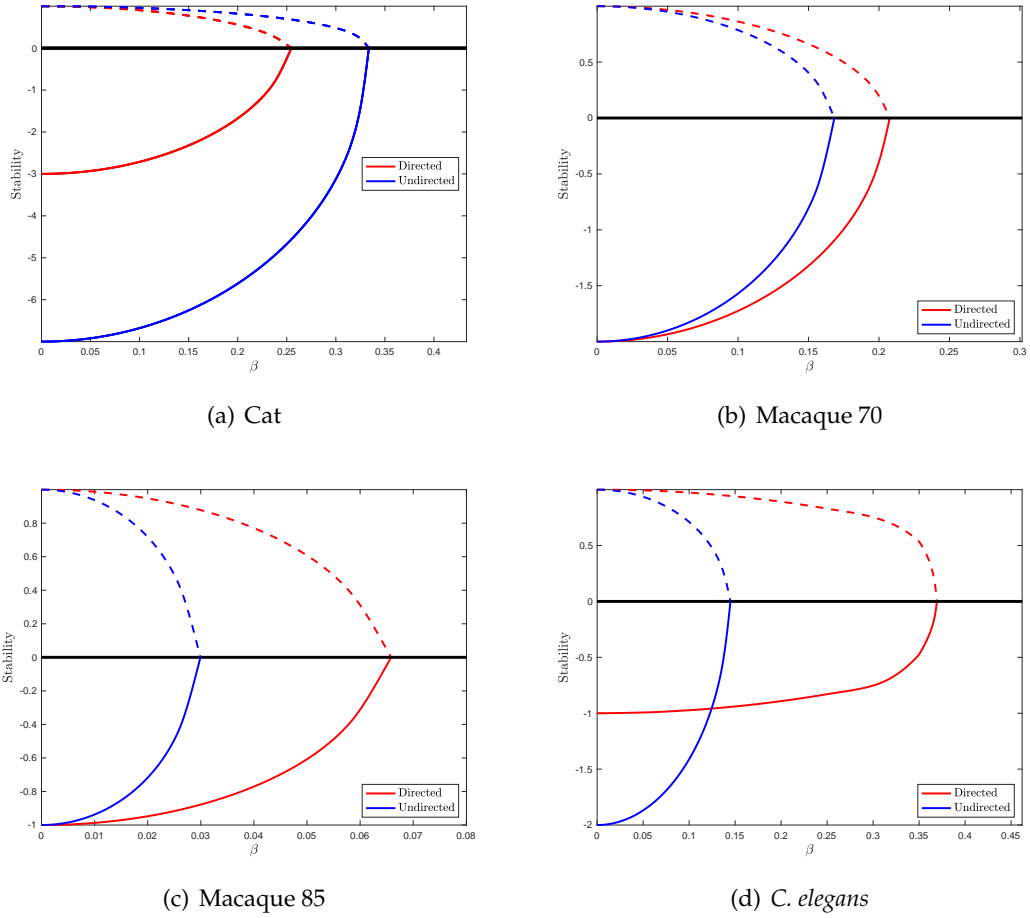


Figure 4.9: Stability plots of the 4 networks considered. Red lines are for the directed networks and blue for the undirected networks. Solid lines show the value of the maximal eigenvalue and dashed lines the stability condition in (4.12) as a function of the delay parameter β .

in (4.22) for two different values of the delay parameter ($\beta = 0.1$ and $\beta = 0.5$) using the macaque connectome on $n = 70$ nodes. Figures on top display results for the empirical connectome and those below for the undirected connectome. We see that for the smaller delay ($\beta = 0.1$) the analytical result is in agreement with the simulations; however, as we increase the delay the two results diverge due to a loss in stability of the phase locked solution, which results in so-called *cluster states* in which two or more groups of synchronised oscillators coexist. Similar results hold for all networks.

Next we wish to determine the value of β at which the phase locked solution loses stability for each of the connectomes. To do this, we calculate the maximal eigenvalue, λ_{\max} , of the Jacobian matrix in (4.11) evaluated at the fixed point (which we evaluate via direct numerical integration) for increasing values of β , stopping as λ_{\max} approaches

zero.

Figure 4.9 plots the maximal eigenvalue (solid line) and the stability condition in (4.12) (dashed line) for empirical (red) and undirected (blue) connectomes for each of the four species considered. Importantly, we observe an increase in the stability properties of the phase locked solution for the empirical connectomes in all but the cat network. We note that this anomaly can be understood by considering Equation (4.11), from which we observe that for $\beta = 0$, the stability of the globally synchronised solution is given by the minimal in-degree (or degree in the case of the undirected representation) of the network. Unlike the other networks considered here, the cat network's minimal degree increases significantly (going from 3 to 7) in the undirected connectome, as can be readily observed in Figure 4.9(a). Importantly, the impact of these additional false negative connections is to artificially increase the stability of the phase locked solution. It is noteworthy that despite the initial differences in stability between the empirical and undirected cat networks, the rate at which stability decays is greater in the undirected connectome, a fact that is consistent across all species we considered.

These results suggest that directed connectomes are more robust with respect to delays, which, according to a number of recent studies (see [156] and references therein), is likely to improve both the efficacy of signal transmission and the quality of information transfer in brain networks.

4.3.3 Phase lead/lag relations

As mentioned previously, the relationship between phase (as measured by dPLI) and cortical network structure has recently received considerable attention (see for example [94, 96, 157]). In particular, it was shown that patterns of phase lead and lag can be predicted by the network structure, network degree to be more specific. In this section we wish to determine whether or not a similar result holds for directed connectomes.

dPLI Vs network degree

To begin with we focus on network degree. Our results are plotted in Figure 4.10. For each network, simulations were performed for $S \in [0, 5]$ and for two different values of β ; one in which the phase locked state was stable and one in which it was not. In [94, 96], it was shown that nodes with large degree phase lag, whilst nodes with small degree phase lead, and so in the figures we plot the mean dPLI (see Equation (4.16)) of each node as a function of the coupling strength S , with nodes ordered in ascending order of their in-degree. It is clear from Figure 4.10 that this relation holds for all undirected connectomes as expected; however, we find the relation between phase lead/lag and node degree to be less transparent in the case of the directed networks. In particular, the relationship appears to largely breakdown for the two larger networks of Macaque ($n = 85$) and *C. elegans*.

To understand why this is the case we need to reconsider the equation for the analytic phase, *i.e.*

$$\phi_i^* = \sin^{-1} \left(\frac{\omega - \Omega}{S k_i^{\text{in}} r_i} \right) + \Phi_i^* - \beta, \quad i = 1, \dots, n. \quad (4.23)$$

As noted in [94], neglecting the potential impact of the terms r_i and Φ_i that result from the local order parameter (4.6), provides an inverse relationship between phase and node degree. Our results would appear to suggest that these terms are indeed negligible in the undirected case, with simulations (not shown) showing that $r_i \approx 1$ for all i , whilst the Φ_i are approximately constant. However, for the empirical connectomes (particularly the larger ones), we observe considerable variation in the Φ_i terms, which we hypothesise arise due to the existence of non-reciprocal connections present within the empirical networks that cause a breakdown in the local synchrony properties of the affected nodes, which explains the increased variability and thus the breakdown in the relation between phase and network degree. We note that there is much less variation in the r_i terms. These results are similar to those obtained in [158], in which it was shown that the over representation of certain closed loop motifs could frustrate, or disrupt, synchronous dynamics in directed cortical networks at both the local and global level.

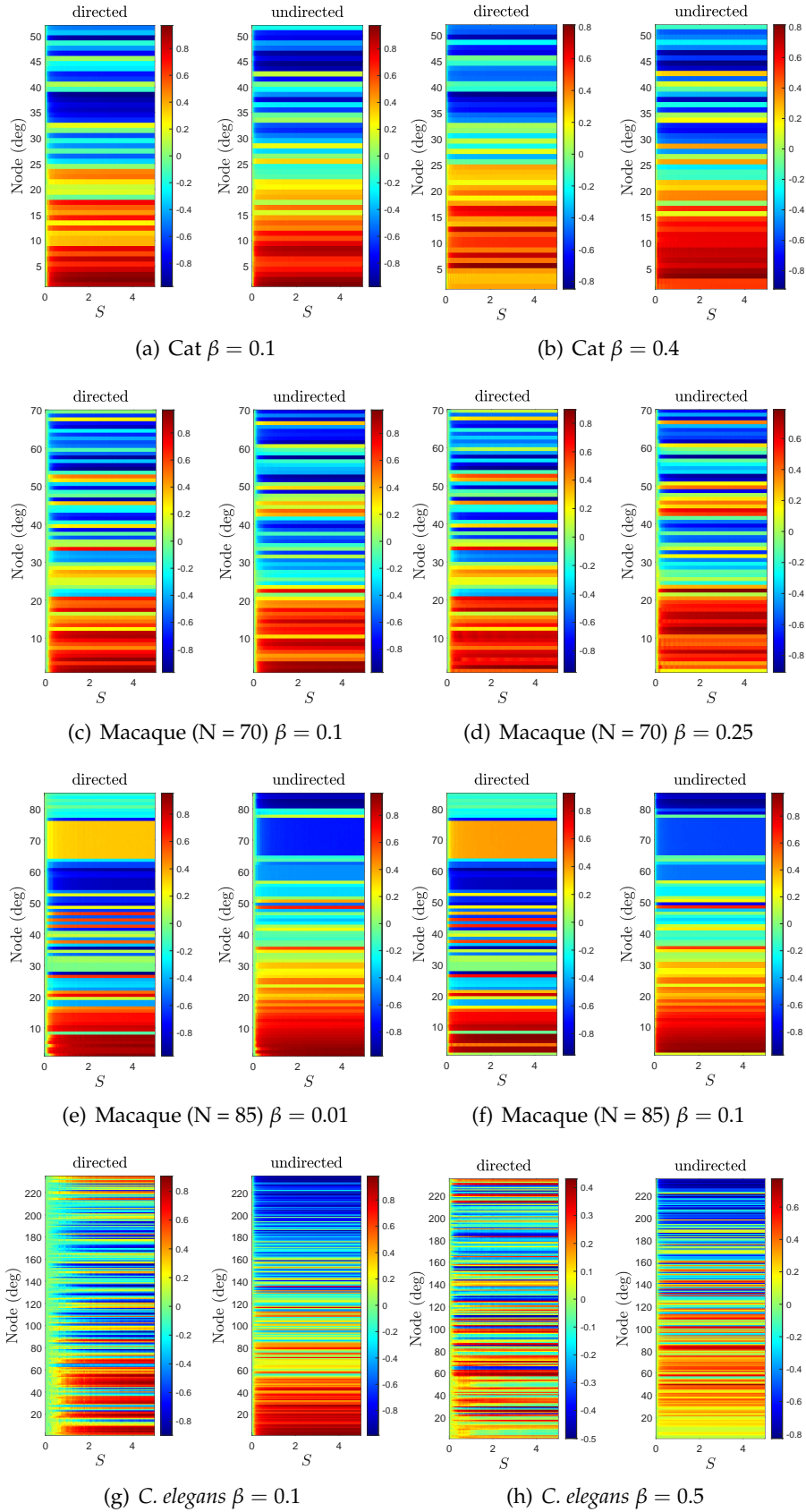


Figure 4.10: dPLI vs S . Left side of figure is for a chosen value of β in which the system is stable and right side is when the system is unstable.

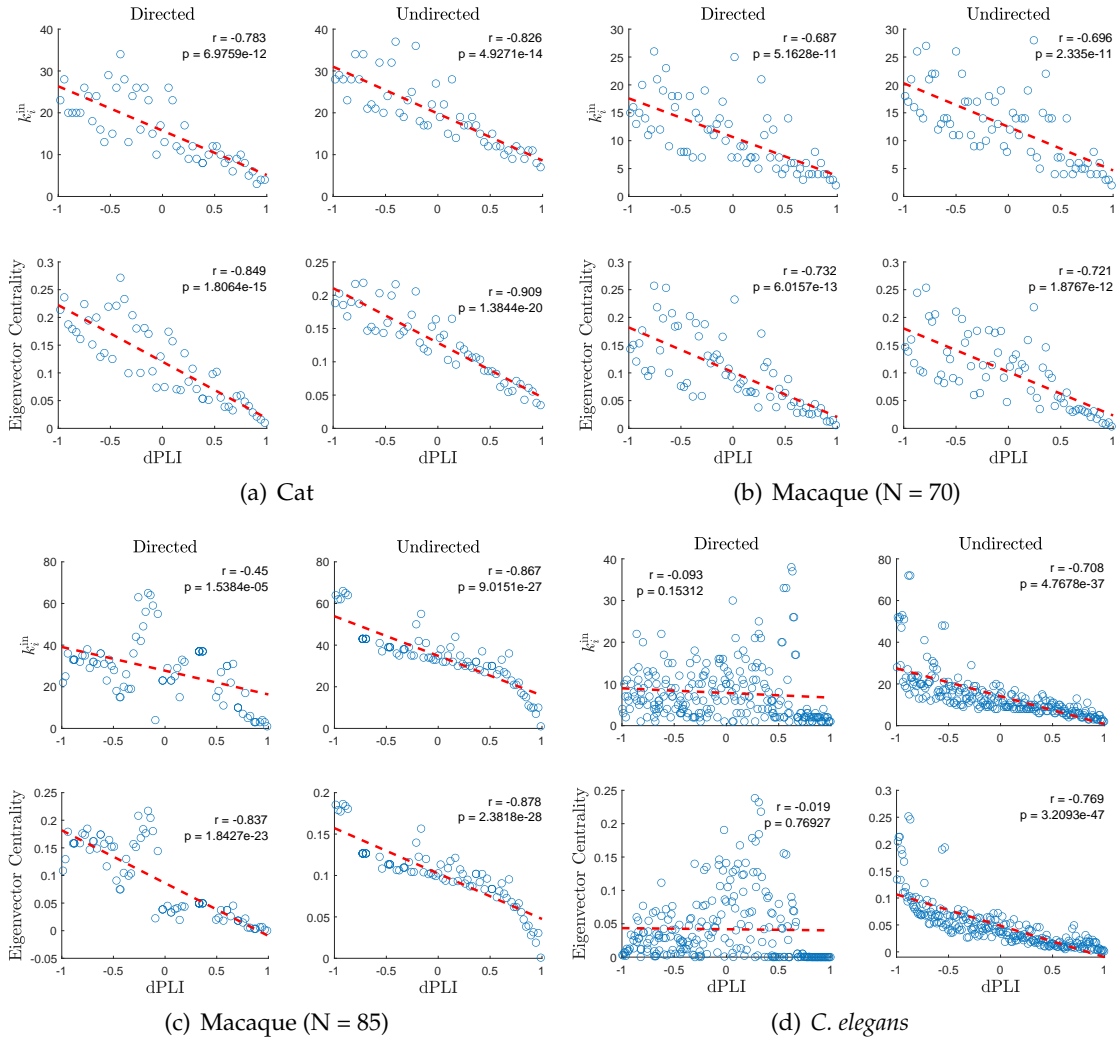


Figure 4.11: Scatter plots of dPLI Vs network degree and dPLI Vs eigenvector centrality for each of the four connectomes (cat, Macaque ($n = 70$ and $n = 85$) and *C. elegans*) for both directed and undirected representations. The red dashed lines represent the lines of best fit for each dataset.

Correlation analysis of network measures and dPLI

Next, we decided to perform a correlation analysis of dPLI against commonly deployed network measures as introduced in Chapter 2 (where appropriate). Note, however, that with the exception of network degree and eigenvector centrality (see Figure 4.11 and the text below), only weak correlations were observed and so these results have largely been relegated to Appendix D.

Figure 4.11 shows scatter plots of mean dPLI versus network degree and eigenvector centrality for all four connectomes studied in this work, as well as a plot of the line of best fit passing through the data. As one would expect, these two measures

show very similar results – it is well known that degree and eigenvector centrality are highly correlated. We see that the cat and Macaque ($n = 70$) are highly correlated ($r = -0.78, p = 7 \times 10^{-12}$ and $r = -0.69, p = 5 \times 10^{-11}$, respectively for the empirical connectomes, and $r = -0.83, p = 5 \times 10^{-14}$ and $r = -0.70, p = 2 \times 10^{-11}$, respectively for the undirected representations) as expected from our previous results, although the correlations are stronger in the case of the undirected connectomes. For the two larger networks, we see a deterioration in this relationship in the case of the empirical connectomes, which is perhaps even more evident than that displayed in the plots in Figure 4.10. Quantitatively, this deterioration can be seen via the associated p -values, which for the macaque network on $n = 85$ nodes are $p = 2 \times 10^{-5}$ and $p = 9 \times 10^{-27}$ for the directed and undirected representations, respectively; and for the *C. elegans* network are $p = 0.15$ and $p = 5 \times 10^{-37}$ for the directed and undirected representations, respectively. These results emphasise the breakdown in the inverse relationship observed by the authors of [94, 96] in the case where network directionality is included.

4.4 Summary

In this Chapter we aimed to better understand the impact that directed network topology has on synchrony properties of the brain. To address this question we simulated neural dynamics on connectome-based networks for a range of species and parcellations that contain directionality information. Neural activity is described by a phase delayed Kuramoto Model (KM), which is perhaps the simplest example of a delay-coupled oscillatory network [159] and is well-suited to assessing how directed connectomes govern synchronisation properties of the brain [160]. In particular, we found that network directionality profoundly impacts both the time-scale at which coordinated rhythmic activity occurs across large-scale brain networks as well as the stability properties of these synchronised states. We also find that recently observed relations between network structure and directed functional connectivity [96, 94], as quantified using the directed phase lag index (dPLI) [95], appear far less conclusive when network directionality is accounted for.

Conclusions

To conclude, in this chapter we review some of the main findings of this thesis and forward a number of possibilities for future research in this area.

5.1 Summary of thesis

The aim of this thesis was to determine the impact of network directionality on large-scale neural activity patterns in the brain. Typically, such models omit information on structural directionality patterns, due largely to the inability of modern non-invasive imaging technologies to infer edge directionality in the brain. Our investigations deployed brain network models, with underlying connectivity informed via a range of species (including the cat, Macaque monkey and *C. elegans* round worm), and neural activity of each node simulated using a suitable neural model. Importantly, our theoretical studies imply that network directionality can have a profound effect on network dynamics, both in terms of the connectomes information storing capabilities and synchrony-related activities such as neural learning.

After introducing the relevant background material in Chapter 1 and describing the network science concepts of pertinence to our work in Chapter 2, we started the technical work of the thesis in Chapter 3, by conducting a computational study to reveal the role of network directionality in determining the capability of a connectome-based network to store information. Deploying a graded response Hopfield model on each

node, information capacity was measured by counting the number of fixed point attractor states as a function of the model parameters. In addition, the robustness of each attractor state was determined by computing its basin stability, which approximates the size of the attractor states basin of attraction. Our study indicates that not only can directed network topology have a significant effect on the information capacity (as measured by the number of attractor states) of connectome-based networks, but it can also impact significantly the domains of attraction of these ‘brain states’. Moreover, we found that network modularity was a key mechanism underlying the formation of observed neural activity patterns, and that by neglecting network directionality we risk eliminating brain states that correlate highly with the directed topology of the brain. Finally, we observed, as in other recent studies [70, 133], a small set of prototypical direction-dependent activity patterns that potentially constitute a ‘skeleton’ of the non-stationary dynamics typically discerned in the brain.

In Chapter 4 we focussed on the role that the interplay between local dynamics and directed cortical topology has on the propensity for cortical structures to synchronise. More specifically, using the same cortical networks as in the previous chapter (cat, Macaque and *C. elegans*), we deployed numerical simulations to investigate the following questions: ‘does network directionality enhance or destabilise synchrony in the brain?’, ‘what impact does it have on the speed at which synchrony takes place?’ and ‘what role do time delays play when directionality is incorporated?’. To address these questions we simulated neural dynamics on the aforementioned connectomes using a phase delayed Kuramoto model to describe neural activity. The simplicity of the Kuramoto model is well-suited to assessing how directionality impacts synchrony properties of the brain. Importantly, we found that network directionality has a profound impact on both the time-scale at which coordinated rhythmic activity occurs as well as the stability properties of these synchronous states. We also found that recently observed relations between network structure and directed functional connectivity [94, 96], as quantified using the directed phase lag index [151], appear far less conclusive when network directionality is accounted for.

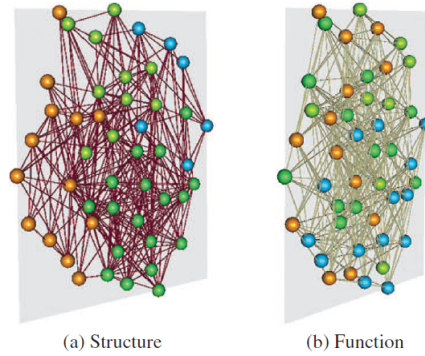


Figure 5.1: Structure-function brain network

5.2 Discussion of further work

Multilayer networks have received considerable attention over the past decade and are natural candidates for modelling the brain, due to the variety of imaging modalities used to study structure-function relations, as well as the multitude of different scales at which neural interactions occur. However, as with standard network analyses the majority of investigations restrict to binary, undirected network representations. Thus, it would be of great interest to construct multilayer network models incorporating both directed structural (where possible) *and* directed functional information. For example, following [33, 99, 161], we would propose to extend these multiplex structure-function brain network models (*i.e.* two layer models with a layer each for structure and function – see Figure 5.1) to fully incorporate directionality, and indeed, to extend where appropriate, these measures (*e.g.* structure-function clustering) to the fully directed case. We hypothesise that the inclusion of network directionality would provide additional insights beyond a traditional (*i.e.* undirected) network analysis and so potentially lead to improved understanding of the mechanisms underlying structure-function relations in the brain.

Additionally, we could extend these models to incorporate time, by modelling the brain as a time-evolving multiplex network [162, 163, 164]; thus allowing us to consider dynamic aspects of structure-function relations. A novel temporal structure-function multiplex model of so-called dynamic functional connectivity (see [165] and references therein) in healthy and diseased brains, promises to provide a holistic understanding

of brain function and thus reveal key mechanisms underlying structure-function relations. Dynamic functional networks have recently been deployed to model a range of neural diseases such as epilepsy [92, 166], Parkinson's disease [167], and Alzheimer's disease [168], yet these models study function in isolation, typically omitting important structural information. Incorporating important biological details (such as structural weights and directionality) is likely key to forwarding the practical applications of network neuroscience, an area that is still in its infancy despite 20 years of research.

Cortical network modularity

In this appendix we display the results of performing a modularity analysis on both the empirical and undirected cortical networks studied in this work: Macaque (71 and 95 nodes); cat and *C. elegans*. All calculations were performed using a multi-iterative generalisation of the Louvain community detection algorithm which estimates optimal modularity structure of a network and is available via the Matlab Brain Connectivity Toolbox (see [57] and references therein for further details). Note that all calculations were performed using the default parameters.

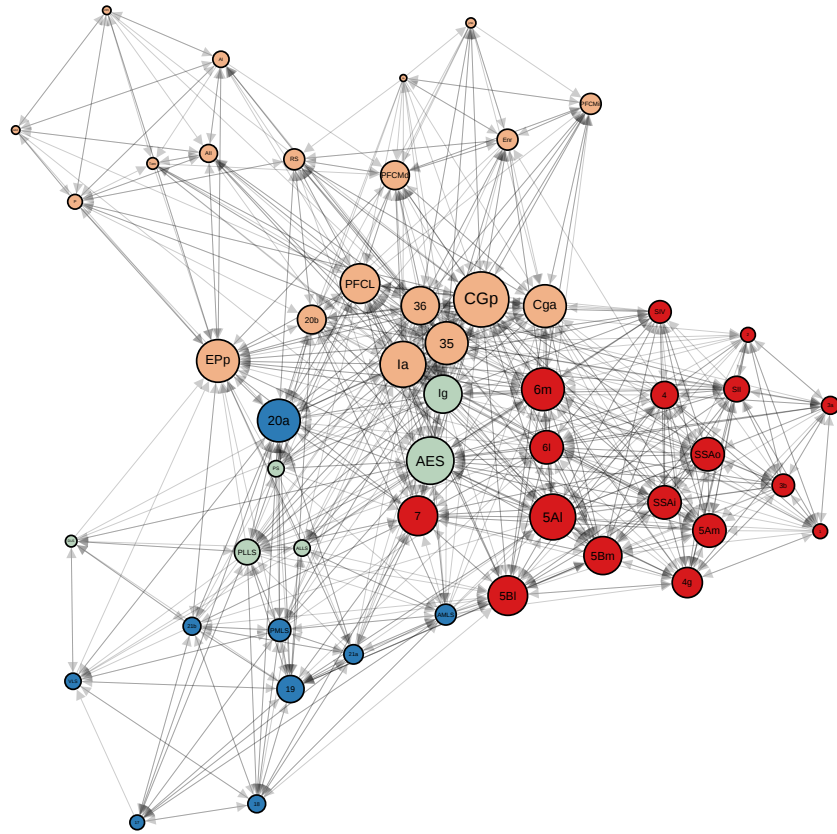
Modularity scores and number of modules for empirical and undirected networks for each species is given in Table A.1., whilst colour coded plots including labelled nodes (denoting either brain regions or neurons) are shown in figures A.1–A.4.

Connectome	Cat		M71		M95		CE	
	D	U	D	U	D	U	D	U
modularity	0.36	0.26	0.4	0.38	0.4	0.35	0.43	0.39
# of modules	4	3	4	4	3	3	6	5

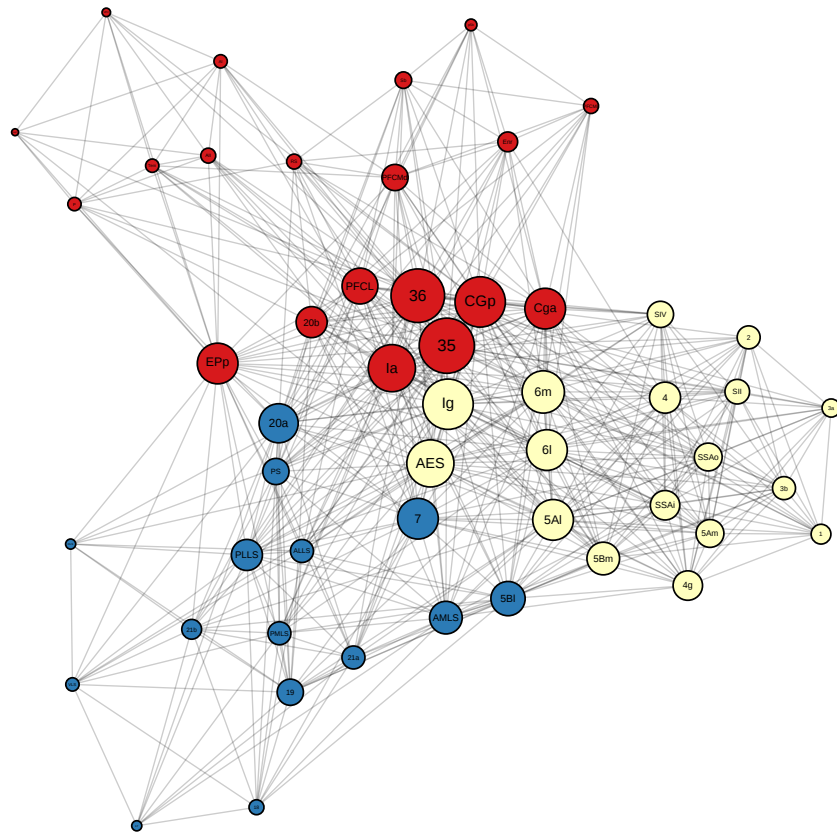
Table A.1: Network statistics for the original directed connectomes (D) and their undirected representations (U). Here, M71 and M95 denote the Macaque connectomes on 71 and 95 nodes, respectively, whilst CE denotes the *C. elegans* connectome.

Networks were produced using the Gephi software [169] and nodes were laid out either using available x - y coordinates of cortical brain regions/neurons (Macaque $n = 95$ and *C. elegans*) or else using the Yifan Hu algorithm [170]. In all cases node size is proportional to the in-degree or degree for the empirical or undirected networks, respec-

tively.

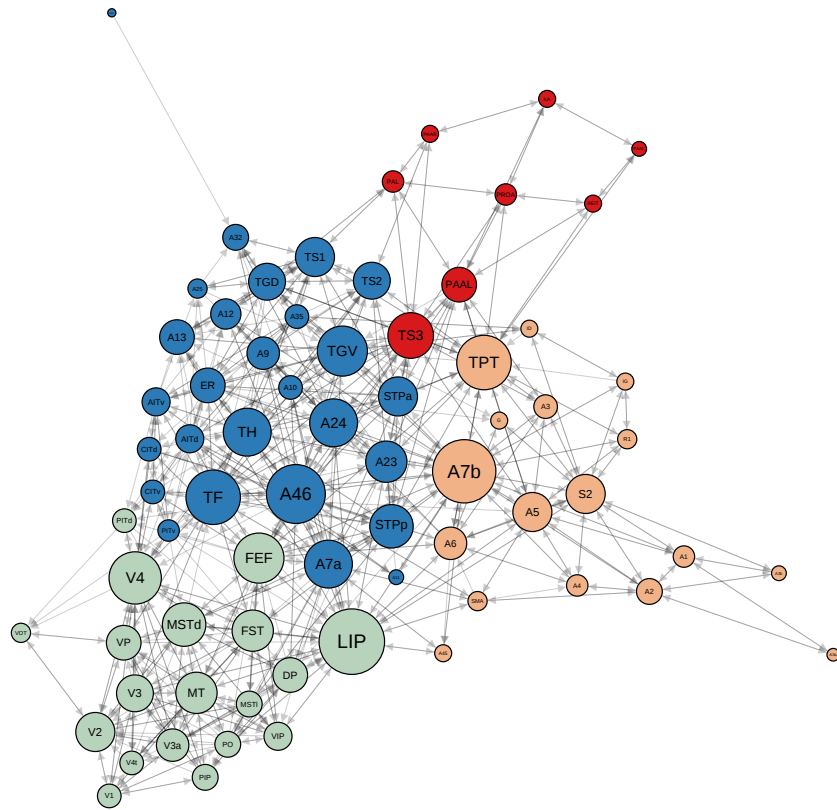


(a) empirical

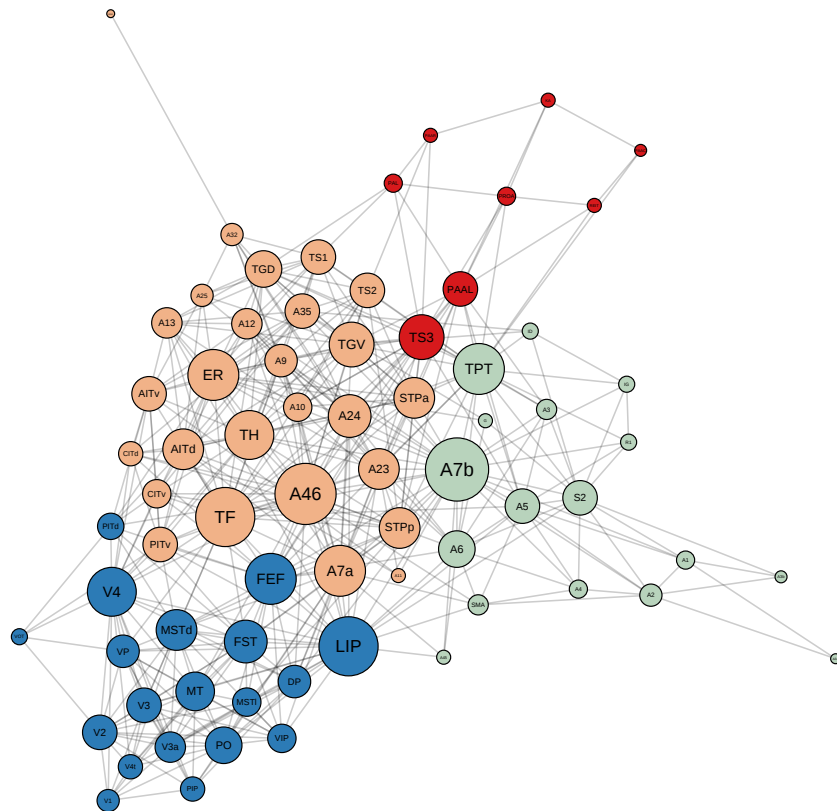


(b) undirected

Figure A.1: Modularity structure for empirical and undirected anatomical networks for the cat cortex ($n = 52$). Node colour is based on the communities identified by the Modularity score. Node size is proportional to the in-degree and degree, respectively. Nodes are labelled using the standard cortical atlas.

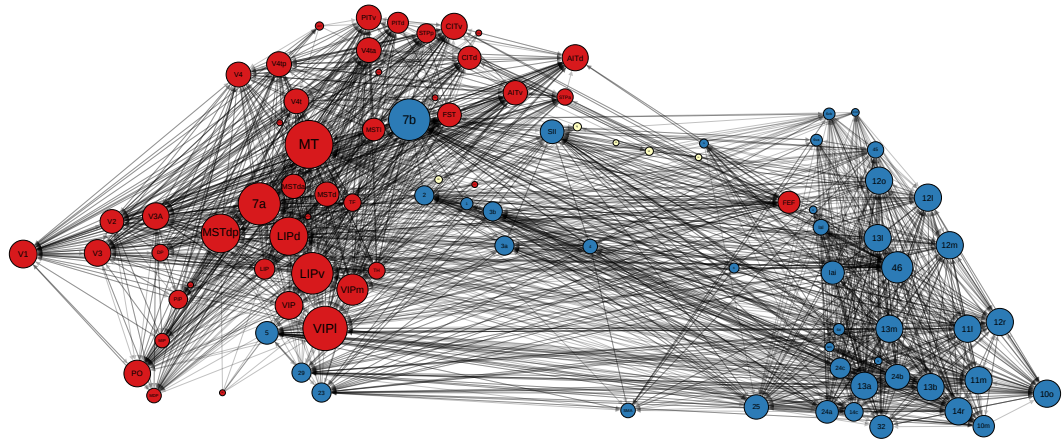


(a) empirical

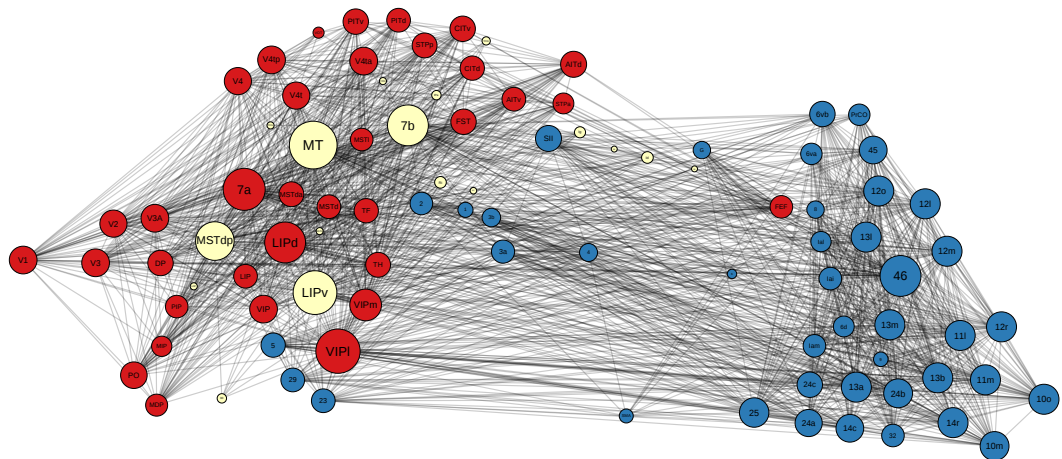


(b) undirected

Figure A.2: Modularity structure for empirical and undirected anatomical networks for the Macaque cortex ($n = 71$). Node colour is based on the communities identified by the Modularity score. Node size is proportional to the in-degree and degree, respectively. Nodes are labelled using the standard cortical atlas.



(a) empirical



(b) undirected

Figure A.3: Modularity structure for empirical and undirected anatomical networks for the Macaque cortex ($n = 95$). Node colour is based on the communities identified by the Modularity score. Node size is proportional to the in-degree and degree, respectively. Nodes are labelled using the standard cortical atlas.

Neural network activity patterns

In this appendix we display final activation patterns for both empirical and undirected networks for the species studied in this thesis: cat, two parcellations of the Macaque monkey and *C. elegans*. In each case we display only solutions with a basin stability score of at least 1% (note this is smaller than the 5% criteria used in Chapter 3 for purposes of comparison) since as argued earlier patterns with smaller basin stabilities are unlikely to be observed in practice.

It is noteworthy that in all cases the driving force behind these states would appear to be the modularity structure (see Appendix A). For the mammalian networks the empirical representation displays a greater number of ‘significant’ solutions than the undirected networks, a situation that is reversed for the micro-scale *C. elegans* connectome. In all cases we find that activity is increased in the undirected networks suggesting a possible role for directionality in neural inhibition, a fact that is related to the loss of modularity in the undirected networks.

Finally, we note that in the plots of the *C. elegans* and Macaque ($n = 95$) networks node coordinates were obtained by projecting the spatial position of the corresponding brain regions onto the x - y plane. In all other cases the layout was the result of applying the Yifan Hu algorithm (see [170] for a discussion of the different methods for laying out large-scale networks). In all instances node size is proportional to the in-degree or degree for the empirical or undirected networks, respectively.

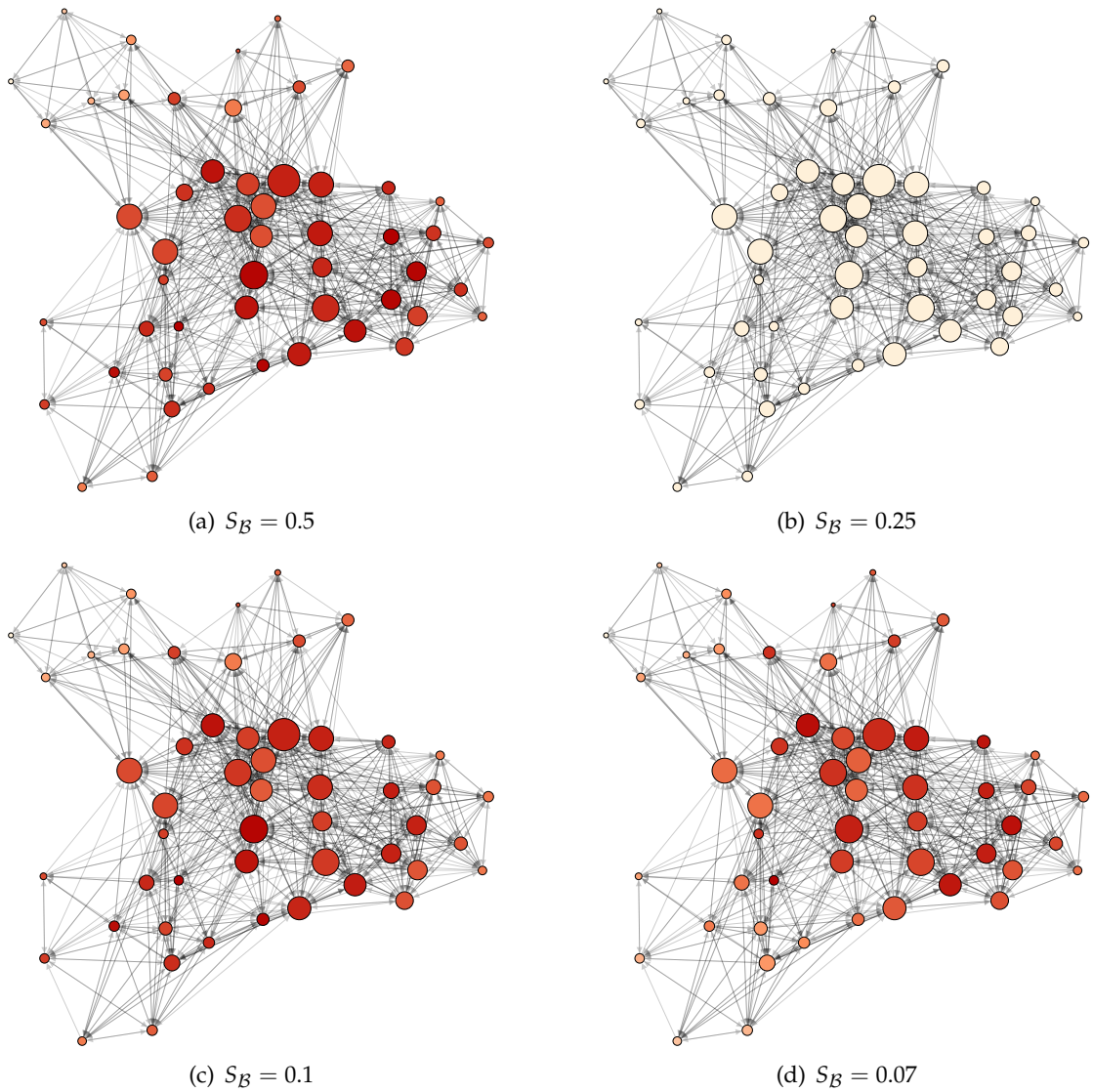


Figure B.1: Final activation patterns (*i.e.* network states) for the empirical Cat network on 52 nodes along with their respective basin stabilities. Here $P = 0.9$ and solutions shown are those with basin stability scores of at least 1%.

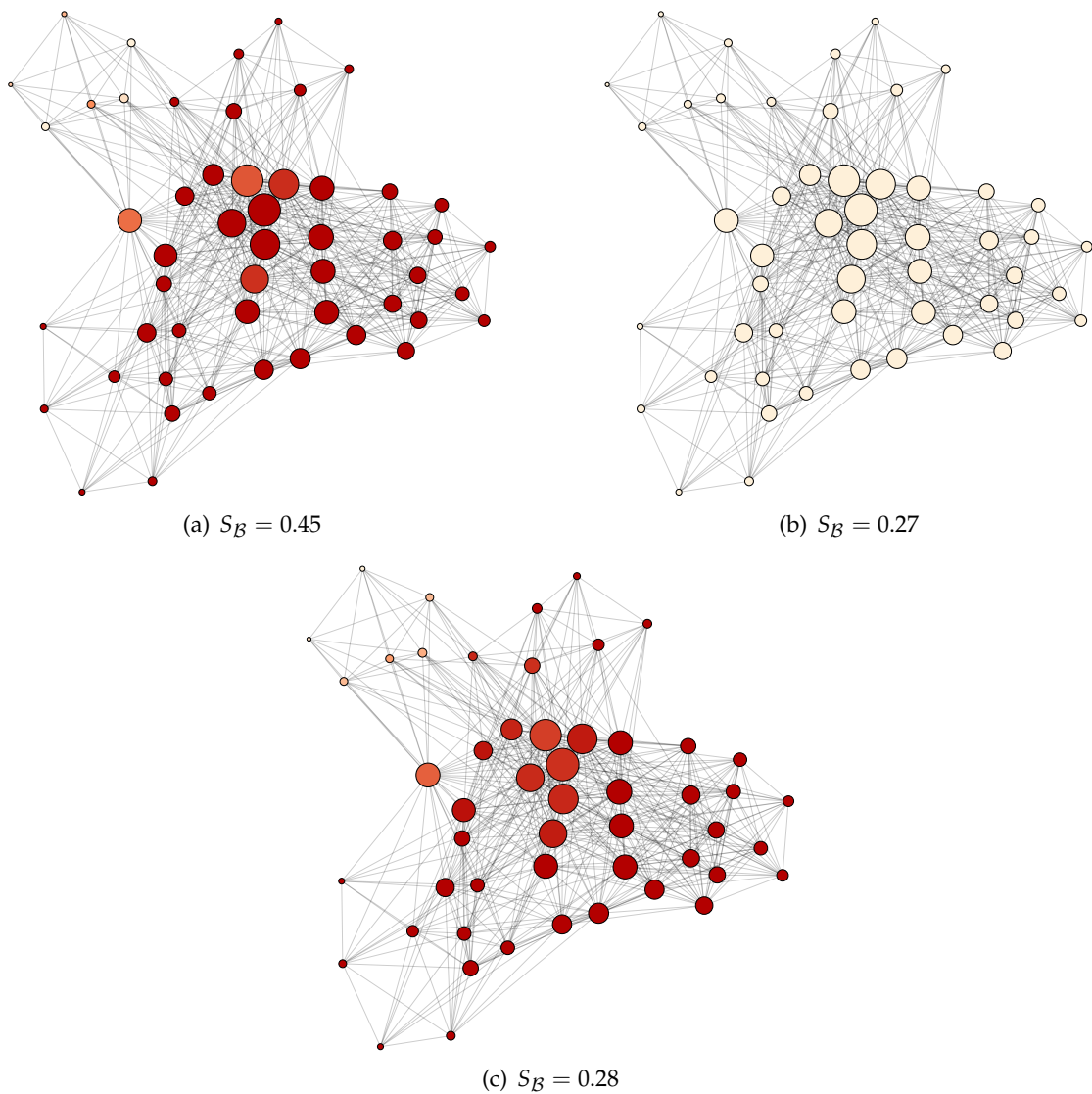


Figure B.2: Final activation patterns (*i.e.* network states) for the undirected Cat network on 52 nodes along with their respective basin stabilities. Here $P = 0.9$ and solutions shown are those with basin stability scores of at least 1%.

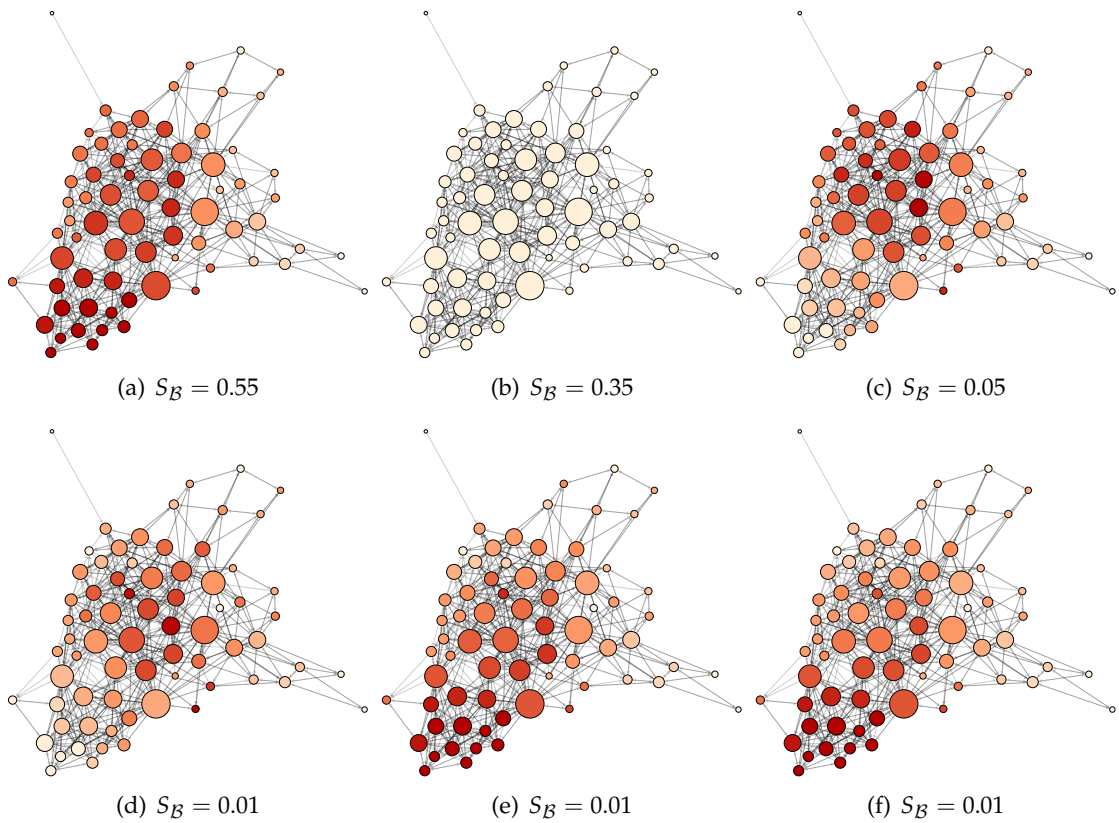


Figure B.3: Final activation patterns (*i.e.* network states) for the empirical Macaque network on 71 nodes along with their respective basin stabilities. Here $P = 0.8$ and solutions shown are those with basin stability scores of at least 1%.

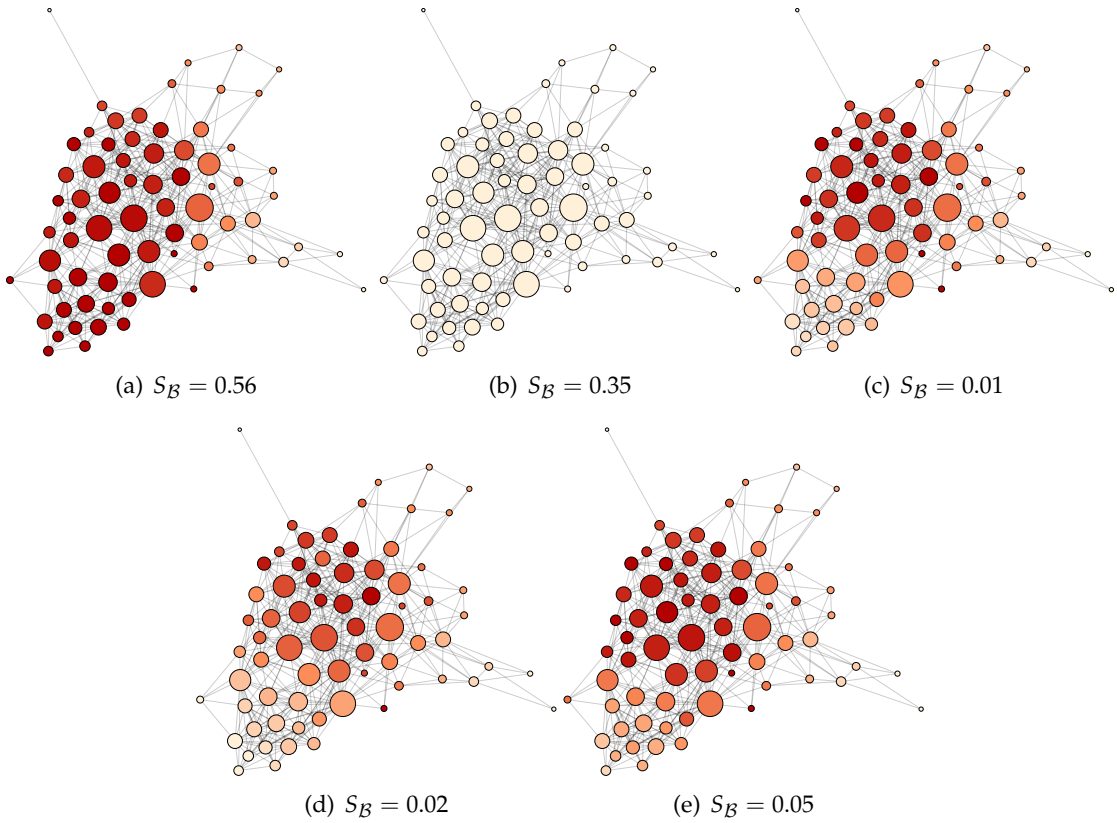


Figure B.4: Final activation patterns (*i.e.* network states) for the undirected Macaque network on 71 nodes along with their respective basin stabilities. Here $P = 0.8$ and solutions shown are those with basin stability scores of at least 1%.

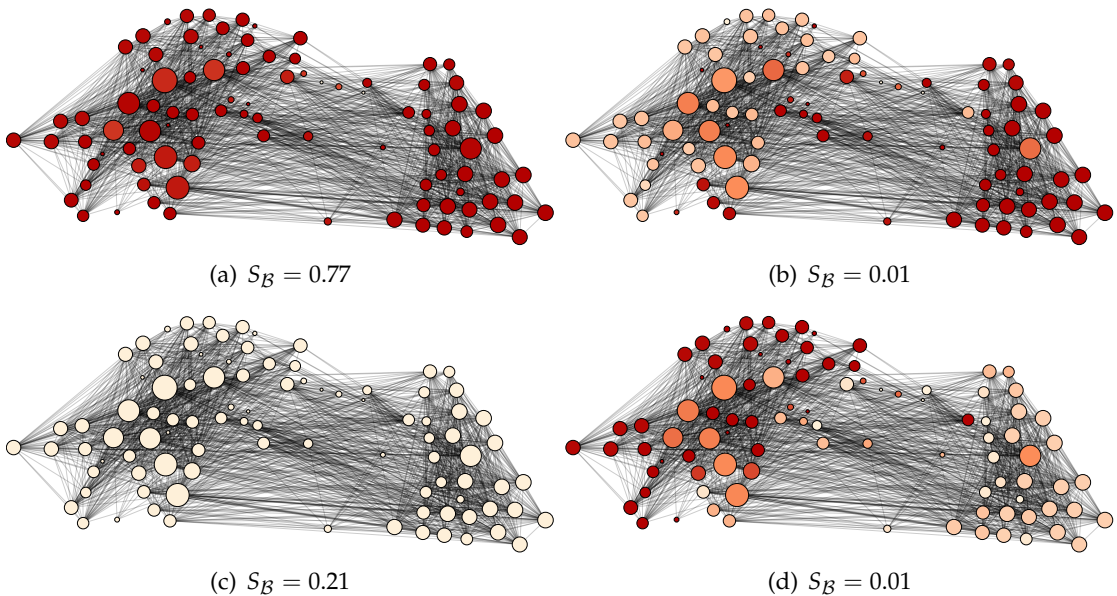


Figure B.5: Final activation patterns (*i.e.* network states) for the undirected Macaque network on 95 nodes along with their respective basin stabilities. Here $P = 1.1$ and solutions shown are those with basin stability scores of at least 1%.

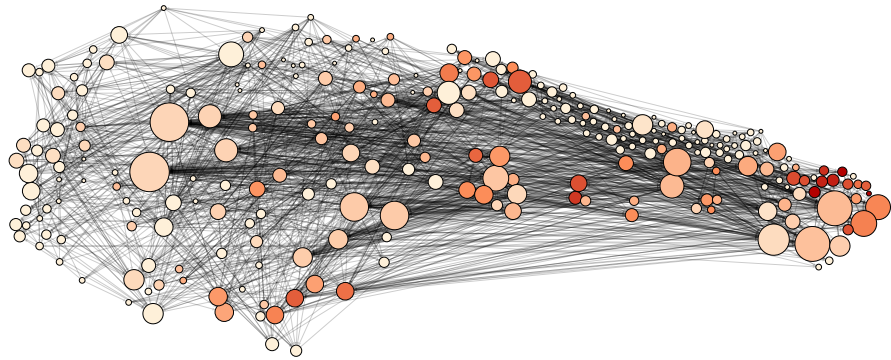
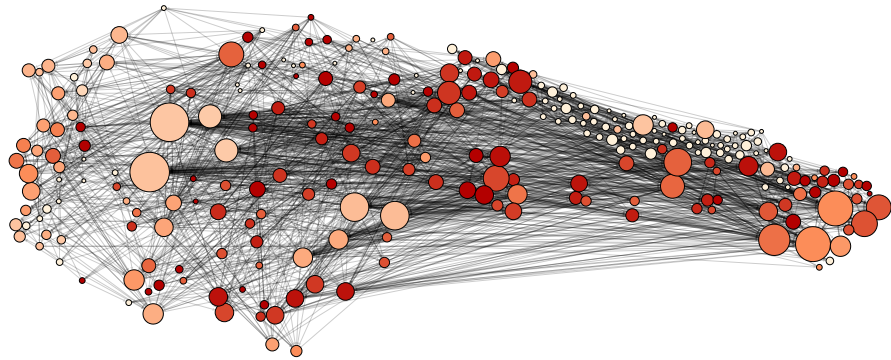
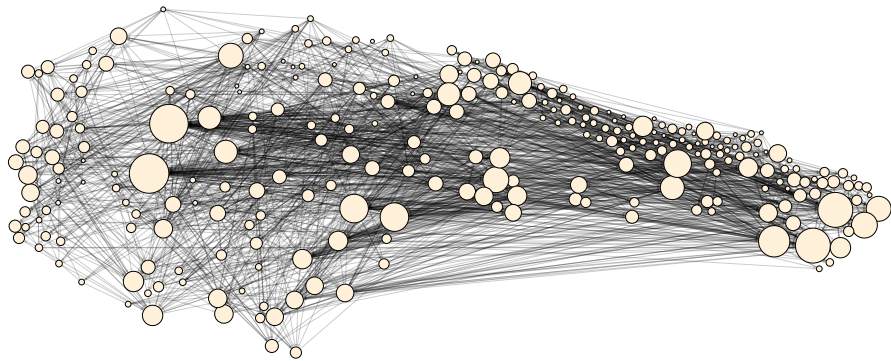
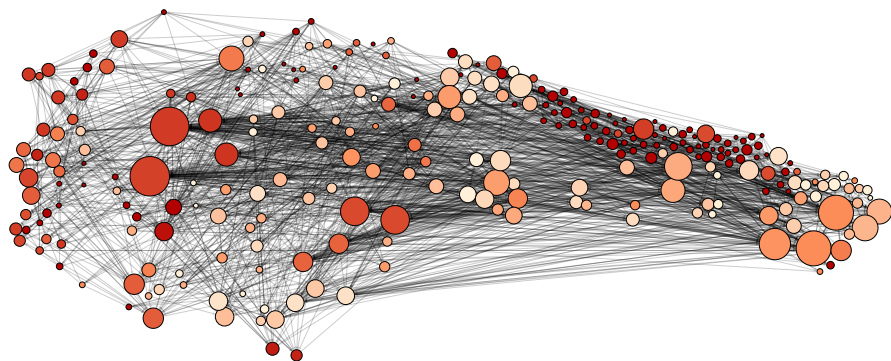
(a) $S_B = 0.05$ (b) $S_B = 0.6$ (c) $S_B = 0.1$ (d) $S_B = 0.25$

Figure B.6: Final activation patterns (*i.e.* network states) for the empirical *C. elegans* network on 277 nodes along with their respective basin stabilities. Here $P = 1$ and solutions shown are those with basin stability scores of at least 1%.

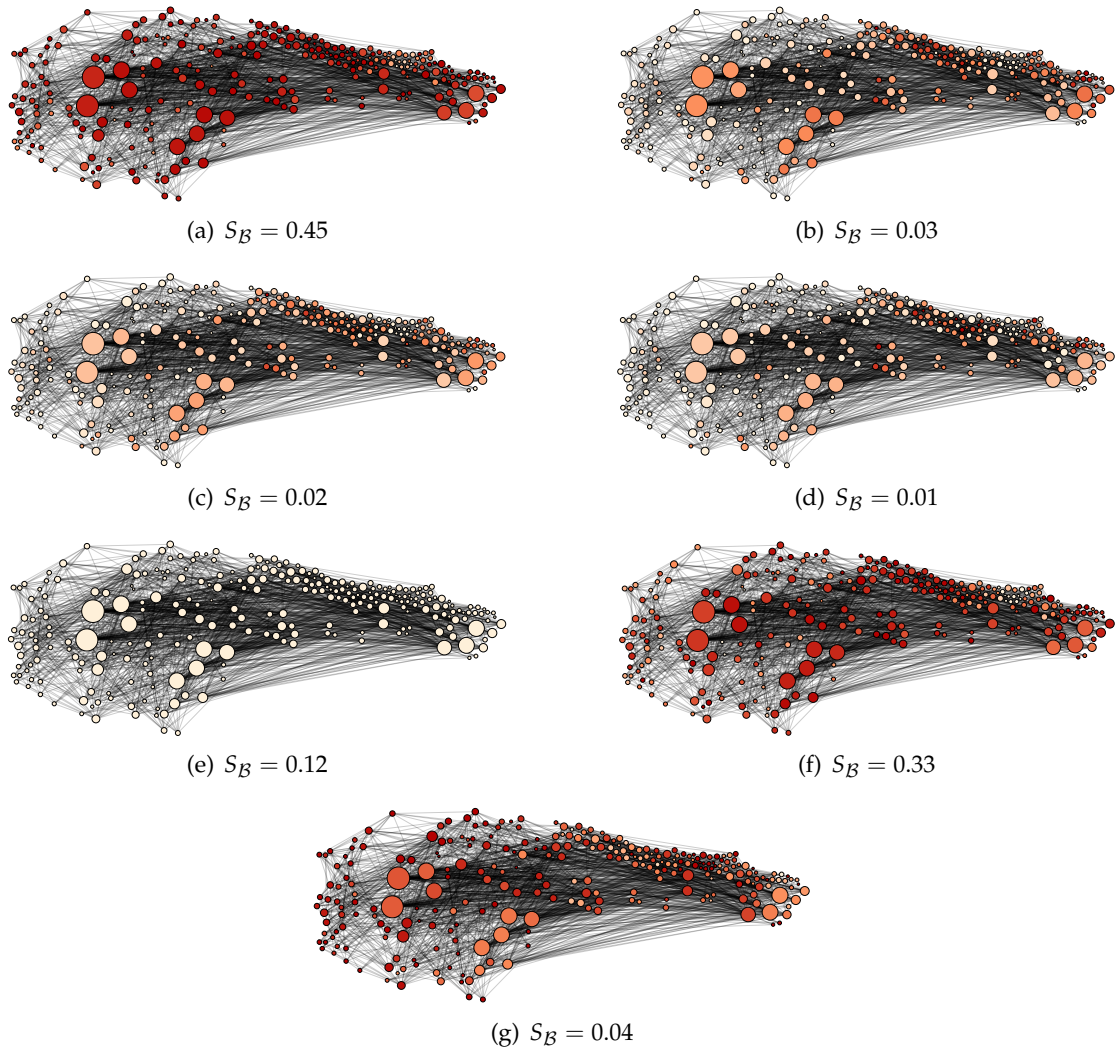


Figure B.7: Final activation patterns (*i.e.* network states) for the undirected *C. elegans* network on 277 nodes along with their respective basin stabilities. Here $P = 1$ and solutions shown are those with basin stability scores of at least 1%.

Clustering of activity patterns for *C. elegans* neural network

From the basin stability plots for *C. elegans* (see figures 3.7(a) and 3.7(b)) we see that many of the observed attractor states are similar in magnitude. This observation motivates the use of a clustering algorithm to identify whether a smaller class of spatially similar attractor states exists, thus reducing the complexity of the attractor state set and making any analysis more amenable.

As a measure of similarity between attractor states we deploy the Euclidean distance:

$$d(\mathbf{p}, \mathbf{q}) = \sqrt{\sum_{i=1}^n (p_i - q_i)^2}, \quad (\text{C.1})$$

which results in a distance matrix $D \in \mathbb{R}^{N \times N}$, where the ij^{th} entry of D gives the similarity between attractor states i and j . Here, N is the number of attractor states found (for each choice of P) for each of the *C. elegans* connectomes (*i.e.* the empirical and undirected network representations). This then enables us to group the solutions and perform a cluster analysis based on spatial proximity.

We perform hierarchical clustering (see, for example, the excellent text [171]) using the built-in routines from the Matlab Statistics and Machine Learning Toolbox in order to reproduce coarse-grained versions of the basin stability plots of Chapter 3. More specifically, for each value of P , clustering was applied on the attractor set of each

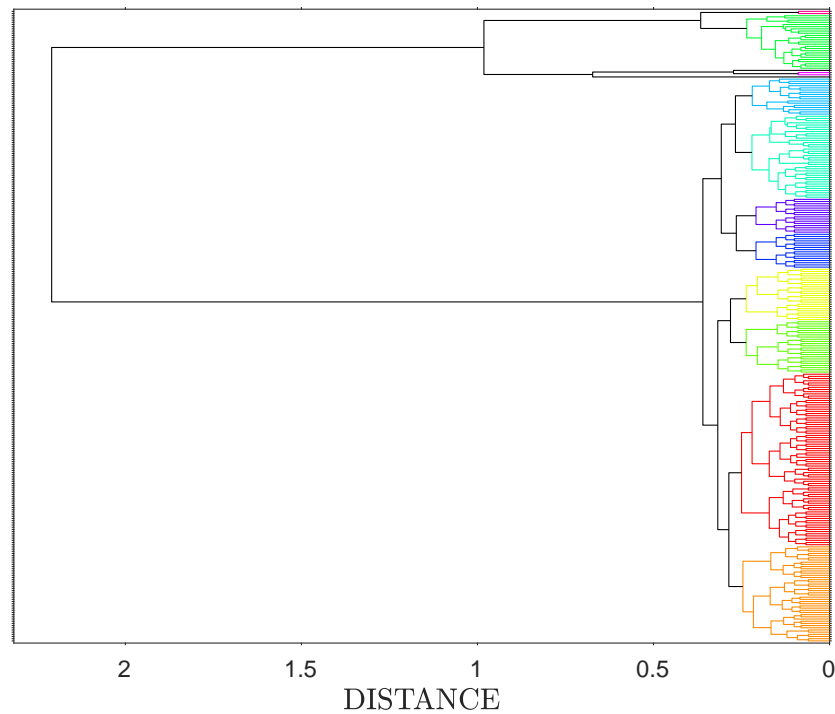


Figure C.1: Dendrogram displaying results of a cluster analysis of the attractor set of the undirected *C. elegans* network for $P = 0.9$. The horizontal axis represents the distance or dissimilarity between clusters. The vertical axis represents the objects (attractor states) and clusters.

connectome (see Figure C.1 for an illustrative example; here, we deploy the undirected *C. elegans* connectome and set $P = 0.9$), and the basin stabilities of attractor states belonging to the same clusters were combined.

The resulting basin stability plots are shown in figures C.2 and C.3. As can be seen from figures C.1-C.3 there is both a significant variation in the size of the cluster states as well as their relative importance – as measured via the basin stability score. We find that in both cases the number of significant attractor states is relatively small, ranging from 3-5 attractor states for the empirical connectome to 5-10 for the undirected connectome. Thus the observed complexities in figures 3.7(a) and 3.7(b) would appear to be due to the existence of a large number of ‘similar’ attractor states – note that such apparent redundancies are common in biological networks and believed to play a crucial role in the robustness of many biological processes [172].

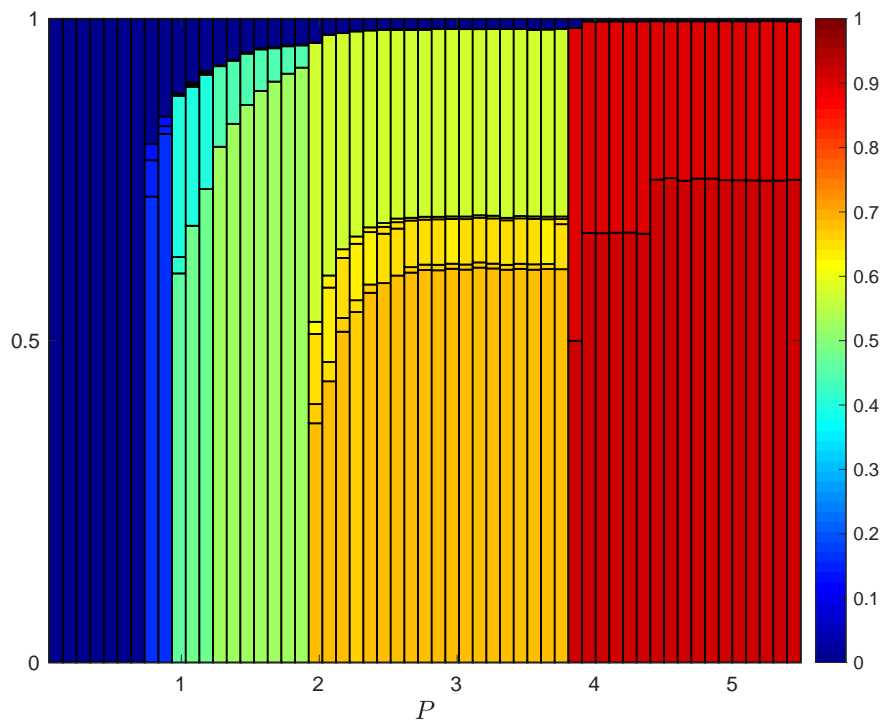


Figure C.2: Basin stability for the clustered attractor states as a function of P for the empirical *C. elegans* neuronal network. Cluster states are coloured according to their average magnitude as measured by the one-norm.

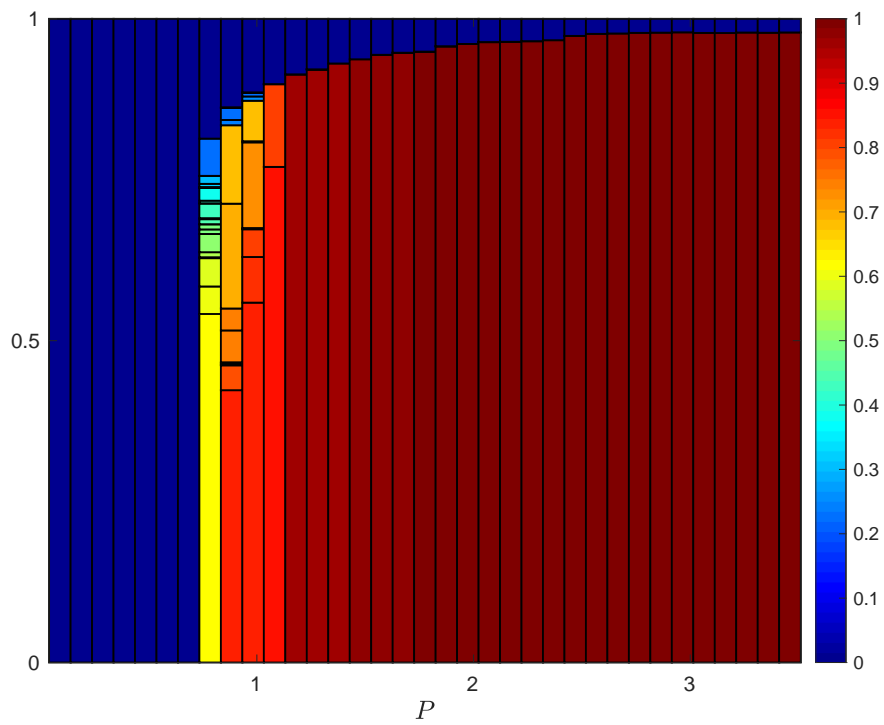


Figure C.3: Basin stability for the clustered attractor states as a function of P for the undirected *C. elegans* neuronal network. Cluster states are coloured according to their average magnitude as measured by the one-norm.

Other network measures correlation with dPLI

In this Appendix we display results for a correlation analysis of mean dPLI versus local clustering and betweenness centrality (Figure D.1). Note that correlations were observed (see figures for r and p -values) over some of the connectomes but neither measure displayed a relationship with phase against all connectomes.

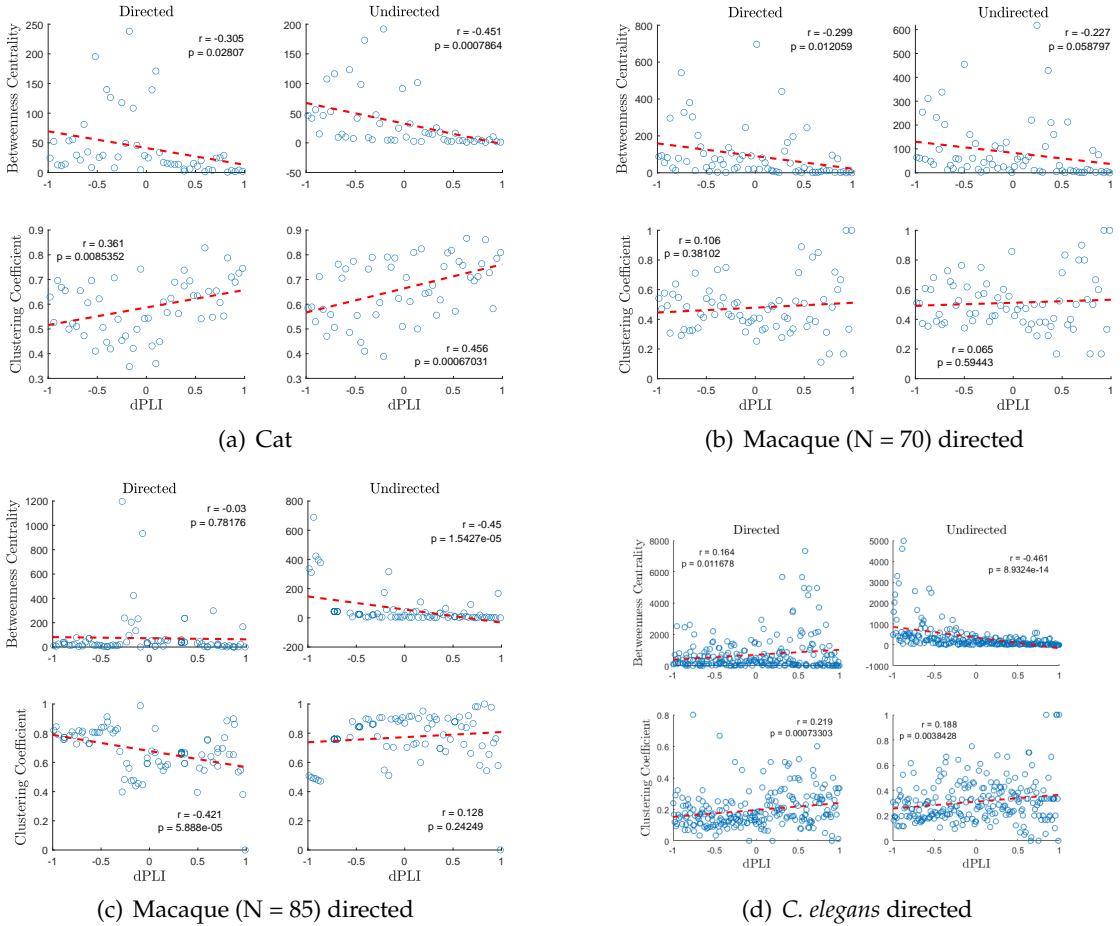


Figure D.1: Scatter plots of dPLI Vs betweenness centrality and dPLI Vs local clustering for each of the four connectomes (cat, Macaque ($n = 70$ and $n = 85$) and *C. elegans*) for both directed and undirected representations. The red dashed lines represent the lines of best fit for each dataset.

References

- [1] Réka Albert, István Albert, and Gary L Nakarado. Structural vulnerability of the north american power grid. *Physical review E*, 69(2):025103, 2004.
- [2] Sergio Arianos, Ettore Bompard, Anna Carbone, and Fei Xue. Power grid vulnerability: A complex network approach. *Chaos: An Interdisciplinary Journal of Nonlinear Science*, 19(1):013119, 2009.
- [3] Danielle S Bassett and Olaf Sporns. Network neuroscience. *Nature neuroscience*, 20(3):353, 2017.
- [4] Jacob J Blum and Robert B Stein. On the analysis of metabolic networks. In *Biological regulation and development*, pages 99–125. Springer, 1982.
- [5] Hawoong Jeong, Bálint Tombor, Réka Albert, Zoltan N Oltvai, and A-L Barabási. The large-scale organization of metabolic networks. *Nature*, 407(6804):651, 2000.
- [6] Soon-Hyung Yook, Zoltán N Oltvai, and Albert-László Barabási. Functional and topological characterization of protein interaction networks. *Proteomics*, 4(4):928–942, 2004.
- [7] Réka Albert, Hawoong Jeong, and Albert-László Barabási. Internet: Diameter of the world-wide web. *nature*, 401(6749):130, 1999.
- [8] Sarah J Jackson and Brooke Foucault Welles. Hijacking# mynypd: Social media dissent and networked counterpublics. *Journal of Communication*, 65(6):932–952, 2015.

- [9] Leonhard Euler. Leonhard euler and the königsberg bridges. *Scientific American*, 189(1):66–72, 1953.
- [10] GA Dirac. Map-colour theorems. *Canadian Journal of Mathematics*, 4:480–490, 1952.
- [11] Oystein Ore et al. Graphs and matching theorems. *Duke Mathematical Journal*, 22(4):625–639, 1955.
- [12] Claude Berge. Two theorems in graph theory. *Proceedings of the National Academy of Sciences of the United States of America*, 43(9):842, 1957.
- [13] Robin J Wilson. *Introduction to graph theory*. Pearson Education India, 1979.
- [14] Douglas Brent West et al. *Introduction to graph theory*, volume 2. Prentice hall Upper Saddle River, NJ, 1996.
- [15] Paul Erdős and Alfréd Rényi. On the evolution of random graphs. *Publ. Math. Inst. Hung. Acad. Sci*, 5(1):17–60, 1960.
- [16] Stanley Milgram. The small world problem. *Psychology today*, 2(1):60–67, 1967.
- [17] R Duncan Luce and Albert D Perry. A method of matrix analysis of group structure. *Psychometrika*, 14(2):95–116, 1949.
- [18] Mino Ashtiani, Ali Salehzadeh-Yazdi, Zahra Razaghi-Moghadam, Holger Hennig, Olaf Wolkenhauer, Mehdi Mirzaie, and Mohieddin Jafari. A systematic survey of centrality measures for protein-protein interaction networks. *BMC systems biology*, 12(1):80, 2018.
- [19] Leo Katz. A new status index derived from sociometric analysis. *Psychometrika*, 18(1):39–43, 1953.
- [20] Linton C Freeman. A set of measures of centrality based on betweenness. *Sociometry*, pages 35–41, 1977.
- [21] Duncan J Watts and Steven H Strogatz. Collective dynamics of ‘small-world’ networks. *nature*, 393(6684):440, 1998.

- [22] Albert-László Barabási and Réka Albert. Emergence of scaling in random networks. *science*, 286(5439):509–512, 1999.
- [23] Michelle Girvan and Mark EJ Newman. Community structure in social and biological networks. *Proceedings of the national academy of sciences*, 99(12):7821–7826, 2002.
- [24] Mark EJ Newman. Modularity and community structure in networks. *Proceedings of the national academy of sciences*, 103(23):8577–8582, 2006.
- [25] Vincent D Blondel, Jean-Loup Guillaume, Renaud Lambiotte, and Etienne Lefebvre. Fast unfolding of communities in large networks. *Journal of statistical mechanics: theory and experiment*, 2008(10):P10008, 2008.
- [26] Giulio Tononi, Olaf Sporns, and Gerald M Edelman. A measure for brain complexity: relating functional segregation and integration in the nervous system. *Proceedings of the National Academy of Sciences*, 91(11):5033–5037, 1994.
- [27] Mikko Kivela, Alex Arenas, Marc Barthelemy, James P Gleeson, Yamir Moreno, and Mason A Porter. Multilayer networks. *Journal of complex networks*, 2(3):203–271, 2014.
- [28] Barry Bentley, Robyn Branicky, Christopher L Barnes, Yee Lian Chew, Eviatar Yemini, Edward T Bullmore, Petra E Vértés, and William R Schafer. The multilayer connectome of *caenorhabditis elegans*. *PLoS computational biology*, 12(12):e1005283, 2016.
- [29] Kanad Mandke, Jil Meier, Matthew J Brookes, Reuben D O’dea, Piet Van Mieghem, Cornelis J Stam, Arjan Hillebrand, and Prejaas Tewarie. Comparing multilayer brain networks between groups: Introducing graph metrics and recommendations. *NeuroImage*, 166:371–384, 2018.
- [30] Federico Battiston, Vincenzo Nicosia, and Vito Latora. Structural measures for multiplex networks. *Physical Review E*, 89(3):032804, 3 2014.

- [31] Albert Solé-Ribalta, Manlio De Domenico, Sergio Gómez, and Alex Arenas. Centrality rankings in multiplex networks. In *Proceedings of the 2014 ACM conference on Web science*, pages 149–155. ACM, 2014.
- [32] Sergio Gomez, Albert Diaz-Guilera, Jesus Gomez-Gardenes, Conrad J Perez-Vicente, Yamir Moreno, and Alex Arenas. Diffusion dynamics on multiplex networks. *Physical review letters*, 110(2):028701, 2013.
- [33] Federico Battiston, Vincenzo Nicosia, Mario Chavez, and Vito Latora. Multilayer motif analysis of brain networks. *Chaos: An Interdisciplinary Journal of Nonlinear Science*, 27(4):047404, 2017.
- [34] Manlio De Domenico. Multilayer modeling and analysis of human brain networks. *GigaScience*, 6(5):1–8, 2017.
- [35] Arda Halu, Manlio De Domenico, Alex Arenas, and Amitabh Sharma. The multiplex network of human diseases. *NPJ systems biology and applications*, 5(1):15, 2019.
- [36] JA Scott Kelso. *Dynamic patterns: The self-organization of brain and behavior*. MIT press, 1997.
- [37] Olaf Sporns. *Networks of the Brain*. MIT press, 2010.
- [38] Richard F Betzel and Danielle S Bassett. Multi-scale brain networks. *Neuroimage*, 160:73–83, 2017.
- [39] Brain power grade 4-5. background. <https://www.drugabuse.gov/publications/brain-power/grades-4-5/neurotransmission-module-3/background>. Accessed: 27-08-2019.
- [40] Michael Vaiana and Sarah Feldt Muldoon. Multilayer brain networks. *Journal of Nonlinear Science*, 30(5):2147–2169, 2020.
- [41] David C Van Essen, Kamil Ugurbil, Edward Auerbach, Deanna Barch, Timothy EJ Behrens, Richard Bucholz, Acer Chang, Liyong Chen, Maurizio Corbetta,

- Sandra W Curtiss, et al. The human connectome project: a data acquisition perspective. *Neuroimage*, 62(4):2222–2231, 2012.
- [42] Dan Goldowitz. Allen reference atlas. a digital color brain atlas of the c57bl/6j male mouse-by hw dong. *Genes, Brain and Behavior*, 9(1):128–128, 2010.
- [43] Theodore B Achacoso and William S Yamamoto. *AY's Neuroanatomy of C. elegans for Computation*. CRC Press, 1991.
- [44] Michael W Davidson and Mortimer Abramowitz. Optical microscopy. *Encyclopedia of imaging science and technology*, 2002.
- [45] Liqun Luo, Edward M Callaway, and Karel Svoboda. Genetic dissection of neural circuits. *Neuron*, 57(5):634–660, 2008.
- [46] Jinhui Wang, Liang Wang, Yufeng Zang, Hong Yang, Hehan Tang, Qiyong Gong, Zhang Chen, Chaozhe Zhu, and Yong He. Parcellation-dependent small-world brain functional networks: a resting-state fmri study. *Human brain mapping*, 30(5):1511–1523, 2009.
- [47] Stephen A Engel, David E Rumelhart, Brian A Wandell, Adrian T Lee, Gary H Glover, Eduardo-Jose Chichilnisky, and Michael N Shadlen. fmri of human visual cortex. *Nature*, 1994.
- [48] Orvar Eeg-Olofsson, Ingemar Petersén, and Ulla Selldén. The development of the electroencephalogram in normal children from the age of 1 through 15 years—paroxysmal activity. *Neuropädiatrie*, 2(04):375–404, 1971.
- [49] EA Allen, E Damaraju, T Eichele, L Wu, and Vince Daniel Calhoun. Eeg signatures of dynamic functional network connectivity states. *Brain topography*, 31(1):101–116, 2018.
- [50] David Cohen. Magnetoencephalography: detection of the brain's electrical activity with a superconducting magnetometer. *Science*, 175(4022):664–666, 1972.
- [51] Olivier David and Karl J Friston. A neural mass model for meg/eeg:: coupling and neuronal dynamics. *NeuroImage*, 20(3):1743–1755, 2003.

- [52] Jan-Mathijs Schoffelen and Joachim Gross. Source connectivity analysis with meg and eeg. *Human brain mapping*, 30(6):1857–1865, 2009.
- [53] Morteza Afrasiabi and Neda Noroozian. Advantages and limitations of functional magnetic resonance imaging (fmri) of the human visual brain. *Horizons in Neuroscience Research Series; Costa, A., Villalba, E., Eds*, pages 65–72, 2015.
- [54] Karl Pearson. Note on regression and inheritance in the case of two parents. *Proceedings of the Royal Society of London*, 58:240–242, 1895.
- [55] Florian Mormann, Klaus Lehnertz, Peter David, and Christian E Elger. Mean phase coherence as a measure for phase synchronization and its application to the eeg of epilepsy patients. *Physica D: Nonlinear Phenomena*, 144(3-4):358–369, 2000.
- [56] Karl J Friston. Functional and effective connectivity: a review. *Brain connectivity*, 1(1):13–36, 2011.
- [57] Mikail Rubinov and Olaf Sporns. Complex network measures of brain connectivity: uses and interpretations. *Neuroimage*, 52(3):1059–1069, 2010.
- [58] Penelope Kale, Andrew Zalesky, and Leonardo L Gollo. Estimating the impact of structural directionality: How reliable are undirected connectomes? *Network Neuroscience*, 2(02):259–284, 2018.
- [59] Uri Alon. Network motifs: theory and experimental approaches. *Nature Reviews Genetics*, 8(6):450–461, 2007.
- [60] Alan L Hodgkin and Andrew F Huxley. A quantitative description of membrane current and its application to conduction and excitation in nerve. *The Journal of physiology*, 117(4):500–544, 1952.
- [61] Wulfram Gerstner and Werner M Kistler. *Spiking neuron models: Single neurons, populations, plasticity*. Cambridge university press, 2002.
- [62] Eugene M Izhikevich. *Dynamical systems in neuroscience*. MIT press, 2007.

- [63] Hugh R Wilson and Jack D Cowan. Excitatory and inhibitory interactions in localized populations of model neurons. *Biophysical journal*, 12(1):1–24, 1972.
- [64] Ben H Jansen and Vincent G Rit. Electroencephalogram and visual evoked potential generation in a mathematical model of coupled cortical columns. *Biological cybernetics*, 73(4):357–366, 1995.
- [65] Mattia Frasca, Andre Bergner, Juergen Kurths, and Luigi Fortuna. Bifurcations in a star-like network of stuart–landau oscillators. *International Journal of Bifurcation and Chaos*, 22(07):1250173, 2012.
- [66] Michael Breakspear. Dynamic models of large-scale brain activity. *Nature neuroscience*, 20(3):340, 2017.
- [67] Rembrandt Bakker, Thomas Wachtler, and Markus Diesmann. Cocomac 2.0 and the future of tract-tracing databases. *Frontiers in neuroinformatics*, 6:30, 2012.
- [68] Gustavo Deco, Adrián Ponce-Alvarez, Dante Mantini, Gian Luca Romani, Patric Hagmann, and Maurizio Corbetta. Resting-state functional connectivity emerges from structurally and dynamically shaped slow linear fluctuations. *Journal of Neuroscience*, 33(27):11239–11252, 2013.
- [69] Ulrike Feudel, Alexander N Pisarchik, and Kenneth Showalter. Multistability and tipping: From mathematics and physics to climate and brain—minireview and preface to the focus issue. *Chaos: An Interdisciplinary Journal of Nonlinear Science*, 28(3):033501, 2018.
- [70] Gustavo Deco and Viktor K Jirsa. Ongoing cortical activity at rest: criticality, multistability, and ghost attractors. *Journal of Neuroscience*, 32(10):3366–3375, 2012.
- [71] Paula Sanz Leon, Stuart A Knock, M Marmaduke Woodman, Lia Domide, Jochen Mersmann, Anthony R McIntosh, and Viktor Jirsa. The virtual brain: a simulator of primate brain network dynamics. *Frontiers in neuroinformatics*, 7:10, 2013.
- [72] M Marmaduke Woodman, Laurent Pezard, Lia Domide, Stuart A Knock, Paula Sanz-Leon, Jochen Mersmann, Anthony R McIntosh, and Viktor Jirsa. Integrating neuroinformatics tools in the virtual brain. *Frontiers in neuroinformatics*, 8:36, 2014.

- [73] Petra Ritter, Michael Schirner, Anthony R McIntosh, and Viktor K Jirsa. The virtual brain integrates computational modeling and multimodal neuroimaging. *Brain connectivity*, 3(2):121–145, 2013.
- [74] Paula Sanz-Leon, Stuart A Knock, Andreas Spiegler, and Viktor K Jirsa. Mathematical framework for large-scale brain network modeling in the virtual brain. *Neuroimage*, 111:385–430, 2015.
- [75] Danielle S Bassett, Andreas Meyer-Lindenberg, Sophie Achard, Thomas Duke, and Edward Bullmore. Adaptive reconfiguration of fractal small-world human brain functional networks. *Proceedings of the National Academy of Sciences*, 103(51):19518–19523, 2006.
- [76] Martijn P van den Heuvel and Olaf Sporns. Network hubs in the human brain. *Trends in cognitive sciences*, 17(12):683–696, 2013.
- [77] David Meunier, Renaud Lambiotte, and Edward T Bullmore. Modular and hierarchically modular organization of brain networks. *Frontiers in neuroscience*, 4:200, 2010.
- [78] Sophie Achard and Ed Bullmore. Efficiency and cost of economical brain functional networks. *PLoS computational biology*, 3(2):e17, 2007.
- [79] Ed Bullmore and Olaf Sporns. The economy of brain network organization. *Nature Reviews Neuroscience*, 13(5):336, 2012.
- [80] Yong Liu, Meng Liang, Yuan Zhou, Yong He, Yihui Hao, Ming Song, Chunshui Yu, Haihong Liu, Zhening Liu, and Tianzi Jiang. Disrupted small-world networks in schizophrenia. *Brain*, 131(4):945–961, 2008.
- [81] Mikail Rubinov et al. Schizophrenia and abnormal brain network hubs. *Dialogues in clinical neuroscience*, 15(3):339, 2013.
- [82] Yong He, Zhang Chen, and Alan Evans. Structural insights into aberrant topological patterns of large-scale cortical networks in alzheimer’s disease. *Journal of Neuroscience*, 28(18):4756–4766, 2008.

- [83] Randy L Buckner, Jorge Sepulcre, Tanveer Talukdar, Fenna M Krienen, Hesheng Liu, Trey Hedden, Jessica R Andrews-Hanna, Reisa A Sperling, and Keith A Johnson. Cortical hubs revealed by intrinsic functional connectivity: mapping, assessment of stability, and relation to alzheimer's disease. *Journal of neuroscience*, 29(6):1860–1873, 2009.
- [84] Zhengjia Dai, Chaogan Yan, Kuncheng Li, Zhiqun Wang, Jinhui Wang, Miao Cao, Qixiang Lin, Ni Shu, Mingrui Xia, Yanchao Bi, et al. Identifying and mapping connectivity patterns of brain network hubs in alzheimer's disease. *Cerebral cortex*, 25(10):3723–3742, 2014.
- [85] Sheryl R Haut, Jana Veliškova, and Solomon L Moshé. Susceptibility of immature and adult brains to seizure effects. *The Lancet Neurology*, 3(10):608–617, 2004.
- [86] Leonardo Bonilha, Travis Nesland, Gabriel U Martz, Jane E Joseph, Maria V Spampinato, Jonathan C Edwards, and Ali Tabesh. Medial temporal lobe epilepsy is associated with neuronal fibre loss and paradoxical increase in structural connectivity of limbic structures. *J Neurol Neurosurg Psychiatry*, 83(9):903–909, 2012.
- [87] Mark P Richardson. Large scale brain models of epilepsy: dynamics meets connectomics. *J Neurol Neurosurg Psychiatry*, 83(12):1238–1248, 2012.
- [88] Peter Neal Taylor, Marcus Kaiser, and Justin Dauwels. Structural connectivity based whole brain modelling in epilepsy. *Journal of neuroscience methods*, 236:51–57, 2014.
- [89] John S Duncan, Josemir W Sander, Sanjay M Sisodiya, and Matthew C Walker. Adult epilepsy. *The Lancet*, 367(9516):1087–1100, 2006.
- [90] Susan Spencer and Linda Huh. Outcomes of epilepsy surgery in adults and children. *The Lancet Neurology*, 7(6):525–537, 2008.
- [91] Nishant Sinha, Justin Dauwels, Marcus Kaiser, Sydney S Cash, M Brandon Westover, Yujiang Wang, and Peter N Taylor. Predicting neurosurgical outcomes in

- focal epilepsy patients using computational modelling. *Brain*, 140(2):319–332, 2016.
- [92] Mark A Kramer, Uri T Eden, Eric D Kolaczyk, Rodrigo Zepeda, Emad N Eskandar, and Sydney S Cash. Coalescence and fragmentation of cortical networks during focal seizures. *Journal of Neuroscience*, 30(30):10076–10085, 2010.
- [93] Aaron F Alexander-Bloch, Danielle S Bassett, and David A Ross. Missed connections: A network approach to understanding psychiatric illness. *Biological Psychiatry*, 84(2):e9–e11, 2018.
- [94] Joon-Young Moon, Junhyeok Kim, Tae-Wook Ko, Minkyung Kim, Yasser Iturria-Medina, Jee-Hyun Choi, Joseph Lee, George A Mashour, and UnCheol Lee. Structure shapes dynamics and directionality in diverse brain networks: mathematical principles and empirical confirmation in three species. *Scientific reports*, 7:46606, 2017.
- [95] Cornelis J Stam and Elisabeth CW van Straaten. Go with the flow: use of a directed phase lag index (dpli) to characterize patterns of phase relations in a large-scale model of brain dynamics. *Neuroimage*, 62(3):1415–1428, 2012.
- [96] Joon-Young Moon, UnCheol Lee, Stefanie Blain-Moraes, and George A Mashour. General relationship of global topology, local dynamics, and directionality in large-scale brain networks. *PLoS computational biology*, 11(4):e1004225, 2015.
- [97] Alard Roebroeck, Elia Formisano, and Rainer Goebel. Mapping directed influence over the brain using granger causality and fmri. *Neuroimage*, 25(1):230–242, 2005.
- [98] André M Bastos and Jan-Mathijs Schoffelen. A tutorial review of functional connectivity analysis methods and their interpretational pitfalls. *Frontiers in systems neuroscience*, 9:175, 2016.
- [99] Jonathan J Crofts, Michael Forrester, and Reuben D O’Dea. Structure-function clustering in multiplex brain networks. *EPL (Europhysics Letters)*, 116(1):18003, 2016.

- [100] Javier M Buldú and Mason A Porter. Frequency-based brain networks: From a multiplex framework to a full multilayer description. *Network Neuroscience*, 2(4):418–441, 2018.
- [101] Ernesto Estrada. *The structure of complex networks: theory and applications*. Oxford University Press, 2012.
- [102] Mark Newman. *Networks*. Oxford university press, 2018.
- [103] Giorgio Fagiolo. Clustering in complex directed networks. *Physical Review E*, 76(2):026107, 2007.
- [104] Leo Spizzirri. Justification and application of eigenvector centrality. *Algebra in Geography: Eigenvectors of Network*, 2011.
- [105] Cristopher Moore and Mark EJ Newman. Epidemics and percolation in small-world networks. *Physical Review E*, 61(5):5678, 2000.
- [106] Mark EJ Newman, DJ Walls, Mark Newman, Albert-László Barabási, and Duncan J Watts. Scaling and percolation in the small-world network model. In *The Structure and Dynamics of Networks*, pages 310–320. Princeton University Press, 2011.
- [107] Béla Bollobás and Bollobás Béla. *Random graphs*. Number 73 in Cambridge studies in advanced mathematics. Cambridge university press, 2001.
- [108] Keiichi Onoda and Shuhei Yamaguchi. Small-worldness and modularity of the resting-state functional brain network decrease with aging. *Neuroscience letters*, 556:104–108, 2013.
- [109] Qihai Yue, Randi C Martin, Simon Fischer-Baum, Aurora I Ramos-Nuñez, Fengdan Ye, and Michael W Deem. Brain modularity mediates the relation between task complexity and performance. *Journal of cognitive neuroscience*, 29(9):1532–1546, 2017.
- [110] Santo Fortunato. Community detection in graphs. *Physics reports*, 486(3-5):75–174, 2010.

- [111] Olaf Sporns and Richard F Betzel. Modular brain networks. *Annual review of psychology*, 67:613–640, 2016.
- [112] MEJ Newman. Spectral community detection in sparse networks. *arXiv preprint arXiv:1308.6494*, 2013.
- [113] Mathieu Golos, Viktor Jirsa, and Emmanuel Daucé. Multistability in large scale models of brain activity. *PLoS computational biology*, 11(12):e1004644, 2015.
- [114] John J Hopfield. Neurons with graded response have collective computational properties like those of two-state neurons. *Proceedings of the national academy of sciences*, 81(10):3088–3092, 1984.
- [115] Peter J Menck, Jobst Heitzig, Norbert Marwan, and Jürgen Kurths. How basin stability complements the linear-stability paradigm. *Nature physics*, 9(2):89, 2013.
- [116] John J Hopfield. Neural networks and physical systems with emergent collective computational abilities. *Proceedings of the national academy of sciences*, 79(8):2554–2558, 1982.
- [117] Klaas Enno Stephan. The history of cocomac. *Neuroimage*, 80:46–52, 2013.
- [118] JW Scannell, GAPC Burns, CC Hilgetag, MA O’Neil, and Malcolm P Young. The connectional organization of the cortico-thalamic system of the cat. *Cerebral Cortex*, 9(3):277–299, 1999.
- [119] Richard Michael Durbin. Studies on the development and organisation of the nervous system of caenorhabditis elegans, 1987.
- [120] John G White, Eileen Southgate, J Nichol Thomson, and Sydney Brenner. The structure of the nervous system of the nematode caenorhabditis elegans. *Philos Trans R Soc Lond B Biol Sci*, 314(1165):1–340, 1986.
- [121] Yoonsuck Choe, BH McCormick, and W Koh. Network connectivity analysis on the temporally augmented c. elegans web: A pilot study. In *Soc Neurosci Abstr*, volume 30, 2004.

- [122] Marcus Kaiser and Claus C Hilgetag. Nonoptimal component placement, but short processing paths, due to long-distance projections in neural systems. *PLoS computational biology*, 2(7):e95, 2006.
- [123] Daniel J Felleman and David C Van Essen. Distributed hierarchical processing in the primate cerebral cortex. In *Cereb cortex*. Citeseer, 1991.
- [124] Edward H Yeterian and Deepak N Pandya. Corticothalamic connections of the posterior parietal cortex in the rhesus monkey. *Journal of Comparative Neurology*, 237(3):408–426, 1985.
- [125] ST Carmichael and JL Price. Architectonic subdivision of the orbital and medial prefrontal cortex in the macaque monkey. *Journal of Comparative Neurology*, 346(3):366–402, 1994.
- [126] James W Lewis and David C Van Essen. Mapping of architectonic subdivisions in the macaque monkey, with emphasis on parieto-occipital cortex. *Journal of Comparative Neurology*, 428(1):79–111, 2000.
- [127] F Reinoso-Suarez. Connectional patterns in parietotemporooccipital association cortex of the feline cerebral cortex. *Cortical integration. IBRO*, 11:255–278, 1984.
- [128] Jack W Scannell, Colin Blakemore, and Malcolm P Young. Analysis of connectivity in the cat cerebral cortex. *Journal of Neuroscience*, 15(2):1463–1483, 1995.
- [129] Lucianoda F Costa, Marcus Kaiser, and Claus C Hilgetag. Predicting the connectivity of primate cortical networks from topological and spatial node properties. *BMC systems biology*, 1(1):16, 2007.
- [130] Alice Roksztin, Zita Márkus, Gábor Braunitzer, Antal Berényi, György Benedek, and Attila Nagy. Visual pathways serving motion detection in the mammalian brain. *Sensors*, 10(4):3218–3242, 2010.
- [131] Bram A Siebert, Cameron L Hall, James P Gleeson, and Malbor Asllani. The role of modularity in self-organisation dynamics in biological networks. *arXiv preprint arXiv:2003.12311*, 2020.

- [132] Malbor Asllani, Joseph D Challenger, Francesco Saverio Pavone, Leonardo Sacconi, and Duccio Fanelli. The theory of pattern formation on directed networks. *Nature communications*, 5(1):1–9, 2014.
- [133] Gustavo Deco, Mario Senden, and Viktor Jirsa. How anatomy shapes dynamics: a semi-analytical study of the brain at rest by a simple spin model. *Frontiers in computational neuroscience*, 6:68, 2012.
- [134] Jessica S Damoiseaux, SARB Rombouts, Frederik Barkhof, Philip Scheltens, Cornelis J Stam, Stephen M Smith, and Christian F Beckmann. Consistent resting-state networks across healthy subjects. *Proceedings of the national academy of sciences*, 103(37):13848–13853, 2006.
- [135] Luca Cocchi, Leonardo L Gollo, Andrew Zalesky, and Michael Breakspear. Criticality in the brain: A synthesis of neurobiology, models and cognition. *Progress in neurobiology*, 158:132–152, 2017.
- [136] Ed Bullmore and Olaf Sporns. Complex brain networks: graph theoretical analysis of structural and functional systems. *Nature reviews neuroscience*, 10(3):186–198, 2009.
- [137] CJ Stam, ECW Van Straaten, E Van Dellen, P Tewarie, G Gong, A Hillebrand, J Meier, and P Van Mieghem. The relation between structural and functional connectivity patterns in complex brain networks. *International Journal of Psychophysiology*, 103:149–160, 2016.
- [138] Farzad V Farahani, Waldemar Karwowski, and Nichole R Lighthall. Application of graph theory for identifying connectivity patterns in human brain networks: a systematic review. *frontiers in Neuroscience*, 13:585, 2019.
- [139] Yoshiki Kuramoto. International symposium on mathematical problems in theoretical physics. *Lecture notes in Physics*, 30:420, 1975.
- [140] Juan A Acebrón, Luis L Bonilla, Conrad J Pérez Vicente, Félix Ritort, and Renato Spigler. The kuramoto model: A simple paradigm for synchronization phenomena. *Reviews of modern physics*, 77(1):137, 2005.

- [141] Carlo R Laing. Phase oscillator network models of brain dynamics. *Computational models of brain and behavior*, 505:517, 2017.
- [142] Arkady Pikovsky, Michael Rosenblum, Jürgen Kurths, and A Synchronization. A universal concept in nonlinear sciences. *Self*, 2:3, 2001.
- [143] Alex Arenas, Albert Díaz-Guilera, Jürgen Kurths, Yamir Moreno, and Changsong Zhou. Synchronization in complex networks. *Physics reports*, 469(3):93–153, 2008.
- [144] Arthur T Winfree. Biological rhythms and the behavior of populations of coupled oscillators. *Journal of theoretical biology*, 16(1):15–42, 1967.
- [145] Francisco A Rodrigues, Thomas K DM Peron, Peng Ji, and Jürgen Kurths. The kuramoto model in complex networks. *Physics Reports*, 610:1–98, 2016.
- [146] Fatihcan M Atay and Axel Hutt. Stability and bifurcations in neural fields with finite propagation speed and general connectivity. *SIAM Journal on Applied Mathematics*, 65(2):644–666, 2004.
- [147] Hae-Jeong Park, Karl J Friston, Chongwon Pae, Bumhee Park, and Adeel Razi. Dynamic effective connectivity in resting state fmri. *NeuroImage*, 180:594–608, 2018.
- [148] E Kevin Kelloway. Structural equation modelling in perspective. *Journal of Organizational Behavior*, 16(3):215–224, 1995.
- [149] Karl J Friston, Lee Harrison, and Will Penny. Dynamic causal modelling. *Neuroimage*, 19(4):1273–1302, 2003.
- [150] Junhyeok Kim, Joon-Young Moon, Uncheol Lee, George A Mashour, Seunghwan Kim, and Tae-Wook Ko. Phase lead/lag due to degree inhomogeneity in complex oscillator network with application to brain networks. *BMC Neuroscience*, 16(1):1–2, 2015.
- [151] Cornelis J Stam, Guido Nolte, and Andreas Daffertshofer. Phase lag index: assessment of functional connectivity from multi channel eeg and meg with diminished bias from common sources. *Human brain mapping*, 28(11):1178–1193, 2007.

- [152] Russell Merris. Laplacian matrices of graphs: a survey. *Linear algebra and its applications*, 197:143–176, 1994.
- [153] Carsten Grabow, Stefan Grosskinsky, and Marc Timme. Speed of complex network synchronization. *The European Physical Journal B*, 84(4):613–626, 2011.
- [154] Patrick N McGraw and Michael Menzinger. Laplacian spectra as a diagnostic tool for network structure and dynamics. *Physical Review E*, 77(3):031102, 2008.
- [155] Takashi Nishikawa and Adilson E Motter. Network synchronization landscape reveals compensatory structures, quantization, and the positive effect of negative interactions. *Proceedings of the National Academy of Sciences*, 107(23):10342–10347, 2010.
- [156] Aref Pariz, Ingo Fischer, Alireza Valizadeh, and Claudio Mirasso. Transmission delays and frequency detuning can regulate information flow between brain regions. *PLoS computational biology*, 17(4):e1008129, 2021.
- [157] Spase Petkoski, J Matias Palva, and Viktor K Jirsa. Phase-lags in large scale brain synchronization: Methodological considerations and in-silico analysis. *PLoS computational biology*, 14(7):e1006160, 2018.
- [158] Leonardo L Gollo and Michael Breakspear. The frustrated brain: from dynamics on motifs to communities and networks. *Philosophical Transactions of the Royal Society B: Biological Sciences*, 369(1653):20130532, 2014.
- [159] Frank C Hoppensteadt and Eugene M Izhikevich. *Weakly connected neural networks*, volume 126. Springer Science & Business Media, 2012.
- [160] Francisco Varela, Jean-Philippe Lachaux, Eugenio Rodriguez, and Jacques Martinerie. The brainweb: phase synchronization and large-scale integration. *Nature reviews neuroscience*, 2(4):229–239, 2001.
- [161] Jonathan J Crofts, Michael Forrester, Steve Coombes, and Reuben D O’Dea. Structure-function clustering in weighted brain networks. Submitted to *New Journal of Physics* (2021).

- [162] Peter J Mucha. Community structure in time-dependent, multiscale, and multiplex networks (vol 328, pg 876, 2010). *Science*, 329(5989):277–277, 2010.
- [163] Peter Grindrod, Mark C Parsons, Desmond J Higham, and Ernesto Estrada. Communicability across evolving networks. *Physical Review E*, 83(4):046120, 2011.
- [164] Alexander V Mantzaris, Danielle S Bassett, Nicholas F Wymbs, Ernesto Estrada, Mason A Porter, Peter J Mucha, Scott T Grafton, and Desmond J Higham. Dynamic network centrality summarizes learning in the human brain. *Journal of Complex Networks*, 1(1):83–92, 2013.
- [165] Enrique CA Hansen, Demian Battaglia, Andreas Spiegler, Gustavo Deco, and Viktor K Jirsa. Functional connectivity dynamics: modeling the switching behavior of the resting state. *Neuroimage*, 105:525–535, 2015.
- [166] Victoria L Morgan, Bassel Abou-Khalil, and Baxter P Rogers. Evolution of functional connectivity of brain networks and their dynamic interaction in temporal lobe epilepsy. *Brain connectivity*, 5(1):35–44, 2015.
- [167] Hong Zhu, Juan Huang, Lifu Deng, Naying He, Lin Cheng, Pin Shu, Fuhua Yan, Shanbao Tong, Junfeng Sun, and Huawei Ling. Abnormal dynamic functional connectivity associated with subcortical networks in parkinson’s disease: a temporal variability perspective. *Frontiers in neuroscience*, 13:80, 2019.
- [168] Delphine Puttaert, Nicolas Coquelet, Vincent Wens, Philippe Peigneux, Patrick Fery, Antonin Rovai, Nicola Trotta, N Sadeghi, Tim Coolen, J-C Bier, et al. Alterations in resting-state network dynamics along the alzheimer’s disease continuum. *Scientific reports*, 10(1):1–13, 2020.
- [169] Mathieu Bastian, Sebastien Heymann, and Mathieu Jacomy. Gephi: an open source software for exploring and manipulating networks. In *Proceedings of the International AAAI Conference on Web and Social Media*, volume 3, 2009.
- [170] Georgios A Pavlopoulos, David Paez-Espino, Nikos C Kyrpidis, and Ioannis Iliopoulos. Empirical comparison of visualization tools for larger-scale network analysis. *Advances in bioinformatics*, 2017, 2017.

- [171] Leonard Kaufman and Peter J Rousseeuw. *Finding groups in data: an introduction to cluster analysis*, volume 344. John Wiley & Sons, 2009.
- [172] James Michael Whitacre. Biological robustness: paradigms, mechanisms, and systems principles. *Frontiers in genetics*, 3:67, 2012.